

Hybrid discrete (H_N^T) approximations to the equation of radiative transfer

by

Minwoo Shin

A dissertation submitted to the graduate faculty
in partial fulfillment of the requirements for the degree of
DOCTOR OF PHILOSOPHY

Major: Applied Mathematics

Program of Study Committee:
James Rossmanith, Major Professor
Hailiang Liu
Rodney Fox
Jue Yan
Paul Sacks

The student author, whose presentation of the scholarship herein was approved by the program of study committee, is solely responsible for the content of this dissertation. The Graduate College will ensure this dissertation is globally accessible and will not permit alterations after a degree is conferred.

Iowa State University

Ames, Iowa

2019

Copyright © Minwoo Shin, 2019. All rights reserved.

DEDICATION

I would like to dedicate this thesis to my parents Hyun-Seok Shin and Young-Ae Lee, to my wife Jihye, and to my son Ian. Without their support I would not have been able to complete this work.

TABLE OF CONTENTS

LIST OF TABLES	vi
LIST OF FIGURES	viii
ACKNOWLEDGEMENTS	xii
ABSTRACT	xii
CHAPTER 1. INTRODUCTION	1
1.1 The Radiative Transfer Equation	1
1.2 Numerical Methods	2
1.3 Scope of This Work	3
CHAPTER 2. CLASSICAL APPROXIMATIONS OF RADIATIVE TRANSFER: SPHERICAL HARMONICS AND DISCRETE ORDINATES	5
2.1 Spherical Harmonics	5
2.1.1 Properties of spherical harmonics	7
2.1.2 A trick in spherical harmonics approximation	7
2.1.3 Streaming term	8
2.1.4 P_N equations	8
2.1.5 Number of unknowns	9
2.1.6 Reduced number of unknowns	9
2.1.7 Reduced moment equations	10
2.2 Discrete Ordinates	12

CHAPTER 3. LINEAR HYPERBOLIC SYSTEMS	14
3.1 1D Linear Hyperbolic Systems	14
3.1.1 The Riemann problem for a linear system	15
3.1.2 The classical upwind method	15
3.2 2D Hyperbolic Linear Systems	16
CHAPTER 4. THE DISCONTINUOUS GALERKIN METHODS	17
4.1 A Brief History	17
4.2 Discontinuous Galerkin Methods	17
4.2.1 Hyperbolic conservation law in 1D	18
4.2.2 Hyperbolic conservation law in 2D	21
4.2.3 Quadrature rules	24
4.2.4 Numerical flux	25
4.3 Time integration	27
4.3.1 Explicit Runge-Kutta methods	27
4.3.2 Strong-stability preserving integrators	29
4.3.3 Diagonally implicit Runge-Kutta methods	30
CHAPTER 5. THE H_N^T APPROXIMATION TO THE LINEAR KINETIC EQUATION	33
5.1 Introduction	33
5.2 The Hybrid Discrete (H_N^T) Approximation: One-Dimension	34
5.2.1 Derivation	34
5.2.2 Discontinuous Galerkin (DG) Method	37
5.2.3 SSP-RK	38
5.2.4 Positivity-preserving limiters	39

5.3	Two-Dimensional Piecewise- P_N equations	40
5.3.1	Version I: Fragments	40
5.3.2	Version II: Strips	43
5.4	Hybrid Discrete (H_N^T) Approximations: Multi-Dimension	46
CHAPTER 6. NUMERICAL RESULTS		54
6.1	Numerical Results in 1D	54
6.2	Numerical Results in 2D	58
6.2.1	The line-source problem	58
6.2.2	The lattice problem	60
6.3	Numerical Results in 2D with Octantal-Spherical-Triangular Mesh	75
CHAPTER 7. H_N^T APPROXIMATION WITH RICHARDSON EXTRAPOLATION		80
7.1	Derivation	80
7.2	Numerical Results	81
CHAPTER 8. COLLIDED-UNCOLLIDED H_N^T APPROXIMATIONS		85
CHAPTER 9. BLENDED P_N AND H_N^T SCHEMES		90
9.1	Derivation	90
9.2	Numerical Results	95
CHAPTER 10. CONCLUSION AND FUTURE WORK		96
BIBLIOGRAPHY		97

LIST OF TABLES

Table 5.1 Algorithm for low-storage strong stability-preserving Runge-Kutta (ten-stage fourth-order).	39
Table 6.1 Parameters for the 2D line-source problem.	58
Table 6.2 Convergence rate of spherical error for H_1^T . We fix the order of polynomial basis function ($N = 0$) for each spherical triangle and increase the number of spherical triangles T	59
Table 6.3 Convergence rate of spherical error for H_2^T . We fix the order of polynomial basis function ($N = 1$) for each spherical triangle and increase the number of spherical triangles T	61
Table 6.4 Convergence rate of spherical error for H_3^T . We fix the order of polynomial basis function ($N = 2$) for each spherical triangle and increase the number of spherical triangles T	64
Table 6.5 Convergence rate of spherical error for H_4^T . We fix the order of polynomial basis function ($N = 3$) for each spherical triangle and increase the number of spherical triangles T	64
Table 6.6 Convergence rate of spherical error for H_N^{20} . Here we fix the number of spherical triangles ($T = 20$) and increase the order of polynomial basis function for each triangle from 0 to 10.	67
Table 6.7 Convergence rate of spherical error for H_N^{80} . We fix the number of spherical triangles ($T = 80$) and increase the order of polynomial basis function for each triangle from 0 to 10.	70

Table 6.8 Convergence rate of spherical error for H_N^{320} . We fix the number of spherical triangles ($T = 320$) and increase the order of polynomial basis function for each triangle from 0 to 5. Due to the limit of memory, it is impossible to test higher order in our computational environment.	70
Table 6.9 Parameters for the lattice problem.	70
Table 7.1 Error of H_1^T with Richardson extrapolation. With the Richardson extrapolation, we cannot obtain any improvement of the original error with the spherical triangular mesh. This might due to the refinement process of our spherical triangular mesh generation. Even though the number of spherical triangles become four times at the next step, the size of each triangle is not exactly one half of previous triangle. . . .	82
Table 7.2 Error of H_2^T with Richardson extrapolation. With the Richardson extrapolation, we cannot obtain any improvement of the original error with the spherical triangular mesh. This might due to the refinement process of our spherical triangular mesh generation. Even though the number of spherical triangles become four times at the next step, the size of each triangle is not exactly one half of previous triangle. . . .	83

LIST OF FIGURES

Figure 2.1 Spherical Coordinate.	6
Figure 5.1 The polar angle θ and azimuthal angle ϕ	41
Figure 5.2 Triangular meshes for the Hybrid Discrete Method.	52
Figure 5.3 Octantal triangular meshes for the Hybrid Discrete Method.	53
Figure 6.1 P_N solutions in 1D. Here each P_N solutions are compared to the exact P_N solutions. This is the numerical accuracy test for our numerical schemes.	55
Figure 6.2 The convergence rate of P_N solutions in 1D. Each of P_N solutions show the correct order by our SSP-RK4-DG scheme: 1st, 2nd, 3rd and 4th order, respectively. This shows that our numerical scheme has correct order of accuracy.	56
Figure 6.3 The density obtained from P_N and H_N^T solutions in 1D. Red plots represent the P_N solutions, while black plots represent the H_N^T solutions. The H_N^T solution converges to the exact solution as T increases.	57
Figure 6.4 The density obtained from H_N^T solutions in 1D. Red plots represent the H_N^T solutions with negative particle concentration near $z = -1$ and $z = 1$, while black plots do not show negativity due to the positivity-preserving limiters.	57
Figure 6.5 P_N solutions with low N in 2D.	58
Figure 6.6 P_N solutions with low N in 2D.	59
Figure 6.7 P_N solutions with high N in 2D.	60

Figure 6.8 P_N solutions with high N in 2D.	61
Figure 6.9 H_N^T for the line source problem in 2D.	62
Figure 6.10 H_N^T for the line source problem in 2D.	63
Figure 6.11 H_N^T for the line source problem in 2D.	64
Figure 6.12 H_N^T for the line source problem in 2D (cross section along x-axis).	65
Figure 6.13 H_N^T for the line source problem in 2D (cross section along x-axis).	66
Figure 6.14 H_N^T for the line source problem in 2D (cross section along x-axis).	67
Figure 6.15 P_N vs H_N^T with similar number of equations.	68
Figure 6.16 P_N vs H_N^T with similar number of equations (cross-section along x-axis). Red plots are the exact solutions for the line source problem with the initial condition (6.2). Black plots are P_N solutions and blue plots are H_N^T solutions. Each plot has the similar number of equations for efficiency comparison. H_N^T approximations tend to have better accuracy than P_N approximations for relatively small number of equations.	69
Figure 6.17 The lattice system: Red and yellow regions are highly absorbing while blue regions are highly scattering. The source of strength one is located in the center (yellow) region.	71
Figure 6.18 Lattice solution with P_N vs H_N^T	72
Figure 6.19 Lattice P_N solutions in 2D.	73
Figure 6.20 Lattice H_N^T solutions in 2D.	73
Figure 6.21 Lattice H_N^T solutions in 2D (cross-section along x-axis from center).	74
Figure 6.22 Lattice H_N^T solutions in 2D (cross-section along y-axis from center).	74
Figure 6.23 H_N^T for the line source problem in 2D.	76
Figure 6.24 H_N^T for the line source problem in 2D (cross section along x-axis).	77
Figure 6.25 P_N vs H_N^T with similar number of equations.	78
Figure 6.26 P_N vs H_N^T with similar number of equations.	79

Figure 7.1 H_1^T solutions with Richardson extrapolation with the original spherical triangular mesh.	81
Figure 7.2 H_1^T solutions with Richardson extrapolation (cross-section along x-axis from center) with the original spherical triangular mesh.	82
Figure 7.3 H_2^T solutions with Richardson extrapolation with the original spherical triangular mesh.	83
Figure 7.4 H_2^T solutions with Richardson extrapolation (cross-section along x-axis from center) with the original spherical triangular mesh.	84

ACKNOWLEDGEMENTS

I would like to thank everyone those who helped me with various aspects of my life at Iowa State University (ISU).

First and foremost, I would like to thank Dr. James Rossmanith for his guidance, patience, and support throughout my study and research. His keen insights and kind words of encouragement have always helped my PhD life. Whenever my research hit a dead-end, he always gave advice to overcome my difficulties. Without his guidance, I would never would have been able to start or finish my research and this thesis.

I would like to thank Dr. Sung-Yell Song who has given me invaluable advice and encouragement to finish my study during my entire graduate career. He has been a great teacher and has guided me to a better trajectory of in life.

I would also like to thank Ms. Melanie Erickson. She has been very important in helping me with many aspects of graduate life and work.

I would also like to thank my committee members for their efforts and contributions to my graduation: Drs. Hailiang Liu, Jue Yan, Paul Sacks, and Rodney Fox.

ABSTRACT

In computational physics, especially in the disciplines of radiative heat transfer, astrophysics, and nuclear engineering, we can easily find mathematical models in the form of linear transport equations. Linear transport equations are not easy to solve numerically, since they are integro-differential equations defined in a high-dimensional phase space, (e.g., seven variables for three dimensional problems). There are several methods used in radiative transfer, including the implicit Monte Carlo, discrete ordinate (S_N), and spherical harmonics (P_N) methods. The implicit Monte Carlo is a direct numerical simulation approach that keeps track of many particles, and for that reason is both accurate and computational expensive. The discrete ordinate method discretizes velocity space into rays along various propagation directions; the difficulty with this approach is that the solutions tend to show ray effects in cases where there should be isotropy. The spherical harmonics approximation use moment equations constructed from the spherical harmonics basis functions to discretize the transport equations in angular variables; the difficulty here is that a truncated spherical harmonic expansion does not guarantee a positive solution.

In this work, we introduce an alternative formulation of the P_N approximation that hybridizes aspects of both P_N and S_N . We are calling this method the H_N^T approach, where the H stands for “hybrid”, the superscript is the number of angular elements, and the subscript is the polynomial order used on each angular element. Although our basic scheme does not guarantee positivity of the solution, the new formulation allows for the introduction of local limiters that can be used to enforce positivity. We first develop our scheme and limiting strategy on the one-dimensional linear transport equations. We then show how to extend this idea to the multidimensional case using unstructured grids in phase space. The resulting scheme is validated on several standard test cases. We also explore

several generalizations of this idea that could be used to improve the simulation accuracy, including Richardson extrapolation, collided-uncollided decompositions, and blended P_N - H_N^T schemes.

The computational results are obtained using the software package DoGPack, which is a package written in C++ and Python for solving hyperbolic partial differential equations via the discontinuous Galerkin method. For more details, see <http://www.dogpack-code.org>. For the mesh generation, we used MeshGenC++ (An Unstructured Grid Generator). For more details, see <http://www.dogpack-code.org/MeshGenC++>. The computations are performed on an Intel CoreTM i7-7700K CPU @ 4.20GHz×8 processor, running Ubuntu Linux 16.04 LTS, and the code is compiled with the GCC 5.4.0 compiler.

CHAPTER 1. INTRODUCTION

1.1 The Radiative Transfer Equation

A standard form of the Boltzmann transport equation is

$$\frac{1}{v} \frac{\partial f}{\partial t} + \underline{\Omega} \cdot \nabla f = C(f), \quad (1.1)$$

where $f(\underline{x}, \underline{\Omega}, \epsilon, t)$ is a density, ϵ is the energy of the particles, $\underline{\Omega}$ is the particle travel direction, t is time, and C is a collision operator. The equation models the particle movement through a medium. The function f is a kinetic distribution function in seven dimensions, i.e., $\underline{x} = (x, y, z)$, $\underline{\Omega} = (\theta, \phi)$, ϵ , and time t , where θ and ϕ are polar and azimuthal angles, respectively. Because of the high dimensionality of this equation, solving the radiative transfer equation is computationally expensive. Since directly solving an equation (1.1) difficult, some approximation is required in order to reduce the computational cost.

Equation (1.1) is often written in terms of the radiation intensity $I(r, \underline{\Omega}, \epsilon, t) = \hbar\nu f$, where \hbar is Planck's constant, and ν is the photon frequency with $\epsilon = \hbar\nu$. The intensity is an efficient way to measure the radiation since it is independent of the range at which it is measured. Intensity is a flux through a surface in one direction. After doing some algebraic treatment to (1.1), we get a new equation:

$$\frac{1}{c} \frac{\partial I}{\partial t} + \underline{\Omega} \cdot \nabla I = -\sigma_t I + \frac{\sigma_s}{4\pi} \int_{4\pi} I d\underline{\Omega}' + \sigma_a B(T_m, \epsilon) + S, \quad (1.2)$$

where c is the speed of light, T_m is the temperature of a material depending on the material energy, σ_s , σ_a , and $\sigma_t = \sigma_s + \sigma_a$ are scattering, absorption and total cross sections, respectively, and $B(T_m, \epsilon)$ is a black body source term.

1.2 Numerical Methods

There are two main classes of methods for solving the radiative transfer equation. One approach is stochastic in nature, the other is deterministic. The stochastic approach known as the Monte Carlo (MC) method is known as the most reliable and accurate method for solving the complicated radiative transfer equations. However, since the MC method simulates the movement of each particle and calculates average trajectories of simulated particles, the MC method has significantly more expensive computational cost, although the accuracy improvement can be made by simply increasing the number of photons traced. Due to the high computational cost and statistical noise problems, there have been many approaches to improve or eliminate the disadvantages of MC method [47, 31].

Implicit Monte Carlo (IMC) methods are stochastic methods that solve RTE with implicit time stepping. These methods simulate the trajectory of photons and use the linearized equation to model the evolution of the radiation. Like all other stochastic methods, IMC solution also has stochastic noise. The computational cost of IMC methods is expensive, although it generally provides the most reliable solution of all existing methods.

Deterministic methods have relatively low computational cost. However, deterministic methods could lead to numerical instabilities due to CFL restriction violations or other numerical errors that produce non-physical solutions, e.g., negative density, ray-effect, or oscillation, etc.... Specific types of equations require optimized numerical methods, and most of the numerical methods have their own strengths and weaknesses. For these reasons, a significant amount of effort is required to improve the shortcomings of numerical methods. The most popular and reliable deterministic methods for thermal radiation transport is the diffusion method, the spherical harmonics (P_N) method, and the discrete ordinates (S_N) method [7].

The S_N method solves the radiation transport equation (RTE) using quadrature rule along particularly chosen angular directions. The S_N method is easy to solve and well-studied. This method has adopted new techniques for a long time, e.g., fast iterative solver

[2], parallelization [36, 23], rotational S_N [9], and new quadrature rules [20, 5], etc.... However, these methods still suffer from the so called the “ray effect” because of the lack of communication between adjacent angular directions. These rays are almost impossible to be totally eliminated with the limited number of discrete ordinates.

The flux-limited diffusion method is another deterministic method. This method is easy to solve and the computational cost is also low; however, it is inaccurate in the optically thin limit or when the gradient is large. This method also makes the diffusion equation nonlinear and makes the hyperbolic transport equation into the parabolic transport equation. As a result, this means radiation can propagate beyond the speed of light. In order to fix this phenomena, a flux limiter has to be introduced. All in all, the flux-limited diffusion method has low order of accuracy, but it is very efficient in the optically thick media.

The P_N method is a deterministic methods based on a truncated expansion in terms of spherical harmonics. P_N equations are a spectral method using the spherical harmonics as basis functions, and as a result, wave effects are caused. The main drawback of P_N methods are that these methods can lead to negative particle concentration, which is physically incorrect, and it is very difficult to apply boundary condition [27]. However, these methods have desirable properties too, e.g., the solution is rotationally invariant, and convergent in the L^2 sense.

1.3 Scope of This Work

The main focus of this work is to develop a deterministic numerical method to solve the radiation transport equation (RTE) efficiently. The most popular deterministic methods such as spherical harmonics (P_N) approximation and discrete ordinates (S_N) have their own benefits and drawbacks. We try to combine desirable behaviors of both P_N and S_N methods to improve the defective aspects of those methods. In particular, we introduce an alternative formulation of the P_N approximation that hybridizes aspects of both P_N and S_N . We are calling this method the H_N^T approach, where the H stands for “hybrid”, the

superscript is the number of angular elements, and the subscript is the polynomial order used on each angular element. Although our basic scheme does not guarantee positivity of the solution, the new formulation allows for the introduction of local limiters that can be used to enforce positivity. We first develop our scheme and limiting strategy on the one-dimensional linear transport equations. We then show how to extend this idea to the multidimensional case using unstructured grids in phase space. The resulting scheme is validated on several standard test cases. We also explore several generalizations of this idea that could be used to improve the simulation accuracy, including Richardson extrapolation, collided-uncollided decompositions, and blended P_N - H_N^T schemes.

This work is organized as follows: in Chapter 2 we review in detail the P_N and S_N methods for the radiative transfer equations. No matter which approximation is used, the end result is a system linear hyperbolic partial differential equations; in Chapter 3 we review some mathematical concepts relevant in understanding the behavior of such equations. In Chapter 4 we detail the underlying numerical methods that will be used in the current work, namely the strong-stability-preserving Runge-Kutta discontinuous Galerkin (SSP-RK-DG) scheme. The primary part of this thesis begins in Chapter 5, in which we fully develop the H_N^T approach for radiative transfer in both the single and multidimensional settings. This method keeps the similar discrete ordinates from S_N methods, however, it can reduce the ray effect induced by the discrete angular directions by increasing the order of basis functions on each spherical triangle. Numerical results are provided in Chapter 6. In Chapters 7, 8, and 9 we explore several generalizations of the H_N^T idea that could be used to improve the simulation accuracy, including Richardson extrapolation (Chapter 7), collided-uncollided decompositions (Chapter 8), and blended P_N - H_N^T schemes (Chapter 9). Finally, we conclude in Chapter 10.

CHAPTER 2. CLASSICAL APPROXIMATIONS OF RADIATIVE TRANSFER: SPHERICAL HARMONICS AND DISCRETE ORDINATES

There are several approaches for solving the radiative transfer equations. The most well-studied deterministic methods include the spherical harmonics approximations and the discrete ordinate methods. Understanding both the spherical harmonics and the discrete ordinates method is useful in understanding the challenges in solving the radiative transfer equations numerically; and hence, in this chapter we review both methods [6, 44]. This will also lay the groundwork for the development of our newly proposed approach in subsequent chapters.

We consider here the one energy group Boltzmann transport equation [42]:

$$\frac{1}{v} F_{,t}(\underline{r}, \underline{\Omega}, t) + \underline{\Omega} \cdot \nabla_{\underline{r}} F(\underline{r}, \underline{\Omega}, t) + \sigma_t F(\underline{r}, \underline{\Omega}, t) = \int_{\mathbf{S}^2} \frac{\sigma_s}{4\pi} F(\underline{r}, \underline{\Omega}', t) d\underline{\Omega}' + S(\underline{r}, \underline{\Omega}, t), \quad (2.1)$$

where $F(\underline{r}, \underline{\Omega}, t)$ is the angular flux, \underline{r} is the position of the particle, $\underline{\Omega}$ is the particle movement direction, S is the external source, σ_t is the total cross section, σ_s is the isotropic scattering cross section, and v is the neutron speed.

2.1 Spherical Harmonics

The spherical harmonics (P_N) approximation of the radiative transfer equation (RTE) uses a truncated spherical harmonics expansion. It is known that the P_N solution converges in L_2 and it is rotationally invariant, i.e., symmetric in any direction. However, it suffers from having difficulties in imposing various boundary conditions, negative solutions, and oscillations [27]. There have been many attempts to overcome these drawbacks of P_N method. Hauck and McClarren [27] and others [22, 39, 41, 48] have developed various techniques to eliminate the negative particle concentration.

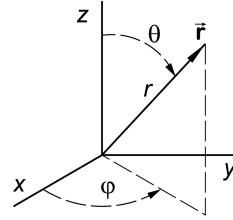


Figure 2.1: Spherical Coordinate.

The spherical harmonics basis function are used to represent functions on the surface of the unit sphere \mathbb{S}^2 as shown Figure 2.1. The basis functions have the following form:

$$Y_\ell^m(\mu, \varphi) = \sqrt{\frac{(2\ell+1)(\ell-m)!}{4\pi(\ell+m)!}} P_\ell^m(\mu) e^{im\varphi}, \quad (2.2)$$

where $\mu = \cos \theta$, $\theta \in [0, \pi]$, $\varphi \in [0, 2\pi]$, and $P_\ell^m(\mu)$ are the associated Legendre polynomials:

$$\begin{cases} P_\ell^m(\mu) = (-1)^m (1 - \mu^2)^{m/2} \frac{\partial^m P_\ell(\mu)}{\partial \mu^m} & \text{if } m \in [0, l], \\ P_\ell^m(\mu) = (-1)^m \frac{(l-|m|)!}{(l+|m|)!} P_\ell^{|m|}(\mu) & \text{if } m \in [-l, 0]. \end{cases}$$

The spherical harmonics are orthonormal on the surface of the unit sphere \mathbb{S}^2 :

$$\int_{\mathbb{S}^2} Y_\ell^m(\mu, \varphi) Y_{\ell'}^{m'}(\mu, \varphi) d\Omega = \delta_{ll'} \delta_{mm'}. \quad (2.3)$$

The angular flux F in (2.1) can be expressed using spherical harmonics :

$$F(\underline{r}, \underline{\Omega}, t) = \sum_{\ell=0}^{\infty} \sum_{m=-\ell}^{\ell} F_\ell^m(\underline{r}, t) Y_\ell^m(\mu, \varphi), \quad (2.4)$$

and we can approximate F by truncating spherical harmonics expansion:

$$F(\underline{r}, \underline{\Omega}, t) \approx \sum_{\ell=0}^N \sum_{m=-\ell}^{\ell} F_\ell^m(\underline{r}, t) Y_\ell^m(\mu, \varphi). \quad (2.5)$$

We consider equation (2.1) in absence of sources:

$$F_{,t} + \underline{\Omega} \cdot \nabla_{\underline{r}} F + \sigma_t F = \frac{\sigma_s}{4\pi} \int_{\mathbb{S}^2} F(\underline{r}, \underline{\Omega}, t) d\Omega. \quad (2.6)$$

In order to get the P_N equations, we use the ansatz (2.5), then multiply (2.6) by the conjugate of the spherical harmonics function \bar{Y}_ℓ^m , and integrate the equation over the unit

sphere \mathbb{S}^2 . By the fact that $Y_0^0 = \bar{Y}_0^0 = 1/\sqrt{4\pi}$, the scattering term becomes:

$$\begin{aligned}
& \frac{\sigma_s}{4\pi} \int_{\mathbb{S}^2} \bar{Y}_\ell^m(\underline{\Omega}) \int_{\mathbb{S}^2} F(x, z, \underline{\Omega}', t) d\underline{\Omega}' d\underline{\Omega} \\
&= \frac{\sigma_s}{\sqrt{4\pi}} \int_{\mathbb{S}^2} \bar{Y}_\ell^m(\underline{\Omega}) \int_{\mathbb{S}^2} \bar{Y}_0^0(\underline{\Omega}') F(x, z, \underline{\Omega}', t) d\underline{\Omega}' d\underline{\Omega} \\
&= \frac{\sigma_s}{\sqrt{4\pi}} \int_{\mathbb{S}^2} \bar{Y}_\ell^m(\underline{\Omega}) F_0^0(x, z, t) d\underline{\Omega} \\
&= \sigma_s F_0^0(x, z, t) \int_{\mathbb{S}^2} \bar{Y}_\ell^m(\underline{\Omega}) Y_0^0 d\underline{\Omega} \\
&= \sigma_s F_0^0(x, z, t) \delta_{\ell 0} \delta_{m0}.
\end{aligned} \tag{2.7}$$

2.1.1 Properties of spherical harmonics

The following properties can be found in [58] and will be used to simplify the P_N equations as in [6]:

$$\begin{aligned}
\cos \theta Y_\ell^m &= A_\ell^m Y_{\ell+1}^m + B_\ell^m Y_{\ell-1}^m, \\
\sin \theta e^{i\varphi} Y_\ell^m &= -C_\ell^m Y_{\ell+1}^{m+1} + D_\ell^m Y_{\ell-1}^{m+1}, \\
\sin \theta e^{-i\varphi} Y_\ell^m &= E_\ell^m Y_{\ell+1}^{m-1} - G_\ell^m Y_{\ell-1}^{m-1},
\end{aligned} \tag{2.8}$$

where

$$\begin{aligned}
A_\ell^m &= \sqrt{\frac{(\ell-m+1)(\ell+m+1)}{(2\ell+3)(2\ell+1)}}, & B_\ell^m &= \sqrt{\frac{(\ell-m)(\ell+m)}{(2\ell+1)(2\ell-1)}}, \\
C_\ell^m &= \sqrt{\frac{(\ell+m+1)(\ell+m+2)}{(2\ell+3)(2\ell+1)}}, & D_\ell^m &= \sqrt{\frac{(\ell-m)(\ell-m-1)}{(2\ell+1)(2\ell-1)}}, \\
E_\ell^m &= \sqrt{\frac{(\ell-m+1)(\ell-m+2)}{(2\ell+3)(2\ell+1)}}, & G_\ell^m &= \sqrt{\frac{(\ell+m)(\ell+m-1)}{(2\ell+1)(2\ell-1)}}.
\end{aligned} \tag{2.9}$$

It is easy to find that $A_{\ell-1}^m = B_\ell^m$, $C_\ell^m = F_{\ell+1}^{m+1}$, and $D_\ell^m = E_{\ell-1}^{m+1}$.

2.1.2 A trick in spherical harmonics approximation

Note that

$$\underline{\Omega} = \begin{bmatrix} \sin \theta \cos \varphi \\ \sin \theta \sin \varphi \\ \cos \theta \end{bmatrix}. \tag{2.10}$$

The following technique is used by Brunner [6]. Let

$$\underline{\Omega}' = \begin{bmatrix} \sin \theta (\cos \varphi + i \sin \varphi) \\ \sin \theta (\cos \varphi - i \sin \varphi) \\ \cos \theta \end{bmatrix} = \begin{bmatrix} \sin \theta e^{i\varphi} \\ \sin \theta e^{-i\varphi} \\ \cos \theta \end{bmatrix}, \quad (2.11)$$

and

$$\nabla' = \begin{bmatrix} \frac{1}{2} \left(\frac{\partial}{\partial x} - i \frac{\partial}{\partial y} \right) \\ \frac{1}{2} \left(\frac{\partial}{\partial x} + i \frac{\partial}{\partial y} \right) \\ \frac{\partial}{\partial z} \end{bmatrix} = \begin{bmatrix} \partial_- \\ \partial_+ \\ \partial_z \end{bmatrix}. \quad (2.12)$$

Then, we can easily show that $\underline{\Omega} \cdot \nabla = \underline{\Omega}' \cdot \nabla'$, and this helps eliminate the imaginary terms in the moment equations.

2.1.3 Streaming term

By equations (2.8)–(2.12), we can derive the following streaming term:

$$\begin{aligned} & \int_{\mathbb{S}^2} \bar{Y}_\ell^m \underline{\Omega} \cdot \nabla F d\underline{\Omega} \\ &= \frac{1}{2} (-C_{\ell-1}^{m-1} F_{\ell-1}^{m-1} + D_{\ell+1}^{m-1} F_{\ell+1}^{m-1} + E_{\ell-1}^{m+1} F_{\ell-1}^{m+1} - G_{\ell+1}^{m+1} F_{\ell+1}^{m+1}),_x \\ &+ \frac{1}{2} i (C_{\ell-1}^{m-1} F_{\ell-1}^{m-1} - D_{\ell+1}^{m-1} F_{\ell+1}^{m-1} + E_{\ell-1}^{m+1} F_{\ell-1}^{m+1} - G_{\ell+1}^{m+1} F_{\ell+1}^{m+1}),_y \\ &+ (A_{\ell-1}^m F_{\ell-1}^m + B_{\ell+1}^m F_{\ell+1}^m),_z. \end{aligned} \quad (2.13)$$

2.1.4 P_N equations

Using equations (2.7) and (2.13) we can derive the following moment equations:

$$\begin{aligned} & F_\ell^m,_t + \frac{1}{2} (-C_{\ell-1}^{m-1} F_{\ell-1}^{m-1} + D_{\ell+1}^{m-1} F_{\ell+1}^{m-1} + E_{\ell-1}^{m+1} F_{\ell-1}^{m+1} - G_{\ell+1}^{m+1} F_{\ell+1}^{m+1}),_x \\ &+ \frac{1}{2} i (C_{\ell-1}^{m-1} F_{\ell-1}^{m-1} - D_{\ell+1}^{m-1} F_{\ell+1}^{m-1} + E_{\ell-1}^{m+1} F_{\ell-1}^{m+1} - G_{\ell+1}^{m+1} F_{\ell+1}^{m+1}),_y \\ &+ (A_{\ell-1}^m F_{\ell-1}^m + B_{\ell+1}^m F_{\ell+1}^m),_z + \sigma_t F_\ell^m = \sigma_s F_0^0 \delta_{\ell 0} \delta_{m 0}, \end{aligned} \quad (2.14)$$

for $0 \leq \ell \leq N$ and $-\ell \leq m \leq \ell$.

For the detailed derivation see [6].

2.1.5 Number of unknowns

The original P_N equations have the following moments F_ℓ^m where $\ell = 0, 1, \dots, N$, and $m = -\ell, \dots, 0, \dots, \ell$:

$$\begin{aligned}
 & F_0^0 \\
 & F_1^{-1} F_1^0 F_1^1 \\
 & F_2^{-2} F_2^{-1} F_2^0 F_2^1 F_2^2 \\
 & \vdots \\
 & F_{N-1}^{-N+1} F_{N-1}^{-N+2} \dots F_{N-1}^0 \dots F_{N-1}^{N-2} F_{N-1}^{N-1} \\
 & F_N^{-N} F_N^{-N+1} F_N^{-N+2} \dots F_N^0 \dots F_N^{N-2} F_N^{N-1} F_N^N.
 \end{aligned} \tag{2.15}$$

Hence the number of unknowns is

$$\sum_{\ell=0}^N \sum_{m=-\ell}^{\ell} 1 = N^2 + 2N + 1. \tag{2.16}$$

2.1.6 Reduced number of unknowns

By the following property of the spherical harmonic functions,

$$\bar{Y}_\ell^m = (-1)^m Y_\ell^{-m}, \tag{2.17}$$

we get

$$F_\ell^m(\underline{x}, t) = \int_{\mathbb{S}^2} \bar{Y}_\ell^m F(\underline{x}, \underline{\Omega}, t) d\underline{\Omega} = (-1)^m \int_{\mathbb{S}^2} Y_\ell^{-m} F(\underline{x}, \underline{\Omega}, t) d\underline{\Omega}, \tag{2.18}$$

and

$$\bar{F}_\ell^m(\underline{x}, t) = (-1)^m \int_{\mathbb{S}^2} \bar{Y}_\ell^{-m} F(\underline{x}, \underline{\Omega}, t) d\underline{\Omega} = (-1)^m F_\ell^{-m}. \tag{2.19}$$

Now we have the reduced moments:

$$\begin{aligned}
 & F_0^0 \\
 & F_1^0 \quad F_1^1 \\
 & F_2^0 \quad F_2^1 \quad F_2^2 \\
 & \vdots \qquad \ddots \\
 & F_{N-1}^0 \cdots \quad F_{N-1}^{N-2} \quad F_{N-1}^{N-1} \\
 & F_N^0 \quad \cdots \quad F_N^{N-2} \quad F_N^{N-1} \quad F_N^N,
 \end{aligned} \tag{2.20}$$

and reduced the number of unknowns to

$$\sum_{\ell=0}^N \sum_{m=0}^{\ell} 1 = \frac{1}{2}(N^2 + 3N) + 1. \tag{2.21}$$

2.1.7 Reduced moment equations

Finally, if we let $\sigma_t = \sigma_s = 1$, then the reduced moment equations with the reduced unknowns can be written as follows:

$$\underline{F}_{,t} + \underline{\underline{A}} \underline{F}_{,x} + \underline{\underline{B}} \underline{F}_{,z} = \underline{\underline{C}} \underline{F}, \tag{2.22}$$

where $\underline{\underline{A}}$ and $\underline{\underline{B}}$ are the P_N Jacobians that are diagonalizable with the same eigenvalues, $\underline{\underline{C}}$ is a diagonal matrix:

$$\underline{\underline{C}} = \begin{bmatrix} 0 & 0 & 0 & \cdots & 0 & 0 \\ 0 & -1 & 0 & \cdots & 0 & 0 \\ 0 & 0 & -1 & \cdots & 0 & 0 \\ \vdots & \vdots & \vdots & \ddots & \vdots & \vdots \\ 0 & 0 & 0 & \cdots & -1 & 0 \\ 0 & 0 & 0 & \cdots & 0 & -1 \end{bmatrix}, \tag{2.23}$$

and the moments are

$$\underline{F} = [F_0^0, F_1^0, F_2^0, \dots, F_N^0, F_1^1, \dots, F_N^1, \dots, F_N^N]^T. \tag{2.24}$$

2.1.7.1 P_1 Jacobians

The flux Jacobian matrices $\underline{\underline{A}}$ and $\underline{\underline{B}}$ in the equation (2.22) are given by

$$\underline{\underline{A}} = \left[\begin{array}{cc|c} 0 & 0 & -\sqrt{\frac{2}{3}} \\ 0 & 0 & 0 \\ \hline -\sqrt{\frac{1}{6}} & 0 & 0 \end{array} \right],$$

$$\underline{\underline{B}} = \left[\begin{array}{cc|c} 0 & \sqrt{\frac{1}{3}} & 0 \\ \sqrt{\frac{1}{3}} & 0 & 0 \\ \hline 0 & 0 & 0 \end{array} \right].$$

2.1.7.2 P_3 Jacobians

The flux Jacobian matrices $\underline{\underline{A}}$ and $\underline{\underline{B}}$ in the equation (2.22) are given by

$$\underline{\underline{A}} = \left[\begin{array}{cccc|ccc|cc|c} 0 & 0 & 0 & 0 & -\sqrt{\frac{2}{3}} & 0 & 0 & 0 & 0 & 0 \\ 0 & 0 & 0 & 0 & 0 & -\sqrt{\frac{2}{5}} & 0 & 0 & 0 & 0 \\ 0 & 0 & 0 & 0 & \sqrt{\frac{2}{15}} & 0 & -\sqrt{\frac{12}{35}} & 0 & 0 & 0 \\ 0 & 0 & 0 & 0 & 0 & \sqrt{\frac{6}{35}} & 0 & 0 & 0 & 0 \\ \hline -\sqrt{\frac{1}{6}} & 0 & \sqrt{\frac{1}{30}} & 0 & 0 & 0 & 0 & -\sqrt{\frac{1}{5}} & 0 & 0 \\ 0 & -\sqrt{\frac{1}{10}} & 0 & \sqrt{\frac{3}{70}} & 0 & 0 & 0 & 0 & -\sqrt{\frac{1}{7}} & 0 \\ 0 & 0 & -\sqrt{\frac{3}{35}} & 0 & 0 & 0 & 0 & \sqrt{\frac{1}{70}} & 0 & 0 \\ \hline 0 & 0 & 0 & 0 & -\sqrt{\frac{1}{5}} & 0 & \sqrt{\frac{1}{70}} & 0 & 0 & -\sqrt{\frac{3}{14}} \\ 0 & 0 & 0 & 0 & 0 & -\sqrt{\frac{1}{7}} & 0 & 0 & 0 & 0 \\ \hline 0 & 0 & 0 & 0 & 0 & 0 & 0 & -\sqrt{\frac{3}{14}} & 0 & 0 \end{array} \right],$$

$$\underline{\underline{B}} = \left[\begin{array}{cccc|ccc|cc|c} 0 & \sqrt{\frac{1}{3}} & 0 & 0 & 0 & 0 & 0 & 0 & 0 & 0 \\ \sqrt{\frac{1}{3}} & 0 & \sqrt{\frac{4}{15}} & 0 & 0 & 0 & 0 & 0 & 0 & 0 \\ 0 & \sqrt{\frac{4}{15}} & 0 & \sqrt{\frac{9}{35}} & 0 & 0 & 0 & 0 & 0 & 0 \\ 0 & 0 & \sqrt{\frac{9}{35}} & 0 & 0 & 0 & 0 & 0 & 0 & 0 \\ \hline 0 & 0 & 0 & 0 & 0 & \sqrt{\frac{1}{5}} & 0 & 0 & 0 & 0 \\ 0 & 0 & 0 & 0 & \sqrt{\frac{1}{5}} & 0 & \sqrt{\frac{8}{35}} & 0 & 0 & 0 \\ 0 & 0 & 0 & 0 & 0 & \sqrt{\frac{8}{35}} & 0 & 0 & 0 & 0 \\ \hline 0 & 0 & 0 & 0 & 0 & 0 & 0 & 0 & \sqrt{\frac{1}{7}} & 0 \\ 0 & 0 & 0 & 0 & 0 & 0 & 0 & \sqrt{\frac{1}{7}} & 0 & 0 \\ \hline 0 & 0 & 0 & 0 & 0 & 0 & 0 & 0 & 0 & 0 \end{array} \right].$$

2.2 Discrete Ordinates

In the discrete ordinate (S_N) method, the angular flux is calculated by using a finite number of discrete angular directions. In order to get a better approximation, we need to use an efficient quadrature set. The approximation of the total radiation flux, i.e., numerical integration of the angular flux over unit sphere (for the isotropic case) is the essential part of S_N method. The best known angular quadrature set in the S_N method is the level symmetric quadrature set(LQ_N), where the number of ordinate directions is $N(N + 2)$. The quadrature set is provided in [20, 45].

Although the level symmetric quadrature set is common, for $N \geq 20$ ($N_q \geq 440$ directions), there exist negative weights [19], which means that there is an upper limit of N . In order to construct a new solid angle quadrature set, one needs to consider the even moment conditions [42], and by adding more conditions, one might obtain new quadrature sets as in [19]. Comparison of different types of quadrature schemes in discrete ordinate method is provided in [30]. In spite of the limitation of LQ_N , throughout this thesis, LQ_N will be used for S_N method, although there have been many different quadrature schemes

developed [30].

The equation that describes the interaction of radiation with material is the Linear Boltzmann equation (LBE):

$$\begin{aligned} & \frac{1}{v} \psi_{,t}(\underline{r}, \underline{\Omega}, E, t) + \underline{\Omega} \cdot \nabla_{\underline{r}} \psi(\underline{r}, \underline{\Omega}, E, t) + \sigma_t(\underline{r}, E) \psi(\underline{r}, \underline{\Omega}, E, t) \\ &= \int_0^\infty \int_{4\pi} \sigma_s(\underline{r}, \underline{\Omega}' \cdot \underline{\Omega}, E' \rightarrow E) \psi(\underline{r}, \underline{\Omega}', E', t) d\underline{\Omega}' dE' \\ &+ \frac{\chi(\underline{r}, E)}{4\pi} \int_0^\infty \int_{4\pi} v \sigma_t(\underline{r}, E') \psi(\underline{r}, \underline{\Omega}', E', t) d\underline{\Omega}' dE' + \frac{Q(\underline{r}, E, t)}{4\pi}, \end{aligned} \quad (2.25)$$

and all the details of multi-group transport equation are provided in [38]. For brevity, we are focusing on the one energy isotropic-linear kinetic equation with unit speed, and we also neglect external sources. The external source term can be easily added later if necessary. Then the governing equation becomes:

$$f_{,t} + \underline{\Omega} \cdot \nabla_{\underline{r}} f = \frac{\sigma_s}{4\pi} \int_{\mathbb{S}^2} f d\Omega - \sigma_t f, \quad (2.26)$$

where $\underline{r} \in \mathbb{R}^3$ is position, $\underline{\Omega} \in \mathbb{S}^2$ is the direction of particle travel, and σ is the scattering cross section. Let $\{\underline{\Omega}_1, \dots, \underline{\Omega}_{N_q}\} \subset \mathbb{S}^2$ be a set of angular directions with corresponding weights w_1, \dots, w_{N_q} . The S_N approximation of (2.26) can be expressed as

$$f_{i,t} + \underline{\Omega} \cdot \nabla_{\underline{r}} f_i = \frac{\sigma_s}{4\pi} \sum_{i'=1}^{N_q} w_{i'} f_{i'} - \sigma_t f_i, \quad (2.27)$$

where $f_i(\underline{r}, t) \simeq f(\underline{r}, \underline{\Omega}_i, t)$ for $i = 1, \dots, N_q$.

CHAPTER 3. LINEAR HYPERBOLIC SYSTEMS

In this chapter, we provide the basic concepts of linear hyperbolic systems, since all of the methods, S_N , P_N , and the H_N^T scheme developed in Chapter 5, all produce linear hyperbolic systems.

3.1 1D Linear Hyperbolic Systems

Definition 3.1. A linear system:

$$\underline{q}_{,t} + \underline{\underline{A}}\underline{q}_{,x} = 0, \quad (3.1)$$

is hyperbolic if the $m \times m$ matrix $\underline{\underline{A}}$ is diagonalizable with only real eigenvalues with $\lambda^1 \leq \lambda^2 \leq \dots \leq \lambda^m$.

If $\underline{r}^1, \underline{r}^2, \dots, \underline{r}^m \in \mathbb{R}^m$ are nonzero eigenvector of $\underline{\underline{A}}$, i.e.,

$$\underline{\underline{A}}\underline{r}^p = \lambda^p \underline{r}^p \text{ for } p = 1, 2, \dots, m, \quad (3.2)$$

and linearly independent, then the matrix called diagonalizable. Then we have

$$\underline{\underline{R}}^{-1} \underline{\underline{A}} \underline{\underline{R}} = \underline{\underline{\Lambda}} \text{ and } \underline{\underline{A}} = \underline{\underline{R}} \underline{\underline{\Lambda}} \underline{\underline{R}}^{-1}, \quad (3.3)$$

where

$$\underline{\underline{\Lambda}} = \begin{bmatrix} \lambda^1 & & & \\ & \lambda^2 & & \\ & & \ddots & \\ & & & \lambda^m \end{bmatrix} \equiv \text{diag}(\lambda^1, \lambda^2, \dots, \lambda^m).$$

Now we can rewrite (5.18) as

$$\underline{\underline{R}}^{-1} \underline{q}_{,t} + \underline{\underline{R}}^{-1} \underline{\underline{A}} \underline{\underline{R}} \underline{\underline{R}}^{-1} \underline{q}_{,x} = 0. \quad (3.4)$$

This becomes

$$\underline{w}_{,t} + \underline{\underline{\Lambda}} \underline{w}_{,x} = 0, \quad (3.5)$$

where $\underline{w}(x, t) \equiv \underline{\underline{R}}^{-1} \underline{q}(x, t)$. This leads to decoupled m independent advection equations. For variable-coefficient or nonlinear hyperbolic systems, see LeVeque [40].

3.1.1 The Riemann problem for a linear system

The hyperbolic equation with a jump discontinuity initial condition,

$$\underline{q}_0(x) = \begin{cases} \underline{q}_l & \text{if } x < 0, \\ \underline{q}_r & \text{if } x > 0, \end{cases} \quad (3.6)$$

is so called the Riemann problem. Decompose \underline{q}_l and \underline{q}_r as

$$\underline{q}_l = \sum_{p=1}^m w_l^p \underline{r}^p \quad \text{and} \quad \underline{q}_r = \sum_{p=1}^m w_r^p \underline{r}^p. \quad (3.7)$$

Then

$$w^p(x, t) = \begin{cases} w_l^p & \text{if } x - \lambda^p t < 0, \\ w_r^p & \text{if } x - \lambda^p t > 0, \end{cases} \quad (3.8)$$

Assume that $P(x, t)$ is the maximum of p where $x - \lambda^p t > 0$, then

$$\underline{q}(x, t) = \sum_{p=1}^{P(x,t)} w_r^p \underline{r}^p + \sum_{p=P(x,t)+1}^m w_l^p \underline{r}^p. \quad (3.9)$$

The Rankine-Hugoniot jump condition is as follow:

$$(w_r^p - w_l^p) \underline{r}^p \equiv \alpha^p \underline{r}^p, \quad (3.10)$$

which can be derived from the conservation law. For multi-dimensional case, again, see [40].

3.1.2 The classical upwind method

For 1D linear hyperbolic systems, we have several waves that propagate with different speeds. In order to obtain a desirable numerical flux, we need to use the information of

the structure of the solution. The classical choice of the information from each direction is determined by the characteristic decomposition. We can update \underline{Q}_i by the following upwind scheme:

$$\underline{Q}_i^{n+1} = \underline{Q}_i^n - \frac{\Delta t}{\Delta x} \left[\underline{\underline{A}}^+ \left(\underline{Q}_i^n - \underline{Q}_{i-1}^n \right) + \underline{\underline{A}}^- \left(\underline{Q}_{i+1}^n - \underline{Q}_i^n \right) \right], \quad (3.11)$$

where

$$\underline{\underline{A}}^\pm = \underline{\underline{R}} \underline{\underline{\Lambda}}^\pm \underline{\underline{R}}^{-1}, \quad (3.12)$$

and

$$\underline{\underline{\Lambda}}^+ = \begin{bmatrix} \max(\lambda^1, 0) & & & \\ & \max(\lambda^2, 0) & & \\ & & \ddots & \\ & & & \max(\lambda^m, 0) \end{bmatrix}, \quad (3.13)$$

$$\underline{\underline{\Lambda}}^- = \begin{bmatrix} \min(\lambda^1, 0) & & & \\ & \min(\lambda^2, 0) & & \\ & & \ddots & \\ & & & \min(\lambda^m, 0) \end{bmatrix}. \quad (3.14)$$

3.2 2D Hyperbolic Linear Systems

Consider the following 2D constant-coefficient linear system:

$$\underline{q}_{,t} + \underline{\underline{A}} \underline{q}_{,x} + \underline{\underline{B}} \underline{q}_{,y} = 0 \quad (3.15)$$

Definition 3.2. Equation (3.15) is hyperbolic if

$$\widehat{\underline{\underline{A}}} := n^1 \underline{\underline{A}} + n^2 \underline{\underline{B}} \quad (3.16)$$

is diagonalizable with only real eigenvalues for all n^1 and n^2 such that $(n^1)^2 + (n^2)^2 = 1$.

CHAPTER 4. THE DISCONTINUOUS GALERKIN METHODS

In this chapter we review the discontinuous Galerkin (DG) methods and provide the notations we will use throughout this thesis.

4.1 A Brief History

The DG method was originally invented by Reed and Hill [51] to solve the neutron transport equation in 1973. The modern framework of DG methods was established by Cockburn, Shu, and their collaborators [14, 13, 12, 11, 15]. Zhang and Shu [60, 61, 62, 63, 64] have significantly improved high order DG method by adding structure-preserving properties such as maximum-principle-satisfying and positivity-preserving properties. Also, recently, Jiang and Liu [33] have developed the invariant-region-preserving DG scheme for multi-dimensional hyperbolic conservation law systems.

4.2 Discontinuous Galerkin Methods

The discontinuous Galerkin (DG) methods are finite element methods (FEM) that are applied to the weak form of the underlying partial differential equation. The main difference between the continuous Galerkin (CG) method and the DG method is the requirement of the continuity of the solution along the element interfaces. DG methods allow to use discontinuous solution at the cell edges. DG methods are very popular since these methods have better flexibility than standard finite element methods when it comes to the ability that can handle complex geometry, parallelization and p -adaptivity. DG methods are especially well suited for the hyperbolic partial differential equations (PDE) problems because these problems often require the ability to capture discontinuities at the cell interfaces.

Finite difference methods are easy to implement and fast, can achieve high-order, however it is hard to deal with complex geometry. While finite volume methods (FVM) can handle complex geometry, it is hard to achieve high-order on general grids. DG methods can combine the benefits of FEM and FVM, i.e., local high-order and flexible element of FEM and the conservation property of FVM [28].

One main characteristic of DG methods is that these methods use piecewise polynomial in each element. This allows the presence of discontinuous solutions at each cell interface. We first describe the DG methods for the 1D hyperbolic conservation law, and then the 2D hyperbolic conservation law on a Cartesian mesh. High-order can be achieved simply by choosing the appropriate maximum polynomial degree.

4.2.1 Hyperbolic conservation law in 1D

Consider the following hyperbolic balance law in one-dimension:

$$q_{,t}(x, t) + f_{,x}(q(x, t)) = \psi(q(x, t), x, t), \quad (4.1)$$

where $q : \mathbb{R} \times \mathbb{R}^+ \rightarrow \mathbb{R}^m$, $f : \mathbb{R}^m \rightarrow \mathbb{R}^m$ is a flux function, and $\psi(q, x, t)$ is a source term. (4.1) is called hyperbolic, if the flux Jacobian is diagonalizable with real eigenvalues, where the flux Jacobian of (4.1) is,

$$A(q(x, t)) = f_{,q}(q(x, t)). \quad (4.2)$$

In order to solve (4.1) using the discontinuous Galerkin (DG) method, we need to introduce the finite element space:

$$V^h = \{v^h \in L^2(\mathcal{D}) : v^h|_{\mathcal{T}} \in P^k(\mathcal{T}), \forall \mathcal{T} \in \mathcal{T}_h\}, \quad (4.3)$$

where \mathcal{T}_h is a collection of disjoint elements \mathcal{T} , $P^k(\mathcal{D})$ is the space of polynomials of degree at most k on a domain $\mathcal{D} \subset \mathbb{R}^m$. This finite element space can be chosen differently for each purpose. In this thesis, we will focus on a uniform Cartesian mesh for DG schemes for brevity, however, it can be replaced with any other mesh with a different finite element space.

Denote the domain by $\mathcal{D} = [a, b]$, and the number of cells on \mathcal{D} by m_x . Then the size of each element is $\Delta x = (b - a)/m_x$. Define the left edge of i -th element as $x_{i-1/2} = a + (i-1)\Delta x$, for $i = 1, 2, \dots, m_x + 1$, and center as $x_i = a + (i-1/2)\Delta x$, for $i = 1, 2, \dots, m_x$.

For simple representation, we transform the coordinate x in i -th element $\mathcal{T}_i = [x_{i-1/2}, x_{i+1/2}]$ into the interval $[-1, 1]$ by the following linear transformation:

$$x = x_i + \xi \frac{\Delta x}{2}. \quad (4.4)$$

We use the orthonormal Legendre polynomials as basis functions for each cell. The set of Legendre polynomials \mathbb{L} is as follow:

$$\begin{aligned} \mathbb{L} := & \left\{ 1, \sqrt{3}\xi, \frac{\sqrt{5}}{2}(3\xi^2 - 1), \frac{\sqrt{7}}{2}(5\xi^3 - 3\xi), \frac{3}{8}(35\xi^4 - 30\xi^2 + 3), \right. \\ & \frac{\sqrt{11}}{8}(63\xi^5 - 70\xi^3 + 15\xi), \frac{\sqrt{13}}{16}(231\xi^6 - 315\xi^4 + 105\xi^2 - 5), \\ & \frac{\sqrt{15}}{16}(429\xi^7 - 693\xi^5 + 315\xi^3 - 35\xi), \frac{\sqrt{17}}{128}(6435\xi^8 - 12012\xi^6 + 6930\xi^4 - 1260\xi^2 + 35), \\ & \frac{\sqrt{19}}{128}(12155\xi^9 - 25740\xi^7 + 18018\xi^5 - 4620\xi^3 + 315\xi), \\ & \left. \frac{\sqrt{21}}{256}(46189\xi^{10} - 109395\xi^8 + 90090\xi^6 - 30030\xi^4 + 3465\xi^2 - 63), \dots \right\}. \end{aligned} \quad (4.5)$$

Now $\varphi^\ell \in \mathbb{L}$ satisfies the following orthonormality property:

$$\frac{1}{2} \int_{-1}^1 \varphi^\ell(\xi) \varphi^{\ell'}(\xi) d\xi = \delta_{\ell\ell'}, \quad (4.6)$$

where $\delta_{\ell\ell'}$ is the Kronecker delta function as usual.

Now our goal is finding approximate solutions of (4.1) using the discontinuous Galerkin expansion:

$$q^h(x, t) \Big|_{\mathcal{T}_i} := q_i^h(\xi, t) = \sum_{\ell=1}^M Q_i^\ell(t) \varphi^\ell(\xi), \quad (4.7)$$

where M is the desired order of accuracy in space. The coefficients $Q_i^\ell(t)$ can be obtained by

$$Q_i^\ell(t) = \frac{1}{2} \int_{-1}^1 q_i^h(\xi, t) \varphi^\ell(\xi) d\xi. \quad (4.8)$$

Now multiply (4.1) by a test function $\varphi(x)$, then integrate over the i -th element $\mathcal{T}_i = [x_{i-1/2}, x_{i+1/2}]$ to get

$$\frac{1}{\Delta x} \int_{\mathcal{T}_i} q_{,t}(x, t) \varphi(x) dx + \frac{1}{\Delta x} \int_{\mathcal{T}_i} f_{,x}(q(x, t)) \varphi(x) dx = \frac{1}{\Delta x} \int_{\mathcal{T}_i} \psi(q(x, t), x, t) \varphi(x) dx. \quad (4.9)$$

By integration by parts, we have

$$\begin{aligned} \frac{1}{\Delta x} \int_{\mathcal{T}_i} f_{,x}(q(x, t)) \varphi(x) dx &= \frac{1}{\Delta x} \left[\hat{f}(q(x_{i+\frac{1}{2}}, t)) \varphi(x_{i+\frac{1}{2}}) - \hat{f}(q(x_{i-\frac{1}{2}}, t)) \varphi(x_{i-\frac{1}{2}}) \right] \\ &\quad - \frac{1}{\Delta x} \int_{\mathcal{T}_i} f(q(x, t)) \varphi_{,x}(x) dx, \end{aligned} \quad (4.10)$$

where \hat{f} is the numerical flux, which will be discussed in Section 4.2.4. Finally, we get

$$\begin{aligned} \frac{1}{\Delta x} \int_{\mathcal{T}_i} q_{,t}(x, t) \varphi(x) dx + \frac{1}{\Delta x} \left[\hat{f}(q(x_{i+\frac{1}{2}}, t)) \varphi(x_{i+\frac{1}{2}}) - \hat{f}(q(x_{i-\frac{1}{2}}, t)) \varphi(x_{i-\frac{1}{2}}) \right] \\ - \frac{1}{\Delta x} \int_{\mathcal{T}_i} f(q(x, t)) \varphi_{,x}(x) dx = \frac{1}{\Delta x} \int_{\mathcal{T}_i} \psi(q(x, t), x, t) \varphi(x) dx. \end{aligned} \quad (4.11)$$

Replace q by q_i^h and $\varphi(x)$ by $\varphi^{\ell'}(\xi)$ in (4.11) to get

$$\begin{aligned} \frac{1}{2} \int_{-1}^1 q_{i,t}^h(\xi, t) \varphi^{\ell'}(\xi) d\xi + \frac{1}{\Delta x} \left[\hat{f}(q(x_{i+\frac{1}{2}}, t)) \varphi^{\ell'}(1) - \hat{f}(q(x_{i-\frac{1}{2}}, t)) \varphi^{\ell'}(-1) \right] \\ - \frac{1}{\Delta x} \int_{-1}^1 f(q_i^h(\xi, t)) \varphi_{,\xi}^{\ell'}(\xi) d\xi = \frac{1}{2} \int_{-1}^1 \psi(q_i^h(\xi, t), \xi, t) \varphi^{\ell'}(\xi) d\xi, \end{aligned} \quad (4.12)$$

therefore, we have

$$\begin{aligned} \frac{1}{2} \int_{-1}^1 \sum_{\ell=1}^M Q_{i,t}^{\ell}(t) \varphi^{\ell}(\xi) \varphi^{\ell'}(\xi) d\xi + \frac{1}{\Delta x} \left[\hat{f}(q(x_{i+\frac{1}{2}}, t)) \varphi^{\ell'}(1) - \hat{f}(q(x_{i-\frac{1}{2}}, t)) \varphi^{\ell'}(-1) \right] \\ - \frac{1}{\Delta x} \int_{-1}^1 f(q_i^h(\xi, t)) \varphi_{,\xi}^{\ell'}(\xi) d\xi = \frac{1}{2} \int_{-1}^1 \psi(q_i^h(\xi, t), \xi, t) \varphi^{\ell'}(\xi) d\xi. \end{aligned} \quad (4.13)$$

A simple representation of (4.13) is

$$Q_{i,t}^{\ell'} = -\frac{1}{\Delta x} \left[F_{i+\frac{1}{2}} - F_{i-\frac{1}{2}} \right] + A_i^{\ell'} + \Psi_i^{\ell'}, \quad (4.14)$$

for $\ell' = 1, 2, \dots, M$, where

$$F_{i \pm \frac{1}{2}} = \hat{f}(q(x_{i \pm \frac{1}{2}}, t)) \varphi^{\ell'}(\pm 1), \quad (4.15)$$

$$A_i^{\ell'} = \frac{1}{\Delta x} \int_{-1}^1 f(q_i^h(\xi, t)) \varphi_{,\xi}^{\ell'}(\xi) d\xi, \quad (4.16)$$

and

$$\Psi_i^\ell = \frac{1}{2} \int_{-1}^1 \psi(q_i^h(\xi, t), \xi, t) \varphi^\ell(\xi) d\xi. \quad (4.17)$$

The integration over $[-1, 1]$ in (4.16) and (4.17) can be computed by the quadrature rule in 4.2.3

4.2.2 Hyperbolic conservation law in 2D

Consider the following hyperbolic conservation law in two-dimensions:

$$q_{,t}(\underline{x}, t) + f_{,x}(q(\underline{x}, t)) + g_{,y}(q(\underline{x}, t)) = \psi(q(\underline{x}, t), \underline{x}, t), \quad (4.18)$$

where $q : \mathbb{R}^2 \times \mathbb{R}^+ \rightarrow \mathbb{R}^m$, $f : \mathbb{R}^m \rightarrow \mathbb{R}^m$ and $g : \mathbb{R}^m \rightarrow \mathbb{R}^m$ are flux functions, and $\psi(q(\underline{x}, t), \underline{x}, t)$ is a source term. Let the flux vector be $\underline{f}(q) = [f(q), g(q)]$, and the unit vector be $\underline{n}(s) = (n^x, n^y)$ in \mathbb{R}^2 . Now define

$$\check{f}(q) := \underline{n} \cdot \underline{f}(q) = n^x f(q) + n^y g(q). \quad (4.19)$$

and

$$\check{A} := \underline{n} \cdot \underline{A} = n^x A + n^y B, \quad (4.20)$$

where $\underline{A} = (A, B)$, $A = f_{,q}$ and $B = g_{,q}$. The equation (4.18) is called hyperbolic, if the linear combination of flux Jacobians, i.e. \check{A} , is diagonalizable with real eigenvalues.

Now define a uniform Cartesian mesh on the domain $\mathcal{D} = [a, b] \times [c, d]$. Then the mesh sizes $\Delta x = \frac{b-a}{m_x}$, $\Delta y = \frac{d-c}{m_y}$, and the center of (i, j) -th element \mathcal{T}_{ij} are (x_i, y_j) where

$$x_i = a + \left(i - \frac{1}{2}\right) \Delta x, \quad (4.21)$$

and

$$y_j = c + \left(j - \frac{1}{2}\right) \Delta y, \quad (4.22)$$

with $1 \leq i \leq m_x$ and $1 \leq j \leq m_y$.

As in one-dimensional case, we need to introduce the finite element space again:

$$V^h = \{v^h \in L^2(\mathcal{D}) : v^h|_{\mathcal{T}} \in P^k(\mathcal{T}), \forall \mathcal{T} \in \mathcal{T}_h\}. \quad (4.23)$$

Now we transform the coordinate (x, y) in (i, j) -th element $\mathcal{T}_{ij} = [x_{i-1/2}, x_{i+1/2}] \times [y_{j-1/2}, y_{j+1/2}]$ into the cell $[-1, 1] \times [-1, 1]$ by the following linear transformation:

$$x = x_i + \xi \frac{\Delta x}{2}, \quad (4.24)$$

and

$$y = y_j + \eta \frac{\Delta y}{2}. \quad (4.25)$$

We use the orthonormal Legendre polynomials as basis functions for each cell. The set of Legendre polynomials \mathbb{L} is as follow:

$$\begin{aligned} \mathbb{L} := \left\{ 1, \sqrt{3}\xi, \sqrt{3}\eta, 3\xi\eta, \frac{\sqrt{5}}{2}(3\xi^2 - 1), \frac{\sqrt{5}}{2}(3\eta^2 - 1), \right. \\ \frac{\sqrt{15}}{2}\eta(3\xi^2 - 1), \frac{\sqrt{15}}{2}\xi(3\eta^2 - 1), \frac{\sqrt{7}}{2}(5\xi^3 - 3\xi), \frac{\sqrt{7}}{2}(5\eta^3 - 3\eta), \\ \frac{\sqrt{21}}{2}\eta(5\xi^3 - 3\xi), \frac{\sqrt{21}}{2}\xi(5\eta^3 - 3\eta), \frac{5}{4}(3\xi^2 - 1)(3\eta^2 - 1), \\ \left. \frac{3}{8}(35\xi^4 - 30\xi^2 + 3), \frac{3}{8}(35\eta^4 - 30\eta^2 + 3), \dots \right\}. \end{aligned} \quad (4.26)$$

Now $\varphi^\ell(\xi, \eta) \in \mathbb{L}$ satisfies the following orthonormal property:

$$\frac{1}{4} \int_{-1}^1 \int_{-1}^1 \varphi^\ell(\xi, \eta) \varphi^{\ell'}(\xi, \eta) d\xi d\eta = \delta_{\ell\ell'}. \quad (4.27)$$

Our goal is finding approximate solutions of (4.18) using the discontinuous Galerkin expansion:

$$q^h(x, y, t) \Big|_{\mathcal{T}_{ij}} := q_{ij}^h(\xi, \eta, t) = \sum_{\ell=1}^N Q_{ij}^\ell(t) \varphi^\ell(\xi, \eta), \quad (4.28)$$

where $N = \frac{M(M+1)}{2}$ and M is the desired order of accuracy in space. The coefficients $Q_{ij}^\ell(t)$ can be obtained by

$$Q_{ij}^\ell(t) = \frac{1}{4} \int_{-1}^1 \int_{-1}^1 q_{ij}^h(\xi, \eta, t) \varphi^\ell(\xi, \eta) d\xi d\eta. \quad (4.29)$$

For simplicity, we will assume that the source term $\psi(q, x, t) = 0$ in (4.18). Now multiply (4.18) with $\psi(q, x, t) = 0$, by a test function $\varphi(x, y)$, then integrate over the (i, j) -th element

$\mathcal{T}_{ij} = [x_{i-1/2}, x_{i+1/2}] \times [y_{j-1/2}, y_{j+1/2}]$ to get

$$\frac{1}{\Delta x \Delta y} \int_{\mathcal{T}_{ij}} q_t \varphi \, dx \, dy + \frac{1}{\Delta x \Delta y} \int_{\mathcal{T}_{ij}} \nabla \underline{f}(q) \cdot \varphi \, dx \, dy = 0. \quad (4.30)$$

Integrating (4.30) by parts, we have

$$\frac{1}{\Delta x \Delta y} \int_{\mathcal{T}_{ij}} q_t \varphi \, dx \, dy + \frac{1}{\Delta x \Delta y} \int_{\partial \mathcal{T}_{ij}} \varphi \hat{n} \cdot \underline{f}(q) \, ds - \frac{1}{\Delta x \Delta y} \int_{\mathcal{T}_{ij}} \nabla \varphi \cdot \underline{f}(q) \, dx \, dy = 0, \quad (4.31)$$

where

$$\underline{f}(q) = (f(q), g(q)). \quad (4.32)$$

The second term in (4.31) can be rewritten as

$$\begin{aligned} & \frac{1}{\Delta x \Delta y} \int_{\partial \mathcal{T}_{ij}} \varphi \hat{n} \cdot \underline{f}(q) \, ds \\ &= \frac{1}{\Delta x \Delta y} \left[\int_{x_{i-\frac{1}{2}}}^{x_{i+\frac{1}{2}}} \varphi(x, y_{j-\frac{1}{2}}) n^y g(q) \, dx + \int_{y_{j-\frac{1}{2}}}^{y_{j+\frac{1}{2}}} \varphi(x_{i+\frac{1}{2}}, y) n^x f(q) \, dy \right. \\ & \quad \left. - \int_{x_{i-\frac{1}{2}}}^{x_{i+\frac{1}{2}}} \varphi(x, y_{j+\frac{1}{2}}) n^y g(q) \, dx - \int_{y_{j-\frac{1}{2}}}^{y_{j+\frac{1}{2}}} \varphi(x_{i-\frac{1}{2}}, y) n^x f(q) \, dy \right]. \end{aligned} \quad (4.33)$$

Plugging (4.33) into (4.31), replacing q by q_{ij}^h , and $\varphi(x, y)$ by $\varphi^{\ell'}(\xi, \eta)$, we get

$$\begin{aligned} Q_{ij,t}^{\ell'} &+ \frac{1}{2} \left[\frac{1}{\Delta y} \int_{-1}^1 \left(\varphi^{\ell'}(\xi, -1) \hat{g}(q_{ij}^h(\xi, -1, t)) - \varphi^{\ell'}(\xi, 1) \hat{g}(q_{ij}^h(\xi, 1, t)) \right) d\xi \right. \\ & \quad \left. + \frac{1}{\Delta x} \int_{-1}^1 \left(\varphi^{\ell'}(1, \eta) \hat{f}(f_{ij}^h(1, \eta, t)) - \varphi^{\ell'}(-1, \eta) \hat{f}(q_{ij}^h(-1, \eta, t)) \right) d\eta \right] \\ & - \frac{1}{2} \int_{-1}^1 \int_{-1}^1 \left(\frac{1}{\Delta x} \varphi_{,\xi}^{\ell'} f(q_{ij}^h) + \frac{1}{\Delta y} \varphi_{,\eta}^{\ell'} g(q_{ij}^h) \right) d\xi d\eta = 0. \end{aligned} \quad (4.34)$$

Therefore, we have

$$Q_{ij,t}^{\ell'} = A_{ij}^{\ell'} + B_{ij}^{\ell'}, \quad (4.35)$$

for $\ell' = 1, 2, \dots, N = \frac{M(M+1)}{2}$, where

$$A_{ij}^{\ell'} = \frac{1}{2} \int_{-1}^1 \int_{-1}^1 \left(\frac{1}{\Delta x} \varphi_{,\xi}^{\ell'} f(q_{ij}^h) + \frac{1}{\Delta y} \varphi_{,\eta}^{\ell'} g(q_{ij}^h) \right) d\xi d\eta, \quad (4.36)$$

and

$$\begin{aligned} B_{ij}^{\ell'} &= -\frac{1}{2} \left[\frac{1}{\Delta y} \int_{-1}^1 \left(\varphi^{\ell'}(\xi, -1) \hat{g}(q_{ij}^h(\xi, -1, t)) - \varphi^{\ell'}(\xi, 1) \hat{g}(q_{ij}^h(\xi, 1, t)) \right) d\xi \right. \\ & \quad \left. + \frac{1}{\Delta x} \int_{-1}^1 \left(\varphi^{\ell'}(1, \eta) \hat{f}(f_{ij}^h(1, \eta, t)) - \varphi^{\ell'}(-1, \eta) \hat{f}(q_{ij}^h(-1, \eta, t)) \right) d\eta \right]. \end{aligned} \quad (4.37)$$

Again, the numerical fluxes \hat{f} and \hat{g} can be computed by the formulas in 4.2.4. The integration over $[-1, 1]$ in (4.34) can be computed by the quadrature rule in 4.2.3

4.2.3 Quadrature rules

The quadrature rules are used in our numerical scheme for the integration. The Gauss-Legendre quadrature rule is used in most cases and the Gauss-Lobatto quadrature rule is used only for the positivity-preserving limiters in Chapter 5.

4.2.3.1 Gauss-Legendre

A quadrature rule is an approximation of the definite integral of a given function. There are various types of quadrature rules, but the most popular quadrature rule is the Gauss-Legendre quadrature rule. Legendre quadrature is exact for the polynomials up to degree $2n - 1$, where n is the number of quadrature points.

Gauss-Legendre quadrature rules satisfy the following:

$$\int_{-1}^1 f(x)dx = \sum_{j=1}^n w_j f(x_j) + R_n, \quad (4.38)$$

where x_j are zeros of the Legendre polynomial $P_n(x)$ in the interval $(-1, 1)$, and the Gauss quadrature weights w_j are given by [1]:

$$w_j = \frac{2}{(1-x_j)^2[P'_n(x_j)]^2}, \quad (4.39)$$

and the remainder R_n is as follows [29]:

$$R_n = \frac{2^{2n+1}(n!)^4}{(2n+1)[(2n)!]^3} f^{(2n)}(\xi), \quad -1 < \xi < 1. \quad (4.40)$$

4.2.3.2 Gauss-Lobatto

The main difference between Gauss-Legendre and Gauss-Lobatto quadrature rules is that the Lobatto quadrature include the two end points of the integration interval. Lobatto quadrature is exact for polynomials up to degree $2n-3$, where n is the number of quadrature

points [50]. Lobatto quadrature rule was especially used in [60, 61, 62, 63, 64] for the structure-preserving limiters.

Gauss-Lobatto quadrature rules satisfy the following:

$$\int_{-1}^1 f(x)dx = \frac{2}{n(n-1)}[f(-1) + f(1)] + \sum_{j=2}^{n-1} w_j f(x_j) + R_n, \quad (4.41)$$

where x_j are zeros of $P'_{n-1}(x)$, weights w_j are given by

$$w_j = \frac{2}{n(n-1)[P_{n-1}(x_j)]^2}, \quad x_j \neq \pm 1, \quad (4.42)$$

and the remainder R_n is as follows [29]:

$$R_n = \frac{-n(n-1)^3 2^{2n-1} [(n-2)!]^4}{(2n-1)[(2n-2)!]^3} f^{(2n-2)}(\xi), \quad -1 < \xi < 1. \quad (4.43)$$

4.2.4 Numerical flux

The discontinuous Galerkin (DG) methods use piecewise polynomial basis functions that are discontinuous at the cell interfaces, thus, a numerical flux must be defined at each element interface. By the appropriate choice of a numerical flux, one can achieve a linearly stable numerical scheme. A comparison of numerical fluxes for the Euler and Navier-Stokes equations can be found in [56]. Consider the following Riemann problem that is governed by the one-dimensional inviscid flow equations

$$\underline{q}_t + \underline{f}(\underline{q})_{,x} = 0, \quad (4.44)$$

with the initial data

$$\underline{q}_0(x) = \begin{cases} \underline{q}_l & \text{if } x < 0, \\ \underline{q}_r & \text{if } x > 0, \end{cases} \quad (4.45)$$

If $\underline{Q}(x/t; \underline{q}_l, \underline{q}_r)$ is the solution to (4.44), we have the Godunov's flux formula which is the interface flux:

$$\underline{f}(\underline{q}_l, \underline{q}_r) = \underline{f}\left(\underline{Q}(0; \underline{q}_l, \underline{q}_r)\right). \quad (4.46)$$

4.2.4.1 Roe flux [52]

Consider the linearized version of (4.44) with initial data (4.45) :

$$\underline{q}_{,t} + \widehat{\underline{A}}(\underline{q}_l, \underline{q}_r) \underline{q}_{,x} = 0, \quad (4.47)$$

where $\widehat{\underline{A}}(\underline{q}_l, \underline{q}_r)$ satisfies

- $\widehat{\underline{A}}(\underline{q}, \underline{q}) = \underline{A}(\underline{q})$, where $\underline{A}(\underline{q})$ is the Jacobian of $\underline{f}(\underline{q})$,
- $\widehat{\underline{A}}(\underline{q}_l, \underline{q}_r)$ has real eigenvalues and a complete set of eigenvectors,
- $\widehat{\underline{A}}(\underline{q}_l, \underline{q}_r) \cdot (\underline{q}_r - \underline{q}_l) = \underline{f}(\underline{q}_r) - \underline{f}(\underline{q}_l)$.

The numerical flux based on this gives

$$\underline{f}(\underline{q}_l, \underline{q}_r) = \frac{1}{2} \left\{ \underline{f}(\underline{q}_l) + \underline{f}(\underline{q}_r) \right\} - \frac{1}{2} |A(\underline{q}_l, \underline{q}_r)| \cdot (\underline{q}_r - \underline{q}_l). \quad (4.48)$$

4.2.4.2 Osher flux [46]

The Osher flux is an upwind finite difference and finite element methods that approximate nonlinear PDEs. This numerical flux is given by the formula:

$$\underline{f}(\underline{q}_l, \underline{q}_r) = \frac{1}{2} \left\{ \underline{f}(\underline{q}_l) + \underline{f}(\underline{q}_r) \right\} - \frac{1}{2} \int_{\underline{q}_l}^{\underline{q}_r} |A(\underline{q})| d\underline{q}. \quad (4.49)$$

4.2.4.3 Harten-Lax/Roe flux [26]

Harten and Lax used a weighted wave speed $V(\underline{q}_l, \underline{q}_r)$ in their numerical flux. Later, Roe used $|V(\underline{q}_l, \underline{q}_r)|$ instead of the whole dissipation matrix [57]. The formula is given by

$$\underline{f}(\underline{q}_l, \underline{q}_r) = \frac{1}{2} \left\{ \underline{f}(\underline{q}_l) + \underline{f}(\underline{q}_r) \right\} - \frac{1}{2} |V(\underline{q}_l, \underline{q}_r)| \cdot (\underline{q}_r - \underline{q}_l), \quad (4.50)$$

where

$$V(\underline{q}_l, \underline{q}_r) = \frac{(w(\underline{q}_r) - w(\underline{q}_l)) \cdot (\underline{f}(\underline{q}_r) - \underline{f}(\underline{q}_l))}{(w(\underline{q}_r) - w(\underline{q}_l)) \cdot (\underline{q}_r - \underline{q}_l)}, \quad (4.51)$$

and $w(\underline{q})$ is the gradient of an entropy.

4.2.4.4 Van Leer flux [57]

Van Leer flux has a property that the dissipation disappears in steady shocks. The formula is as follows:

$$\underline{f}(\underline{q}_l, \underline{q}_r) = \frac{1}{2} \left\{ \underline{f}(\underline{q}_l) + \underline{f}(\underline{q}_r) \right\} - \frac{1}{2} \int_{\underline{q}_l}^{\underline{q}_r} |B(\underline{q})| d\underline{q}, \quad (4.52)$$

where

$$|B(\underline{q})| \equiv B^+(\underline{q}) - B^-(\underline{q}). \quad (4.53)$$

4.2.4.5 Rusanov/Davis/Yee flux [53]

In this numerical flux, the dissipation matrix $Q(\underline{q}_l, \underline{q}_r)$ is a spectral radius of $A(\underline{q}_l, \underline{q}_r)$.

The numerical flux is given by the following formula:

$$\underline{f}(\underline{q}_l, \underline{q}_r) = \frac{1}{2} \left\{ \underline{f}(\underline{q}_l) + \underline{f}(\underline{q}_r) \right\} - \frac{1}{2} \max_k |a^{(k)}(\underline{q}_l, \underline{q}_r)| \cdot (\underline{q}_r - \underline{q}_l), \quad (4.54)$$

where $\max_k |a^{(k)}(\underline{q}_l, \underline{q}_r)|$ is a spectral radius of $A(\underline{q}_l, \underline{q}_r)$. Also, a constant C can be used to reduce dissipation level:

$$\underline{f}(\underline{q}_l, \underline{q}_r) = \frac{1}{2} \left\{ \underline{f}(\underline{q}_l) + \underline{f}(\underline{q}_r) \right\} - C \max_k |a^{(k)}(\underline{q}_l, \underline{q}_r)| \cdot (\underline{q}_r - \underline{q}_l), \quad (4.55)$$

More details for other fluxes can be found in [57, 53, 18, 59].

4.3 Time integration

In our numerical scheme, we use explicit time integration. Especially, we use the low-storage strong stability-preserving explicit Runge-Kutta (SSP-RK) method of Ketcheson [35]. Here we study the explicit RK scheme first, and then study the diagonally implicit RK method (DIRK) [3].

4.3.1 Explicit Runge-Kutta methods

Consider the following ODEs

$$\underline{y}' = \underline{f}(t, \underline{y}), \quad t \geq t_0, \quad \underline{y}(t_0) = \underline{y}_0. \quad (4.56)$$

Integrating (4.56) from t_n to $t_{n+1} = t_n + \Delta t$, we get

$$\underline{y}(t_{n+1}) = \underline{y}(t_n) + \int_{t_n}^{t_{n+1}} \underline{f}(\tau, \underline{y}(\tau)) d\tau = \underline{y}(t_n) + \Delta t \int_0^1 \underline{f}(t_n + \Delta t \tau, \underline{y}(t_n + \Delta t \tau)) d\tau. \quad (4.57)$$

Then use a quadrature rule to replace the second integral. We can get

$$\underline{y}_{n+1} = \underline{y}_n + \Delta t \sum_{j=1}^{\nu} b_j \underline{f}(t_n + c_j \Delta t, \underline{y}(t_n + c_j \Delta t)), \quad n = 0, 1, \dots. \quad (4.58)$$

Let $\xi_j = \underline{y}(t_n + c_j \Delta t)$, $j = 1, 2, \dots, \nu$ and $c_1 = 0$. Then

$$\begin{aligned} \underline{\xi}_1 &= \underline{y}_n, \\ \underline{\xi}_2 &= \underline{y}_n + \Delta t a_{2,1} \underline{f}(t_n, \underline{\xi}_1), \\ \underline{\xi}_3 &= \underline{y}_n + \Delta t [a_{3,1} \underline{f}(t_n, \underline{\xi}_1) + a_{3,2} \underline{f}(t_n + c_2 \Delta t, \underline{\xi}_2)], \\ &\vdots \\ \underline{\xi}_\nu &= \underline{y}_n + \Delta t \sum_{i=1}^{\nu-1} a_{\nu,i} \underline{f}(t_n + c_i \Delta t, \underline{\xi}_i), \\ \underline{y}_{n+1} &= \underline{y}_n + \Delta t \sum_{j=1}^{\nu} b_j \underline{f}(t_n + c_j \Delta t, \underline{\xi}_j). \end{aligned} \quad (4.59)$$

We represent the method by a Butcher tableau:

$$\begin{array}{c|ccccc} \underline{c} & \underline{\underline{A}} \\ \hline & \underline{b}^T \end{array},$$

i.e.,

$$\begin{array}{c|ccccc} c_1 & a_{11} & a_{12} & \cdots & a_{1s} \\ c_2 & a_{21} & a_{22} & \cdots & a_{2s} \\ \vdots & \vdots & \vdots & \ddots & \vdots \\ c_s & a_{s1} & a_{s2} & \cdots & a_{ss} \\ \hline & b_1 & b_2 & \cdots & b_s \end{array}$$

and if the method is explicit, we have

0					
c_2	a_{21}				
c_3	a_{31}	a_{32}			
\vdots	\vdots	\vdots	\ddots		
c_s	a_{s1}	a_{s2}	\cdots	$a_{s,s-1}$	
	b_1	b_2	\cdots	b_{s-1}	b_s

For example,

- Euler's method:

0	0	
	1	

- Heun's method:

0	0	0	
1	1	0	
	1/2	1/2	

- RK4 method:

0	0	0	0	0
1/2	1/2	0	0	0
1/2	0	1/2	0	0
1	0	0	1	0
	1/6	1/3	1/3	1/6

4.3.2 Strong-stability preserving integrators

These versions of the Runge-Kutta method were originally called the TVD (total variation diminishing) time discretizations in [54], but later renamed to the SSP (strong stability preserving) time discretizations in [24]. Consider the following systems of ODEs

$$u_{,t} = L(u), \quad (4.60)$$

which is derived by the method of lines approximation of the hyperbolic conservation law:

$$u_{,t} = -f(u)_{,x}, \quad (4.61)$$

In [55], the m -stage Runge-Kutta method for (4.60) is as follow:

$$\begin{aligned} u^{(0)} &= u^n, \\ u^{(i)} &= \sum_{k=0}^{i-1} \left(\alpha_{i,k} u^{(k)} + \Delta t \beta_{i,k} L(u^{(k)}) \right), \quad \alpha_{i,k} \geq 0, \quad i = 1, \dots, m, \\ u^{(n+1)} &= u^{(m)}. \end{aligned} \quad (4.62)$$

If the strong forward Euler time discretization,

$$u^{n+1} = u^n + \Delta t L(u^n), \quad (4.63)$$

is strongly stable under the CFL condition $\Delta t \leq \Delta t_{FE}$, then the Runge-Kutta method (4.62) with $\beta_{i,k} \geq 0$ is strong stability preserving (SSP), provided that

$$\Delta t \leq c \Delta t_{FE}, \quad c = \min_{i,k} \frac{\alpha_{i,k}}{\beta_{i,k}}. \quad (4.64)$$

See [55] for more details.

4.3.3 Diagonally implicit Runge-Kutta methods

A review of diagonally implicit Runge-Kutta methods can be found in [34]. The diagonally implicit Runge-Kutta (DIRK) method is one the most popular implicit Runge-Kutta (IRK) method since it is relatively easy to implement. It is known that constructing high order DIRK methods having both the stability and the necessary order is very difficult [25]. The third order of DIRK is known that it gives the best computational efficiency among first-, third-, and fifth-order space-time discretizations for solving radiative transport problem [16]. Thus we will cover here only second-order two-stage DIRK and third-order three-stage DIRK methods that can be found in [3].

Definition 4.1. [49] “A RK-method is *S-stable* if for any bounded function $g : [0, T] \rightarrow \mathbb{R}$ that has a bounded derivative, and any positive constant λ_0 , there exists a positive constant h_0 such that the numerical solution (y_n) to the equation

$$y' = g'(t) + \lambda(y - g(t)), \quad (4.65)$$

satisfies

$$\left| \frac{y_{n+1} - g(t_{n+1})}{y_n - g(t_n)} \right| < 1, \quad (4.66)$$

provided $y_n \neq g(t_n)$, for all $0 < h < h_0$ and all $\lambda \in \mathbb{C}$ with $\operatorname{Re}(-\lambda) \geq \lambda_0$. A RK method is *strongly S-stable* if

$$\frac{y_{n+1} - g(t_{n+1})}{y_n - g(t_n)} \rightarrow 0, \quad (4.67)$$

as $\operatorname{Re}(-\lambda) \rightarrow \infty$ for all $h > 0$ such that $[t_n, t_{n+1}] \subset [0, T]$. Notice that an *S-stable* method is *A-stable* if we take $g \equiv 0$.”

The following are the Butcher tableau for the *S-stable* DIRK methods with two stages and three stages, respectively [3].

- Two-stage DIRK method:

α	α	0	
1	$1 - \alpha$	α	
		1 - α	α

$$\text{where } \alpha = \frac{2 \pm \sqrt{2}}{2}.$$

- Three-stage DIRK method:

α	α	0	0	
τ_2	$\tau_2 - \alpha$	α	0	
1	b_1	b_2	α	
		b_1	b_2	α

where α is the root of $x^3 - 3x^2 + \frac{3}{2}x - \frac{1}{6} = 0$ lying in $(\frac{1}{6}, \frac{1}{2})$,

$$\tau_2 = (1 + \alpha)/2,$$

$$b_1 = -(6\alpha^2 - 16\alpha + 1)/4, \text{ and}$$

$$b_2 = (6\alpha^2 - 20\alpha + 5)/4.$$

CHAPTER 5. THE H_N^T APPROXIMATION TO THE LINEAR KINETIC EQUATION

This chapter contains the main result of this work: the introduction and development of the H_N^T approximation of the radiative transfer equations. All the numerical calculations using this approximation are provided in the next chapter: Chapter 6.

5.1 Introduction

The linear kinetic transport equations are ubiquitous in many application areas, including as a model for neutron transport in nuclear reactors and the propagation of electromagnetic radiation in astrophysics. The main computational challenge in solving the linear transport equations is that solutions live in a high-dimensional phase space that must be sufficiently resolved for accurate simulations. The three standard computational techniques for solving the linear transport equations are the (1) implicit Monte Carlo (IMC), (2) discrete ordinate(S_N), and (3) spherical harmonic(P_N) methods. Monte Carlo (MC) methods are stochastic methods for solving time-dependent nonlinear RTEs. In the IMC methods, implicit time stepping is used. Also, in the IMC methods, the photons are considered to be re-emitted from the place where they were actually absorbed, and this helps improve the accuracy of the original MC methods. Overall, IMC method improves stability, flexibility, and computational efficiency [21].

The S_N method solves the transport equation using a quadrature rule to reconstruct the energy density. This method suffers from so-called “ray effect”, which are due to the approximation of the double integral over a unit sphere by a finite number of discrete angular directions [10].

The P_N approximation is based on the truncated spherical harmonics expansion. A

big challenge with the P_N approach is that the spherical harmonics expansion does not prevent the formation of negative particle concentrations, which is produced by the "wave effect". The idea behind our research is to develop an alternative formulation of P_N approximations that hybridizes aspects of both P_N and S_N . Although the basic scheme does not guarantee positivity of the solution, the new formulation allows for the introduction of local limiters that can be used to enforce positivity.

5.2 The Hybrid Discrete (H_N^T) Approximation: One-Dimension

The P_N approximation uses truncated spherical harmonics basis functions to approximate the linear kinetic equation. However, this produces undesirable effect which is negative particle concentration. Similarly, S_N method has the ray effect. Thus, we improve the phenomena using the discretized triangular region for the integration of the unit sphere. Instead of using spherical harmonic functions for the entire sphere, we use piecewise basis functions for each triangular region on sphere. The idea is to develop an alternative formulation of the discrete approximation that hybridizes aspects of both P_N and S_N .

5.2.1 Derivation

The linear kinetic transport equation is the equation of kinetic distribution F :

$$F_{,t} + \underline{\Omega} \cdot \nabla_r F + \sigma_t F = \frac{\sigma_s}{4\pi} \int_{\mathbb{S}^2} F(\underline{r}, \underline{\Omega}, t) d\underline{\Omega}, \quad (5.1)$$

where $\underline{r} = (x, y, z) \in \Gamma \subset \mathbb{R}^d$ is a position, $\underline{\Omega} \subset \mathbb{S}^2$ is an angle. In one-dimension, (5.1) becomes

$$F_{,t} + \mu F_{,z} + \sigma_t F = \frac{\sigma_s}{2} \rho, \quad (5.2)$$

where

$$\rho(z, t) = \int_{-1}^1 F(z, \mu, t) d\mu. \quad (5.3)$$

In P_N equations, we let

$$F(z, \mu, t) := \sum_{k=0}^N u_k(z, t) p_k(\mu), \quad (5.4)$$

with the Legendre polynomial $p_k(\mu)$, in contrast, in the H_N^T equations, we have a discretized version of (5.4):

$$F^{(j)}(z, \alpha, t) := \sum_{k=0}^N u_k^{(j)}(z, t) p_k(\alpha), \quad (5.5)$$

with μ and $\rho^{(j)}$ as

$$\mu = \mu^{(j)} + \alpha \frac{\Delta\mu}{2}, \quad (5.6)$$

and

$$\rho^{(j)}(z, t) := \int_{\mu^{(j)} - \frac{\Delta\mu}{2}}^{\mu^{(j)} + \frac{\Delta\mu}{2}} F(z, \mu, t) d\mu = \frac{\Delta\mu}{2} \int_{-1}^1 F^{(j)}(z, \alpha, t) d\alpha, \quad (5.7)$$

for $j = 1, 2, \dots, N_\mu$ with $\alpha \in [-1, 1]$.

Originally $\mu \in [-1, 1]$ in (5.4), however, $\mu \in \left[\mu_j - \frac{\Delta\mu}{2}, \mu_j + \frac{\Delta\mu}{2}\right]$ in (5.5), hence

$$F_{,t}^{(j)}(t, z, \alpha) + \left(\mu^{(j)} + \alpha \frac{\Delta\mu}{2}\right) F_{,z}^{(j)}(t, z, \alpha) + \sigma_t F^{(j)}(t, z, \alpha) = \frac{\sigma_s}{2} \sum_{j=1}^{N_\mu} \rho^{(j)}(t, z). \quad (5.8)$$

Plugging (5.5) into (5.8) and multiplying the equation by the Legendre polynomial p_ℓ , then integrating over $[-1, 1]$ give the following system of equations:

$$\underline{u}_{,t}^{(j)} + \underline{A}_{,z}^{(j)} \underline{u}_{,z}^{(j)} + \sigma_t \underline{u}^{(j)} = \underline{B} \sum_{j=1}^{N_\mu} \underline{u}^{(j)}, \quad (5.9)$$

where

$$\underline{u}^{(j)} = \begin{bmatrix} u_1^{(j)} & u_2^{(j)} & \dots & u_{N+1}^{(j)} \end{bmatrix}^T, \quad (5.10)$$

$$A_{k\ell}^{(j)} = \mu^{(j)} \delta_{k\ell} + \frac{\Delta\mu}{2} \int_{-1}^1 \alpha p_k(\alpha) p_\ell(\alpha) d\alpha, \quad (5.11)$$

and

$$B_{k\ell} = \begin{cases} \frac{\sigma_s \Delta\mu}{4}, & \text{if } k = \ell = 1, \\ 0, & \text{otherwise.} \end{cases} \quad (5.12)$$

The scattering term (right hand side) in (5.9) is not obvious, so we add more details.

By (5.7), the right hand side of (5.8) becomes

$$\frac{\sigma_s}{2} \sum_{j=1}^{N_\mu} \rho^{(j)}(t, z) = \frac{\sigma_s}{2} \sum_{j=1}^{N_\mu} \frac{\Delta\mu}{2} \int_{-1}^1 F^{(j)}(z, \alpha, t) d\alpha. \quad (5.13)$$

Plugging (5.5) into (5.13), we get

$$\frac{\sigma_s}{2} \sum_{j=1}^{N_\mu} \frac{\Delta\mu}{2} \int_{-1}^1 F^{(j)}(z, \alpha, t) d\alpha = \frac{\sigma_s}{2} \sum_{j=1}^{N_\mu} \frac{\Delta\mu}{2} \int_{-1}^1 \left(\sum_{k=0}^N u_k^{(j)}(z, t) p_k(\alpha) \right) d\alpha. \quad (5.14)$$

Multiply (5.14) by $p_\ell(\alpha)$ and integrate over $[-1, 1]$ to get

$$\frac{\sigma_s \Delta\mu}{4} \left[\sum_{j=1}^{N_\mu} \sum_{k=0}^N \left(u_k^{(j)}(z, t) \int_{-1}^1 p_k(\alpha) d\alpha \right) \right] \int_{-1}^1 p_\ell(\alpha) d\alpha. \quad (5.15)$$

Note that

$$\int_{-1}^1 p_k(\alpha) d\alpha = \delta_{k0} \quad \text{and} \quad \int_{-1}^1 p_\ell(\alpha) d\alpha = \delta_{\ell0}, \quad (5.16)$$

where δ_{k0} and $\delta_{\ell0}$ are Kronecker delta functions.

Thus, (5.15) becomes

$$\frac{\sigma_s \Delta\mu}{4} \left[\sum_{j=1}^{N_\mu} \sum_{k=0}^N \left(u_k^{(j)}(z, t) \delta_{k0} \right) \right] \delta_{\ell0}. \quad (5.17)$$

Finally, we obtain a simple hyperbolic system:

$$\underline{u}_{,t} + \underline{\underline{A}} \underline{u}_{,z} = (\underline{\underline{C}} - \sigma_t \mathbb{I}) \underline{u}, \quad (5.18)$$

where

$$\underline{\underline{A}} = \begin{bmatrix} \underline{\underline{A}}^{(1)} & & & & \\ & \underline{\underline{A}}^{(2)} & & & \\ & & \underline{\underline{A}}^{(3)} & & \\ & & & \ddots & \\ & & & & \underline{\underline{A}}^{(N_\mu)} \end{bmatrix}, \quad (5.19)$$

and

$$\underline{\underline{C}} = \begin{bmatrix} \underline{\underline{B}} & \underline{\underline{B}} & \underline{\underline{B}} & \cdots & \underline{\underline{B}} \\ \underline{\underline{B}} & \underline{\underline{B}} & \underline{\underline{B}} & \cdots & \underline{\underline{B}} \\ \underline{\underline{B}} & \underline{\underline{B}} & \underline{\underline{B}} & \cdots & \underline{\underline{B}} \\ \vdots & \vdots & \vdots & \ddots & \vdots \\ \underline{\underline{B}} & \underline{\underline{B}} & \underline{\underline{B}} & \cdots & \underline{\underline{B}} \end{bmatrix}. \quad (5.20)$$

Theorem 5.1. (5.18) is hyperbolic.

Proof. We know that $A_{k\ell}^{(j)}$ is a form of

$$A_{k\ell}^{(j)} = \mu^{(j)} \delta_{k\ell} + \frac{\Delta\mu}{2} \int_{-1}^1 \alpha p_k(\alpha) p_\ell(\alpha) d\alpha. \quad (5.21)$$

By the property of Legendre function in [4],

$$\int_{-1}^1 \alpha p_k(\alpha) p_\ell(\alpha) d\alpha = \begin{cases} \frac{2k}{(2k-1)(2k+1)}, & \text{if } \ell = k-1, \\ \frac{2(k+1)}{(2k+1)(2k+3)}, & \text{if } \ell = k+1. \end{cases}. \quad (5.22)$$

Thus,

$$A_{k\ell}^{(j)} = \begin{cases} \frac{k\Delta\mu}{(2k-1)(2k+1)}, & \text{if } \ell = k-1, \\ \mu^j, & \text{if } \ell = k, \\ \frac{(k+1)\Delta\mu}{(2k+1)(2k+3)}, & \text{if } \ell = k+1, \\ 0, & \text{otherwise,} \end{cases} \quad (5.23)$$

i.e., $\underline{\underline{A}}^{(j)}$ is a tri-diagonal matrix. Note that $\underline{\underline{A}}^{(j)}$ is symmetric, since

$$A_{k,k-1}^{(j)} = \frac{k\Delta\mu}{(2k-1)(2k+1)} = A_{k-1,k}^{(j)}.$$

Since $\underline{\underline{A}}^{(j)}$ is a block matrix as in (5.19), $\underline{\underline{A}}$ is a tridiagonal and symmetric matrix, thus, (5.18) is hyperbolic. \square

5.2.2 Discontinuous Galerkin (DG) Method

Consider the equation (5.18). Define $u_k^{(j)}(z, t)$ as

$$u_k^{(j)}(z, t) \Big|_{z \in [z_i - \frac{\Delta z}{2}, z_i + \frac{\Delta z}{2}]} := \sum_{\ell=1}^M Q_i^{(j)k\ell}(t) \psi^\ell(\xi), \quad (5.24)$$

and let

$$\underline{Q}_i^{k\ell}(t) = \left[Q_i^{(1)k\ell} \ Q_i^{(2)k\ell} \ \dots \ Q_i^{(N_\mu)k\ell} \right]^T. \quad (5.25)$$

Plug this into (5.18), to get

$$\dot{Q}_i^{k\ell}(t) = - \left[\left(\underline{\underline{\Lambda}}^+ \sum_{\hat{\ell}=1}^M \underline{Q}_i^{k\hat{\ell}}(t) \psi^{\hat{\ell}}(1) + \underline{\underline{\Lambda}}^- \sum_{\hat{\ell}=1}^M \underline{Q}_{i+1}^{k\hat{\ell}}(t) \psi^{\hat{\ell}}(-1) \right) \psi^\ell(1) \right]$$

$$\begin{aligned}
& - \left[\underline{\Lambda}^+ \sum_{\hat{\ell}=1}^M \underline{Q}_{i-1}^{k\hat{\ell}}(t) \psi^{\hat{\ell}}(1) + \underline{\Lambda}^- \sum_{\hat{\ell}=1}^M \underline{Q}_i^{k\hat{\ell}}(t) \psi^{\hat{\ell}}(-1) \right] \psi^\ell(-1) \\
& + \underline{\Lambda} \sum_{\hat{\ell}=1}^M \underline{Q}_i^{k\hat{\ell}}(t) \int_{-1}^1 \psi^{\hat{\ell}}(\xi) \psi_{,\xi}^\ell(\xi) d\xi \\
& - \underline{B} \left[\sum_{\hat{\ell}=1}^M \underline{Q}_i^{k\hat{\ell}}(t) \psi^{\hat{\ell}}(1) \psi^\ell(1) - \sum_{\hat{\ell}=1}^M \underline{Q}_{i-1}^{k\hat{\ell}}(t) \psi^{\hat{\ell}}(1) \psi^\ell(-1) \right] \\
& + \underline{B} \sum_{\hat{\ell}=1}^M \underline{Q}_i^{k\hat{\ell}}(t) \int_{-1}^1 \psi^{\hat{\ell}}(\xi) \psi_{,\xi}^\ell(\xi) d\xi - \sigma \underline{Q}_i^{k\ell}(t) \\
& + \frac{\sigma \Delta \mu}{4} \left[1 \ 1 \ 1 \cdots \ 1 \right]^T \int_{-1}^1 p^k(\alpha) d\alpha \sum_{j=1}^{N_\mu} \sum_{\hat{k}=1}^{N+1} Q_{ij}^{\hat{k}\ell}(t) \int_{-1}^1 p^{\hat{k}}(\alpha) d\alpha.
\end{aligned}$$

By defining the operator L as follow

$$\begin{aligned}
L(Q) = & - \left[\left(\underline{\Lambda}^+ \sum_{\hat{\ell}=1}^M \underline{Q}_i^{k\hat{\ell}} \psi^{\hat{\ell}}(1) + \underline{\Lambda}^- \sum_{\hat{\ell}=1}^M \underline{Q}_{i+1}^{k\hat{\ell}} \psi^{\hat{\ell}}(-1) \right) \psi^\ell(1) \right. \\
& - \left. \left(\underline{\Lambda}^+ \sum_{\hat{\ell}=1}^M \underline{Q}_{i-1}^{k\hat{\ell}} \psi^{\hat{\ell}}(1) + \underline{\Lambda}^- \sum_{\hat{\ell}=1}^M \underline{Q}_i^{k\hat{\ell}} \psi^{\hat{\ell}}(-1) \right) \psi^\ell(-1) \right] \\
& + \underline{\Lambda} \sum_{\hat{\ell}=1}^M \underline{Q}_i^{k\hat{\ell}} \int_{-1}^1 \psi^{\hat{\ell}}(\xi) \psi_{,\xi}^\ell(\xi) d\xi \\
& - \underline{B} \left[\sum_{\hat{\ell}=1}^M \underline{Q}_i^{k\hat{\ell}} \psi^{\hat{\ell}}(1) \psi^\ell(1) - \sum_{\hat{\ell}=1}^M \underline{Q}_{i-1}^{k\hat{\ell}} \psi^{\hat{\ell}}(1) \psi^\ell(-1) \right] \\
& + \underline{B} \sum_{\hat{\ell}=1}^M \underline{Q}_i^{k\hat{\ell}} \int_{-1}^1 \psi^{\hat{\ell}}(\xi) \psi_{,\xi}^\ell(\xi) d\xi - \sigma \underline{Q}_i^{k\ell} \\
& + \frac{\sigma \Delta \mu}{4} \left[1 \ 1 \ \dots \ 1 \right]^T \int_{-1}^1 p^k(\alpha) d\alpha \sum_{j=1}^{N_\mu} \sum_{\hat{k}=1}^{N+1} Q_{ij}^{\hat{k}\ell} \int_{-1}^1 p^{\hat{k}}(\alpha) d\alpha,
\end{aligned} \tag{5.26}$$

we can apply explicit Runge-Kutta time stepping methods.

5.2.3 SSP-RK

We use the low-storage strong stability-preserving Runge-Kutta method by Ketcheson [35] for our numerical implementation. The algorithm for the time discretization is shown in Table 5.1.

Table 5.1: Algorithm for low-storage strong stability-preserving Runge-Kutta (ten-stage fourth-order).

$Q^{(1)} = Q^n;$ $Q^{(2)} = Q^n;$ $\text{for } i = 1 : 5 \text{ do}$ $Q^{(1)} = Q^{(1)} + \frac{\Delta t}{6} L(Q^{(1)});$ end $Q^{(2)} = \frac{1}{25} Q^{(2)} + \frac{9}{25} Q^{(1)};$ $Q^{(1)} = 15Q^{(2)} - 5Q^{(1)};$ $\text{for } i = 6 : 9 \text{ do}$ $Q^{(1)} = Q^{(1)} + \frac{\Delta t}{6} L(Q^{(1)});$ end $Q^{(n+1)} = Q^{(2)} + \frac{3}{5} Q^{(1)} + \frac{\Delta t}{10} L(Q^{(1)});$
--

5.2.4 Positivity-preserving limiters

We are going to build the positive-preserving limiters based on the work in [62]. The Zhang-Shu limiter preserves the positivity of the solutions for the finite volume schemes or discontinuous Galerkin (DG) schemes with strong stability preserving (SSP) high order time discretization.

Define $F_i^{(j)}$ as follow:

$$F_i^{(j)}(\xi, \alpha, t) := \sum_{\ell=1}^M \sum_{k=1}^{N+1} Q_i^{(j)k\ell}(t) \phi^\ell(\xi) p^k(\alpha). \quad (5.27)$$

We can rewrite (5.27) as

$$\begin{aligned} F_i^{(j)}(\xi, \alpha, t) &= \frac{1}{2} Q_i^{(j)11} + \left(\frac{1}{\sqrt{2}} \sum_{\ell=2}^M Q_i^{(j)1\ell}(t) \phi^\ell(\xi) + \frac{1}{\sqrt{2}} \sum_{k=2}^{N+1} Q_i^{(j)k1}(t) p^k(\alpha) \right. \\ &\quad \left. + \sum_{\ell=2}^M \sum_{k=2}^{N+1} Q_i^{(j)k\ell}(t) \phi^\ell(\xi) p^k(\alpha) \right), \end{aligned} \quad (5.28)$$

and then update $F_i^{(j)}$ using the limiter $\theta_i^{(j)}$:

$$F_i^{(j)}(\xi, \alpha, t) \leftarrow \frac{1}{2} Q_i^{(j)11} + \theta_i^{(j)} \left(\bar{F}_i^{(j)} - \frac{1}{2} Q_i^{(j)11} \right), \quad (5.29)$$

where

$$\theta_i^{(j)} = \min \left(\frac{\varepsilon - Q_i^{(j)11}}{F_{\min} - Q_i^{(j)11}}, 1 \right), \quad (5.30)$$

with

$$F_{\min} := \min_{(\xi, \alpha) \in S} \bar{F}_i^{(j)}(t, \xi, \alpha), \quad \xi, \alpha \in [-1, 1], \quad S = S_1 \otimes S_2,$$

$$S_1 := \text{set of M+1 Gauss-Lobatto quadrature points}, \quad (5.31)$$

$$S_2 := \text{set of N+1 Gauss-Legendre quadrature points, and}$$

$$\epsilon := 1.0 \times 10^{-13}.$$

Finally, update $Q_i^{(j)k\ell}$ as

$$Q_i^{(j)k\ell} \leftarrow \theta_i^{(j)} Q_i^{(j)k\ell}, \quad \theta_i^{(j)} = 1 \text{ if } k = \ell = 1. \quad (5.32)$$

We will show the numerical results for the positivity-preserving limiters in the later section.

5.3 Two-Dimensional Piecewise-P_N equations

In this section, we show two different versions of piecewise-P_N approximations. We try to use the original spherical harmonics and modify it to solve the linear kinetic transport equation. However, these methods are computationally inefficient and we could not find how to reduce the number of equations yet. Therefore, readers might be better to skip this section. We just leave this section for later research.

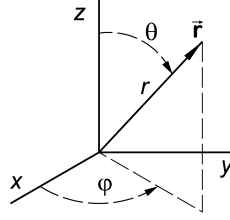
5.3.1 Version I: Fragments

The original equation is as follow:

$$F_{,t}(x, y, \Omega, t) + \Omega \cdot \nabla F(x, y, \Omega, t) + \sigma_t F(x, y, \Omega, t) = \int_{\mathbf{S}^2} \frac{\sigma_s}{4\pi} F(x, y, \Omega', t) d\Omega'. \quad (5.33)$$

Let

$$F(x, y, \Omega, t) := \sum_{\ell=0}^N \sum_{m=-\ell}^{\ell} F_{\ell}^m(x, y, t) Y_{\ell}^m(\Omega), \quad (5.34)$$

Figure 5.1: The polar angle θ and azimuthal angle ϕ .

where

$$Y_\ell^m(\mu, \phi) = \sqrt{\frac{(2\ell+1)(\ell-m)!}{4\pi(\ell+m)!}} p_\ell^m(\mu) e^{im\phi}, \quad (5.35)$$

with $\mu = \cos \theta$.

If we discretize μ and ϕ as

$$\mu = \mu_p + \alpha \frac{\Delta\mu}{2}, \quad \phi = \phi_q + \beta \frac{\Delta\phi}{2\pi}, \quad (5.36)$$

then

$$Y_\ell^m(\alpha, \beta) = \sqrt{\frac{(2\ell+1)(\ell-m)!}{4\pi(\ell+m)!}} p_\ell^m(\alpha) e^{im(\phi_q + \beta \frac{\Delta\phi}{2\pi})}, \quad (5.37)$$

and

$$p = 1, 2, 3, \dots, N_\mu, \quad q = 1, 2, 3, \dots, N_\phi, \quad (5.38)$$

$$\mu = \mu_p + \alpha \frac{\Delta\mu}{2}, \quad \phi = \phi_q + \beta \frac{\Delta\phi}{2\pi},$$

$$\alpha \in [-1, 1], \quad \beta \in [-\pi, \pi]. \quad (5.39)$$

$$\mu \in [\cos \theta, 1], \quad \phi \in [0, 2\pi],$$

$$\alpha \in [-1, 1], \quad \beta \in [-\pi, \pi].$$

Then the equation becomes

$$\begin{aligned} & F_{,t}^{(p,q)} + \sqrt{1 - \left(\mu_p + \alpha \frac{\Delta\mu}{2}\right)^2} \cos\left(\phi_q + \beta \frac{\Delta\phi}{2\pi}\right) F_{,x}^{(p,q)} \\ & + \sqrt{1 - \left(\mu_p + \alpha \frac{\Delta\mu}{2}\right)^2} \sin\left(\phi_q + \beta \frac{\Delta\phi}{2\pi}\right) F_{,y}^{(p,q)} + \sigma_t F^{(p,q)} \\ & = \frac{\sigma_s \Delta\mu \Delta\phi}{(4\pi)^2} \sum_{p=1}^{N_\mu} \sum_{q=1}^{N_\phi} \int_{-1}^1 \int_{-\pi}^{\pi} \sum_{\ell=0}^{\ell} \sum_{m=-\ell}^{\ell} F_\ell^{m(p,q)} Y_\ell^m(\alpha, \beta) d\alpha d\beta. \end{aligned} \quad (5.40)$$

Now multiply (5.40) by the conjugate of the spherical harmonic basis function, $\bar{Y}_{\ell'}^{m'}$, and then integrate of both sides over the rectangle $[-1, 1] \times [-\pi, \pi]$ to get

$$\begin{aligned}
& \int_{-1}^1 \int_{-\pi}^{\pi} \sum_{\ell=0}^N \sum_{m=-\ell}^{\ell} F_{\ell,t}^{m(p,q)}(x, y, t) Y_{\ell}^m \bar{Y}_{\ell'}^{m'} d\alpha d\beta \\
& + \int_{-1}^1 \int_{-\pi}^{\pi} \sqrt{1 - \left(\mu_p + \alpha \frac{\Delta\mu}{2}\right)^2} \cos\left(\phi_q + \beta \frac{\Delta\phi}{2\pi}\right) \sum_{\ell=0}^N \sum_{m=-\ell}^{\ell} F_{\ell,x}^{m(p,q)} Y_{\ell}^m \bar{Y}_{\ell'}^{m'} d\alpha d\beta \\
& + \int_{-1}^1 \int_{-\pi}^{\pi} \sqrt{1 - \left(\mu_p + \alpha \frac{\Delta\mu}{2}\right)^2} \sin\left(\phi_q + \beta \frac{\Delta\phi}{2\pi}\right) \sum_{\ell=0}^N \sum_{m=-\ell}^{\ell} F_{\ell,y}^{m(p,q)} Y_{\ell}^m \bar{Y}_{\ell'}^{m'} d\alpha d\beta \quad (5.41) \\
& + \sigma_t \sum_{\ell=0}^N \sum_{m=-\ell}^{\ell} F_{\ell}^{m(p,q)} \int_{-1}^1 \int_{-\pi}^{\pi} Y_{\ell}^m \bar{Y}_{\ell'}^{m'} d\alpha d\beta \\
& = \frac{\sigma_s \Delta\mu \Delta\phi}{4\pi} \sum_{p=1}^{N_\mu} \sum_{q=1}^{N_\phi} F_0^{0(p,q)} \delta_{\ell'0} \delta_{m'0}.
\end{aligned}$$

This equation is equivalent to

$$\begin{aligned}
& F_{\ell,t}^{m(p,q)}(x, y, t) \delta_{\ell\ell'} \delta_{mm'} \\
& + \sum_{\ell=0}^N \sum_{m=-\ell}^{\ell} A_{\ell}^m A_{\ell'}^{m'} F_{\ell,x}^{m(p,q)} \int_{-1}^1 \sqrt{1 - \left(\mu_p + \alpha \frac{\Delta\mu}{2}\right)^2} p_{\ell}^m(\alpha) \bar{p}_{\ell'}^{m'}(\alpha) d\alpha \int_{-\pi}^{\pi} \cos\left(\phi_q + \beta \frac{\Delta\phi}{2\pi}\right) e^{i\beta(m-m')} d\beta \\
& + \sum_{\ell=0}^N \sum_{m=-\ell}^{\ell} A_{\ell}^m A_{\ell'}^{m'} F_{\ell,x}^{m(p,q)} \int_{-1}^1 \sqrt{1 - \left(\mu_p + \alpha \frac{\Delta\mu}{2}\right)^2} p_{\ell}^m(\alpha) \bar{p}_{\ell'}^{m'}(\alpha) d\alpha \int_{-\pi}^{\pi} \sin\left(\phi_q + \beta \frac{\Delta\phi}{2\pi}\right) e^{i\beta(m-m')} d\beta \\
& + \sigma_t F_{\ell}^{m(p,q)}(x, y, t) \delta_{\ell\ell'} \delta_{mm'} \\
& = \frac{\sigma_s \Delta\mu \Delta\phi}{4\pi} \sum_{p=1}^{N_\mu} \sum_{q=1}^{N_\phi} F_0^{0(p,q)} \delta_{\ell'0} \delta_{m'0}, \quad (5.42)
\end{aligned}$$

where

$$Y_{\ell}^{m(p,q)}(\alpha, \beta) = A_{\ell}^m p_{\ell}^m(\alpha) e^{im\beta}, \quad A_{\ell}^m = \sqrt{\frac{(2\ell+1)(\ell-m)!}{4\pi(\ell+m)!}},$$

and

$$p_{\ell}^m(\alpha) = \frac{(1-\alpha^2)^{m/2}}{2^{\ell} \ell!} \frac{d^{\ell+m}}{d\mu^{\ell+m}} (\alpha^2 - 1)^{\ell}.$$

5.3.2 Version II: Strips

Instead of letting

$$Y_\ell^m(\alpha, \beta) = A_\ell^m p_\ell^m(\alpha) e^{im(\phi_q + \beta \frac{\Delta\phi}{2\pi})},$$

set

$$Y_\ell^{m,p}(\alpha, \phi) = A_\ell^m p_\ell^m(\alpha) e^{im\phi}.$$

Then,

$$F(x, y, \Omega, t)|_p = \sum_{\ell=0}^N \sum_{m=-\ell}^{\ell} F_\ell^{m,p}(x, y, t) Y_\ell^{m,p}(\Omega).$$

Thus, (5.33) becomes

$$\begin{aligned} & \sum_{\ell=0}^N \sum_{m=-\ell}^{\ell} F_{\ell,t}^{m,p}(x, y, t) Y_\ell^{m,p} \\ & + \sqrt{1 - \left(\mu_p + \alpha \frac{\Delta\mu}{2} \right)^2} \cos \phi \sum_{\ell=0}^N \sum_{m=-\ell}^{\ell} F_{\ell,x}^{m,p}(x, y, t) Y_\ell^{m,p} \\ & + \sqrt{1 - \left(\mu_p + \alpha \frac{\Delta\mu}{2} \right)^2} \sin \phi \sum_{\ell=0}^N \sum_{m=-\ell}^{\ell} F_{\ell,y}^{m,p}(x, y, t) Y_\ell^{m,p} \\ & + \sigma_t \sum_{\ell=0}^N \sum_{m=-\ell}^{\ell} F_\ell^{m,p}(x, y, t) Y_\ell^{m,p} \\ & = \frac{\sigma_s \Delta\mu}{8\pi} \sum_{p=1}^{N_\mu} \sum_{\ell=0}^N \sum_{m=-\ell}^{\ell} A_\ell^m F_\ell^{m,p}(x, y, t) \int_{-1}^1 p_\ell^m(\alpha) d\alpha \int_0^{2\pi} e^{im\phi} d\phi. \end{aligned} \quad (5.43)$$

The right hand side of (5.43), can be rewritten as

$$\frac{\sigma_s \Delta\mu}{8\pi} \sum_{p=1}^{N_\mu} \sum_{\ell=0}^N \sum_{m=-\ell}^{\ell} A_\ell^m F_\ell^{m,p}(x, y, t) \int_{-1}^1 p_\ell^m(\alpha) d\alpha \cdot 2\pi \delta_{m0} = \frac{\sigma_s \Delta\mu}{2} \sum_{p=1}^{N_\mu} A_\ell^m F_\ell^{m,p} \delta_{\ell0} \delta_{m0}, \quad (5.44)$$

since $p_\ell^m(\alpha)$ is the Legendre polynomial when $m = 0$, i.e., $\int_{-1}^1 p_\ell^0(\alpha) d\alpha = 0$, if $\ell \neq 0$ and $\int_{-1}^1 p_\ell^0(\alpha) d\alpha = 2$, if $\ell = 0$. Hence, we get,

$$\begin{aligned} & \sum_{\ell=0}^N \sum_{m=-\ell}^{\ell} F_{\ell,t}^{m,p}(x,y,t) Y_{\ell}^{m,p} \\ & + \sqrt{1 - \left(\mu_p + \alpha \frac{\Delta\mu}{2} \right)^2} \cos \phi \sum_{\ell=0}^N \sum_{m=-\ell}^{\ell} F_{\ell,x}^{m,p}(x,y,t) Y_{\ell}^{m,p} \\ & + \sqrt{1 - \left(\mu_p + \alpha \frac{\Delta\mu}{2} \right)^2} \sin \phi \sum_{\ell=0}^N \sum_{m=-\ell}^{\ell} F_{\ell,y}^{m,p}(x,y,t) Y_{\ell}^{m,p} \\ & + \sigma_t \sum_{\ell=0}^N \sum_{m=-\ell}^{\ell} F_{\ell}^{m,p}(x,y,t) Y_{\ell}^{m,p} = \frac{\sigma_s \Delta\mu}{2} \sum_{p=1}^{N_\mu} A_\ell^m F_\ell^{m,p} \delta_{\ell 0} \delta_{m 0}. \end{aligned} \quad (5.45)$$

Multiply (5.45) by $\bar{Y}_{\ell'}^{m',p'}$ and then integrate it over the strip $[\mu_p - \frac{\Delta\mu}{2}, \mu_p + \frac{\Delta\mu}{2}] \times [0, 2\pi]$,

$$\begin{aligned} & \int_{-1}^1 \int_0^{2\pi} \sum_{\ell=0}^N \sum_{m=-\ell}^{\ell} F_{\ell,t}^{m,p}(x,y,t) Y_{\ell}^{m,p} \bar{Y}_{\ell'}^{m',p'} d\alpha d\phi \\ & + \int_{-1}^1 \int_0^{2\pi} \sqrt{1 - \left(\mu_p + \alpha \frac{\Delta\mu}{2} \right)^2} \cos \phi \sum_{\ell=0}^N \sum_{m=-\ell}^{\ell} F_{\ell,x}^{m,p}(x,y,t) Y_{\ell}^{m,p} \bar{Y}_{\ell'}^{m',p'} d\alpha d\phi \\ & + \int_{-1}^1 \int_0^{2\pi} \sqrt{1 - \left(\mu_p + \alpha \frac{\Delta\mu}{2} \right)^2} \sin \phi \sum_{\ell=0}^N \sum_{m=-\ell}^{\ell} F_{\ell,y}^{m,p}(x,y,t) Y_{\ell}^{m,p} \bar{Y}_{\ell'}^{m',p'} d\alpha d\phi \\ & + \sigma_t \sum_{\ell=0}^N \sum_{m=-\ell}^{\ell} F_{\ell}^{m,p}(x,y,t) \int_{-1}^1 \int_0^{2\pi} Y_{\ell}^{m,p} \bar{Y}_{\ell'}^{m',p'} d\alpha d\phi \\ & = \frac{\sigma_s \Delta\mu}{2} \sum_{p=1}^{N_\mu} A_\ell^m F_\ell^{m,p} \delta_{\ell 0} \delta_{m 0} \int_{-1}^1 \int_0^{2\pi} \bar{Y}_{\ell'}^{m',p'} d\alpha d\phi. \end{aligned} \quad (5.46)$$

In the first and the fourth terms of (5.46),

$$\begin{aligned} & \int_{-1}^1 \int_0^{2\pi} Y_{\ell}^{m,p} \bar{Y}_{\ell'}^{m',p'} d\alpha d\phi \\ & = A_\ell^m A_{\ell'}^{m'} \int_{-1}^1 p_\ell^m(\alpha) \bar{p}_{\ell'}^{m'}(\alpha) d\alpha \int_0^{2\pi} e^{i(m-m')\phi} d\phi \\ & = A_\ell^m A_{\ell'}^{m'} \int_{-1}^1 p_\ell^m(\alpha) \bar{p}_{\ell'}^{m'}(\alpha) d\alpha \cdot 2\pi \delta_{mm'} \\ & = 2\pi \delta_{mm'} \delta_{\ell\ell'} A_\ell^m A_{\ell'}^{m'} \frac{2(\ell' + m')!}{(2\ell' + 1)(\ell' - m')!} \\ & = 4\pi \delta_{mm'} \delta_{\ell\ell'} A_\ell^m A_{\ell'}^{m'} \frac{(\ell' + m')!}{(2\ell' + 1)(\ell' - m')!}. \end{aligned} \quad (5.47)$$

And in the last term of (5.46),

$$\begin{aligned}
& \int_{-1}^1 \int_0^{2\pi} \bar{Y}_{\ell'}^{m', p'} d\alpha d\phi \\
&= A_{\ell'}^{m'} \int_{-1}^1 \bar{p}_{\ell'}^{m'}(\alpha) d\alpha \int_0^{2\pi} e^{-im'\phi} d\phi \\
&= 4\pi A_{\ell'}^{m'} \delta_{\ell'0} \delta_{m'0}.
\end{aligned} \tag{5.48}$$

Now equation (5.46) is equivalent to

$$\begin{aligned}
& 4\pi \sum_{\ell=0}^N \sum_{m=-\ell}^{\ell} \delta_{mm'} \delta_{\ell\ell'} A_{\ell}^m A_{\ell'}^{m'} \frac{(\ell'+m')!}{(2\ell'+1)(\ell'-m')!} F_{\ell,t}^{m,p}(x, y, t) \\
&+ \sum_{\ell=0}^N \sum_{m=-\ell}^{\ell} A_{\ell}^m A_{\ell'}^{m'} F_{\ell,x}^{m,p}(x, y, t) \int_{-1}^1 \sqrt{1 - \left(\mu_p + \alpha \frac{\Delta\mu}{2}\right)^2} p_{\ell}^m(\alpha) \bar{p}_{\ell'}^{m'}(\alpha) d\alpha \int_0^{2\pi} \cos \phi e^{i(m-m')\phi} d\phi \\
&+ \sum_{\ell=0}^N \sum_{m=-\ell}^{\ell} A_{\ell}^m A_{\ell'}^{m'} F_{\ell,y}^{m,p}(x, y, t) \int_{-1}^1 \sqrt{1 - \left(\mu_p + \alpha \frac{\Delta\mu}{2}\right)^2} p_{\ell}^m(\alpha) \bar{p}_{\ell'}^{m'}(\alpha) d\alpha \int_0^{2\pi} \sin \phi e^{i(m-m')\phi} d\phi \\
&+ 4\pi \sigma_t \sum_{\ell=0}^N \sum_{m=-\ell}^{\ell} F_{\ell}^{m,p}(x, y, t) \delta_{mm'} \delta_{\ell\ell'} A_{\ell}^m A_{\ell'}^{m'} \frac{(\ell'+m')!}{(2\ell'+1)(\ell'-m')!} = 4\pi \sigma_s A_{\ell'}^{m'} \delta_{\ell'0} \delta_{m'0}.
\end{aligned} \tag{5.49}$$

In (5.49),

$$\int_0^{2\pi} \cos \phi e^{i(m-m')\phi} d\phi = \pi \delta_{m,m'\pm 1}, \tag{5.50}$$

and

$$\int_0^{2\pi} \sin \phi e^{i(m-m')\phi} d\phi = \pm i\pi \delta_{m,m'\pm 1}. \tag{5.51}$$

Rewriting (5.49),

$$\begin{aligned}
& 4\pi(A_{\ell'}^{m'})^2 \frac{(\ell' + m')!}{(2\ell' + 1)(\ell' - m')!} F_{\ell',t}^{m',p'}(x, y, t) \\
& + \pi \sum_{\ell=0}^N A_\ell^{m'+1} A_{\ell'}^{m'} F_{\ell,x}^{m'+1,p}(x, y, t) \int_{-1}^1 \sqrt{1 - \left(\mu_p + \alpha \frac{\Delta\mu}{2}\right)^2} p_\ell^{m'+1}(\alpha) \bar{p}_{\ell'}^{m'}(\alpha) d\alpha \\
& + \pi \sum_{\ell=0}^N A_\ell^{m'-1} A_{\ell'}^{m'} F_{\ell,x}^{m'-1,p}(x, y, t) \int_{-1}^1 \sqrt{1 - \left(\mu_p + \alpha \frac{\Delta\mu}{2}\right)^2} p_\ell^{m'-1}(\alpha) \bar{p}_{\ell'}^{m'}(\alpha) d\alpha \\
& + i\pi \sum_{\ell=0}^N A_\ell^{m'+1} A_{\ell'}^{m'} F_{\ell,y}^{m'+1,p}(x, y, t) \int_{-1}^1 \sqrt{1 - \left(\mu_p + \alpha \frac{\Delta\mu}{2}\right)^2} p_\ell^{m'+1}(\alpha) \bar{p}_{\ell'}^{m'}(\alpha) d\alpha \\
& - i\pi \sum_{\ell=0}^N A_\ell^{m'-1} A_{\ell'}^{m'} F_{\ell,y}^{m'-1,p}(x, y, t) \int_{-1}^1 \sqrt{1 - \left(\mu_p + \alpha \frac{\Delta\mu}{2}\right)^2} p_\ell^{m'-1}(\alpha) \bar{p}_{\ell'}^{m'}(\alpha) d\alpha \\
& + 4\pi\sigma_t(A_{\ell'}^{m'})^2 \frac{(\ell' + m')!}{(2\ell' + 1)(\ell' - m')!} F_{\ell'}^{m',p'}(x, y, t) = 4\pi\sigma_s A_{\ell'}^{m'} \delta_{\ell'0} \delta_{m'0}.
\end{aligned} \tag{5.52}$$

Dividing (5.52) by π , we get,

$$\begin{aligned}
& 4(A_{\ell'}^{m'})^2 \frac{(\ell' + m')!}{(2\ell' + 1)(\ell' - m')!} F_{\ell',t}^{m',p'}(x, y, t) \\
& + \sum_{\ell=0}^N A_\ell^{m'+1} A_{\ell'}^{m'} F_{\ell,x}^{m'+1,p}(x, y, t) \int_{-1}^1 \sqrt{1 - \left(\mu_p + \alpha \frac{\Delta\mu}{2}\right)^2} p_\ell^{m'+1}(\alpha) \bar{p}_{\ell'}^{m'}(\alpha) d\alpha \\
& + \sum_{\ell=0}^N A_\ell^{m'-1} A_{\ell'}^{m'} F_{\ell,x}^{m'-1,p}(x, y, t) \int_{-1}^1 \sqrt{1 - \left(\mu_p + \alpha \frac{\Delta\mu}{2}\right)^2} p_\ell^{m'-1}(\alpha) \bar{p}_{\ell'}^{m'}(\alpha) d\alpha \\
& + i \sum_{\ell=0}^N A_\ell^{m'+1} A_{\ell'}^{m'} F_{\ell,y}^{m'+1,p}(x, y, t) \int_{-1}^1 \sqrt{1 - \left(\mu_p + \alpha \frac{\Delta\mu}{2}\right)^2} p_\ell^{m'+1}(\alpha) \bar{p}_{\ell'}^{m'}(\alpha) d\alpha \\
& - i \sum_{\ell=0}^N A_\ell^{m'-1} A_{\ell'}^{m'} F_{\ell,y}^{m'-1,p}(x, y, t) \int_{-1}^1 \sqrt{1 - \left(\mu_p + \alpha \frac{\Delta\mu}{2}\right)^2} p_\ell^{m'-1}(\alpha) \bar{p}_{\ell'}^{m'}(\alpha) d\alpha \\
& + 4\sigma_t(A_{\ell'}^{m'})^2 \frac{(\ell' + m')!}{(2\ell' + 1)(\ell' - m')!} F_{\ell'}^{m',p'}(x, y, t) = 4\pi\sigma_s A_{\ell'}^{m'} \delta_{\ell'0} \delta_{m'0},
\end{aligned} \tag{5.53}$$

for $0 \leq \ell' \leq N$ and $-\ell' \leq m' \leq \ell'$.

5.4 Hybrid Discrete (\mathbf{H}_N^T) Approximations: Multi-Dimension

The main idea of this work is to combine the P_N and S_N approximations in such a way to obtain a method with improved properties. The goal is to generalize the 1D method described in Section 5.2. We create a new orthonormal basis for each spherical

triangle and multiply the equation by the basis, then integrate the equation over an each element. We use the triangular mesh as in Figure 5.2 to integrate the integrand over unit sphere, so that we can control both the number of triangular elements of the sphere and the number of basis function for each triangle. In the numerical test, we compare the numerical solutions for two different versions of spherical-triangular mesh, i.e., 5.2 and 5.3. Since now we have discretized angular variables along each triangular region on unit sphere \mathbb{S}^2 , we may apply the limiters to improve negativity of density and also improve the ray effect of S_N approximations by increasing the number of spherical triangles and the number of basis function for each triangle. Setting the coordinates of three vertices of triangle as $\underline{x}_1 = (x_1, y_1, z_1)$, $\underline{x}_2 = (x_2, y_2, z_2)$, $\underline{x}_3 = (x_3, y_3, z_3)$, and $\underline{x} = (x, y, z)$, we get a Jacobian,

$$J(\xi, \eta) = \frac{ax(\xi, \eta) + by(\xi, \eta) + cz(\xi, \eta)}{r^3(\xi, \eta)}, \quad (5.54)$$

where $J(\xi, \eta)$ is the transformation from $(\xi, \eta) \in \mathbb{R}^2$ to points on \mathcal{T} , and $|\mathcal{T}|$ is the surface area of $\mathcal{T} \subset \mathcal{S}^2$, and

$$\underline{x}_c = \frac{1}{3}(\underline{x}_1 + \underline{x}_2 + \underline{x}_3), \quad (5.55)$$

$$\begin{aligned} a &= -y_2z_1 + y_3z_1 + y_1z_2 - y_3z_2 - y_1z_3 + y_2z_3, \\ b &= x_2z_1 - x_3z_1 - x_1z_2 + x_3z_2 + x_1z_3 - x_2z_3, \\ c &= -x_2y_1 + x_3y_1 + x_1y_2 - x_3y_2 - x_1y_3 + x_2y_3, \\ \underline{x} &= \underline{x}_c + \xi(\underline{x}_2 - \underline{x}_1) + \eta(\underline{x}_3 - \underline{x}_1). \end{aligned} \quad (5.56) \quad (5.57)$$

On the spherical spherical triangle $\mathcal{T} \subset \mathcal{S}^2$ we define a polynomial basis, $\underline{\Psi}(\xi, \eta) : \mathbb{R}^2 \mapsto \mathbb{R}^M$, with the property that

$$\frac{1}{|\mathcal{T}|} \int_{-\frac{1}{3}}^{\frac{2}{3}} \int_{-\frac{1}{3}}^{\frac{1}{3}-\eta} \underline{\Psi} \underline{\Psi}^T J(\xi, \eta) d\xi d\eta = \mathbb{I}. \quad (5.58)$$

We can derive (5.59) from (5.33) using (5.54) – (5.58):

$$F_{,t} + \frac{x(\xi, \eta)}{r(\xi, \eta)} F_{,x} + \frac{y(\xi, \eta)}{r(\xi, \eta)} F_{,y} + \frac{z(\xi, \eta)}{r(\xi, \eta)} F_{,z} + F = \sum_{\mathcal{T} \in \mathcal{S}^2} \frac{1}{|\mathcal{T}|} \int_{\mathcal{T}} F(x, y, z, \xi, \eta, t) J(\xi, \eta) d\xi d\eta. \quad (5.59)$$

Theorem 5.2. *The H_N^T system is hyperbolic.*

Proof. We assume the following ansatz for the distribution function:

$$F(x, y, z, \xi, \eta, t) = \sum_{m=1}^M F_m(x, y, z, t) \Psi_m(\xi, \eta) = \underline{\Psi}^T \underline{F}. \quad (5.60)$$

Plugging this into (5.59), multiplying by $\underline{\Psi}$, and integrating over \mathcal{T} yields the system of equations:

$$\underline{F}_{,t} + \underline{\underline{A}}(\underline{e}_1) \underline{F}_{,x} + \underline{\underline{A}}(\underline{e}_2) \underline{F}_{,y} + \underline{\underline{A}}(\underline{e}_3) \underline{F}_{,z} = \underline{B}, \quad (5.61)$$

where $\underline{e}_1 = (1, 0, 0)$, $\underline{e}_2 = (0, 1, 0)$, $\underline{e}_3 = (0, 0, 1)$,

$$\underline{\underline{A}}(\widehat{n}) = \frac{1}{|\mathcal{T}|} \int_{-\frac{1}{3}}^{\frac{2}{3}} \int_{-\frac{1}{3}}^{\frac{1}{3}-\eta} (\widehat{n} \cdot \underline{u}) \underline{\Psi} \underline{\Psi}^T J(\xi, \eta) d\xi d\eta, \quad (5.62)$$

and

$$\underline{B} = -\underline{F} + \left[\sum_{\mathcal{T} \in \mathcal{S}^2} \left(\frac{1}{|\mathcal{T}|} \int_{-\frac{1}{3}}^{\frac{2}{3}} \int_{-\frac{1}{3}}^{\frac{1}{3}-\eta} \underline{\Psi}^T J(\xi, \eta) d\xi d\eta \right) \right] \left(\frac{1}{|\mathcal{T}'|} \int_{-\frac{1}{3}}^{\frac{2}{3}} \int_{-\frac{1}{3}}^{\frac{1}{3}-\eta} \underline{\Psi} J(\xi, \eta) d\xi d\eta \right) \underline{F}, \quad (5.63)$$

where

$$\underline{u} = \begin{bmatrix} x(\xi, \eta) & y(\xi, \eta) & z(\xi, \eta) \\ r(\xi, \eta) & r(\xi, \eta) & r(\xi, \eta) \end{bmatrix}^T. \quad (5.64)$$

Note that the ij^{th} entry of $\underline{\underline{A}}(\widehat{n})$ is given by

$$A_{ij} = \frac{1}{|\mathcal{T}|} \int_{-\frac{1}{3}}^{\frac{2}{3}} \int_{-\frac{1}{3}}^{\frac{1}{3}-\eta} (\widehat{n} \cdot \underline{u}) \Psi_i \Psi_j J(\xi, \eta) d\xi d\eta, \quad (5.65)$$

and this proves the hyperbolicity of the system. \square

Consider the following equation:

$$\underline{F}_{,t} + \underline{\Omega} \cdot \nabla_r \underline{F} + \sigma_t \underline{F} = \frac{\sigma_s}{4\pi} \int_{\mathbb{S}^2} \underline{F}(r, \underline{\Omega}, t) d\underline{\Omega} + S. \quad (5.66)$$

Let the Cartesian coordinates of three vertices of k-th triangle be

$$\begin{aligned} \underline{x}_1^{(k)} &= (x_1^{(k)}, y_1^{(k)}, z_1^{(k)}), \\ \underline{x}_2^{(k)} &= (x_2^{(k)}, y_2^{(k)}, z_2^{(k)}), \\ \underline{x}_3^{(k)} &= (x_3^{(k)}, y_3^{(k)}, z_3^{(k)}). \end{aligned} \quad (5.67)$$

Also set the coordinate of a point inside a spherical triangle as

$$\underline{x}^{(k)} = \left(x^{(k)}, y^{(k)}, z^{(k)} \right), \quad (5.68)$$

and distance between the origin and the point as

$$r^{(k)} = \sqrt{\left(x^{(k)} \right)^2 + \left(y^{(k)} \right)^2 + \left(z^{(k)} \right)^2}. \quad (5.69)$$

Note that $r^{(k)} \neq 1$, since each triangle is not on the surface of a unit sphere \mathbb{S}^2 before projection onto \mathbb{S}^2 . Then we get a Jacobian,

$$J^{(k)}(\xi, \eta) = \frac{a^{(k)}x^{(k)}(\xi, \eta) + b^{(k)}y^{(k)}(\xi, \eta) + c^{(k)}z^{(k)}(\xi, \eta)}{\left(r^{(k)}(\xi, \eta) \right)^3}, \quad (5.70)$$

where $J^{(k)}(\xi, \eta)$ is the transformation from $(\xi, \eta) \in \mathbb{R}^2$ to points on \mathbb{S}^2 , and

$$\begin{aligned} a^{(k)} &= -y_2^{(k)}z_1^{(k)} + y_3^{(k)}z_1^{(k)} + y_1^{(k)}z_2^{(k)} - y_3^{(k)}z_2^{(k)} - y_1^{(k)}z_3^{(k)} + y_2^{(k)}z_3^{(k)}, \\ b^{(k)} &= x_2^{(k)}z_1^{(k)} - x_3^{(k)}z_1^{(k)} - x_1^{(k)}z_2^{(k)} + x_3^{(k)}z_2^{(k)} + x_1^{(k)}z_3^{(k)} - x_2^{(k)}z_3^{(k)}, \\ c^{(k)} &= -x_2^{(k)}y_1^{(k)} + x_3^{(k)}y_1^{(k)} + x_1^{(k)}y_2^{(k)} - x_3^{(k)}y_2^{(k)} - x_1^{(k)}y_3^{(k)} + x_2^{(k)}y_3^{(k)}. \end{aligned} \quad (5.71)$$

Now $\underline{x}^{(k)}$ can be expressed in terms of three vertices of a k-th triangle $\underline{x}_1^{(k)}, \underline{x}_2^{(k)}, \underline{x}_3^{(k)}$ and the center of the triangle $\underline{x}_c^{(k)}$:

$$\underline{x}^{(k)} = \underline{x}_c^{(k)} + \xi \left(\underline{x}_2^{(k)} - \underline{x}_1^{(k)} \right) + \eta \left(\underline{x}_3^{(k)} - \underline{x}_1^{(k)} \right), \quad (5.72)$$

where

$$\underline{x}_c^{(k)} = \frac{1}{3} \left(\underline{x}_1^{(k)} + \underline{x}_2^{(k)} + \underline{x}_3^{(k)} \right). \quad (5.73)$$

On the spherical spherical triangle $\mathcal{T}^{(k)} \subset \mathbb{S}^2$, we define a polynomial basis,

$\underline{\Psi}^{(k)}(\xi, \eta) : \mathbb{R}^2 \mapsto \mathbb{R}^M$, with the property that

$$\frac{1}{|\mathcal{T}^{(k)}|} \int_{-\frac{1}{3}}^{\frac{2}{3}} \int_{-\frac{1}{3}}^{\frac{1}{3}-\eta} \underline{\Psi}^{(k)} \underline{\Psi}^{(k)T} J^{(k)}(\xi, \eta) d\xi d\eta = \mathbb{I}, \quad (5.74)$$

where \mathbb{I} is an identity matrix. Now we can easily derive

$$\begin{aligned} F_{,t}^{(k)} &+ \frac{x^{(k)}(\xi, \eta)}{r^{(k)}(\xi, \eta)} F_{,x}^{(k)} + \frac{y^{(k)}(\xi, \eta)}{r^{(k)}(\xi, \eta)} F_{,y}^{(k)} + \frac{z^{(k)}(\xi, \eta)}{r^{(k)}(\xi, \eta)} F_{,z}^{(k)} + \sigma_t F^{(k)} \\ &= \frac{\sigma_s}{4\pi} \sum_{\mathcal{T}^{(k)} \subset \mathbb{S}^2} \frac{1}{|\mathcal{T}^{(k)}|} \int_{\mathcal{T}^{(k)}} F^{(k)}(x, y, z, \xi, \eta, t) J^{(k)}(\xi, \eta) d\xi d\eta + S^{(k)}, \end{aligned} \quad (5.75)$$

where $k = 1, 2, \dots, T$ with T is the number of spherical triangles.

From now on, we only consider two dimensional case, so that the equation (5.75) becomes:

$$\begin{aligned} & F_{,t}^{(k)} + \frac{x^{(k)}(\xi, \eta)}{r^{(k)}(\xi, \eta)} F_{,x}^{(k)} + \frac{y^{(k)}(\xi, \eta)}{r^{(k)}(\xi, \eta)} F_{,y}^{(k)} + \sigma_t F^{(k)} \\ &= \frac{\sigma_s}{4\pi} \sum_{\mathcal{T}^{(k)} \subset \mathbb{S}^2} \frac{1}{|\mathcal{T}^{(k)}|} \int_{\mathcal{T}^{(k)}} F^{(k)}(x, y, \xi, \eta, t) J^{(k)}(\xi, \eta) d\xi d\eta + S^{(k)}, \end{aligned} \quad (5.76)$$

for $k = 1, 2, \dots, T$.

Define $F^{(k)}$ as

$$F^{(k)} := \sum_{m=1}^N F^{(k)m}(x, y, t) \Psi^{(k)m}(\xi, \eta), \quad (5.77)$$

where N is the number of basis functions $\Psi^{(k)m}(\xi, \eta)$ defined on a spherical triangle for the equation (5.76). Note that if the highest order of Ψ is n , then $N = n(n+1)/2$. Plug (5.77) into (5.76), and multiply the equation by $\Psi^{(k)m'}$, then integrate over the corresponding spherical triangle to get the following equations:

$$\begin{aligned} & \frac{1}{|\mathcal{T}^{(k)}|} \int_{-\frac{1}{3}}^{\frac{2}{3}} \int_{-\frac{1}{3}}^{\frac{1}{3}-\eta} \sum_{m=1}^N F_{,t}^{(k)m}(x, y, t) \Psi^{(k)m}(\xi, \eta) \Psi^{(k)m'}(\xi, \eta) J^{(k)}(\xi, \eta) d\xi d\eta \\ &+ \frac{1}{|\mathcal{T}^{(k)}|} \int_{-\frac{1}{3}}^{\frac{2}{3}} \int_{-\frac{1}{3}}^{\frac{1}{3}-\eta} \sum_{m=1}^N \frac{x^{(k)}(\xi, \eta)}{r^{(k)}(\xi, \eta)} F_{,x}^{(k)m}(x, y, t) \Psi^{(k)m}(\xi, \eta) \Psi^{(k)m'}(\xi, \eta) J^{(k)}(\xi, \eta) d\xi d\eta \\ &+ \frac{1}{|\mathcal{T}^{(k)}|} \int_{-\frac{1}{3}}^{\frac{2}{3}} \int_{-\frac{1}{3}}^{\frac{1}{3}-\eta} \sum_{m=1}^N \frac{y^{(k)}(\xi, \eta)}{r^{(k)}(\xi, \eta)} F_{,y}^{(k)m}(x, y, t) \Psi^{(k)m}(\xi, \eta) \Psi^{(k)m'}(\xi, \eta) J^{(k)}(\xi, \eta) d\xi d\eta \\ &+ \frac{\sigma_t}{|\mathcal{T}^{(k)}|} \int_{-\frac{1}{3}}^{\frac{2}{3}} \int_{-\frac{1}{3}}^{\frac{1}{3}-\eta} \sum_{m=1}^N F^{(k)m}(x, y, t) \Psi^{(k)m}(\xi, \eta) \Psi^{(k)m'}(\xi, \eta) J^{(k)}(\xi, \eta) d\xi d\eta \\ &= \frac{\sigma_s}{4\pi} \sum_{k'=1}^T \left(\frac{1}{|\mathcal{T}^{(k')}|} \int_{-\frac{1}{3}}^{\frac{2}{3}} \int_{-\frac{1}{3}}^{\frac{1}{3}-\eta} \sum_{m=1}^N F^{(k')m} \Psi^{(k')m} J^{(k')} d\xi d\eta \right) \frac{1}{|\mathcal{T}^{(k)}|} \int_{-\frac{1}{3}}^{\frac{2}{3}} \int_{-\frac{1}{3}}^{\frac{1}{3}-\eta} \Psi^{(k)m'} J^{(k)} d\xi' d\eta' \\ &+ \frac{1}{|\mathcal{T}^{(k)}|} \int_{-\frac{1}{3}}^{\frac{2}{3}} \int_{-\frac{1}{3}}^{\frac{1}{3}-\eta} \sum_{m=1}^N S^{(k)}(x, y, t) \Psi^{(k)m}(\xi, \eta) \Psi^{(k)m'}(\xi, \eta) J^{(k)}(\xi, \eta) d\xi d\eta, \end{aligned} \quad (5.78)$$

for $k = 1, 2, \dots, T$. For better representation of the system of equations:

$$\underline{F}_{,t} + \underline{\underline{A}}(\underline{e}_1) \underline{F}_{,x} + \underline{\underline{A}}(\underline{e}_2) \underline{F}_{,y} = -\sigma_t \underline{F} + \underline{B} + \underline{S}, \quad (5.79)$$

where $\underline{e}_1 = (1, 0)$, $\underline{e}_2 = (0, 1)$, $\underline{\underline{A}}^k$ is k -th block of block diagonal matrix $\underline{\underline{A}}$,

$$\underline{\underline{A}}^{(k)}(\widehat{n}) = \frac{1}{|\mathcal{T}^{(k)}|} \int_{-\frac{1}{3}}^{\frac{2}{3}} \int_{-\frac{1}{3}}^{\frac{1}{3}-\eta} (\widehat{n} \cdot \underline{v}) \underline{\Psi}^{(k)} \underline{\Psi}^{(k)T} J^{(k)}(\xi, \eta) d\xi d\eta, \quad (5.80)$$

with

$$\underline{v} = \begin{bmatrix} x^{(k)}(\xi, \eta) \\ r^{(k)}(\xi, \eta) \end{bmatrix}^T, \quad (5.81)$$

and

$$\underline{\underline{A}} = \begin{bmatrix} \underline{\underline{A}}^{(1)} & & & & \\ & \underline{\underline{A}}^{(2)} & & & \\ & & \underline{\underline{A}}^{(3)} & & \\ & & & \ddots & \\ & & & & \underline{\underline{A}}^{(T)} \end{bmatrix}.$$

And since

$$F^{(k)}(x, y, \xi, \eta, t) = \sum_{m=1}^N F^{(k)m}(x, y, t) \Psi^{(k)m}(\xi, \eta) = \underline{\Psi}^{(k)T} \underline{F}^{(k)}, \quad (5.82)$$

we have vectors \underline{F} and $\underline{\Psi}$ as follow:

$$\underline{F} = \begin{bmatrix} \underline{F}^{(1)} \\ \underline{F}^{(2)} \\ \underline{F}^{(3)} \\ \vdots \\ \underline{F}^{(T)} \end{bmatrix}, \quad \underline{\Psi} = \begin{bmatrix} \underline{\Psi}^{(1)} \\ \underline{\Psi}^{(2)} \\ \underline{\Psi}^{(3)} \\ \vdots \\ \underline{\Psi}^{(T)} \end{bmatrix}.$$

Also, \underline{B} in the equation (5.79) is

$$\underline{B} = \frac{\sigma_s}{4\pi} \left(\sum_{k=1}^T \underline{F}^{(k)1} \right) \underline{w}, \quad (5.83)$$

where \underline{w} is a sparse vector:

$$\underline{w} = \begin{bmatrix} \underline{c} \\ \underline{c} \\ \underline{c} \\ \vdots \\ \underline{c} \end{bmatrix} \left\{ \begin{array}{l} N \times T \text{ rows,} \\ \underline{c} = \begin{bmatrix} 1 \\ 0 \\ 0 \\ \vdots \\ 0 \end{bmatrix} \end{array} \right\} \begin{array}{l} N \text{ rows} \end{array}$$

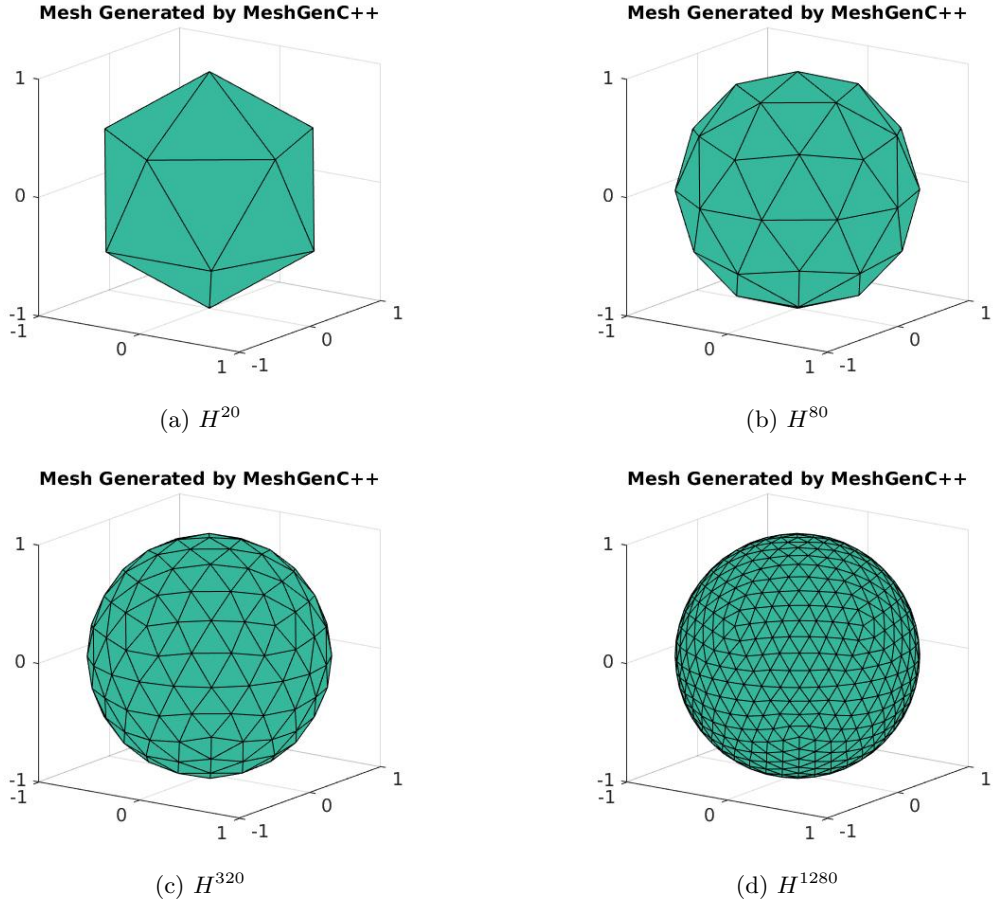


Figure 5.2: Triangular meshes for the Hybrid Discrete Method.

with T is the number of triangular elements on the unit sphere \mathbb{S}^2 , and N is the number of basis functions for each triangle.

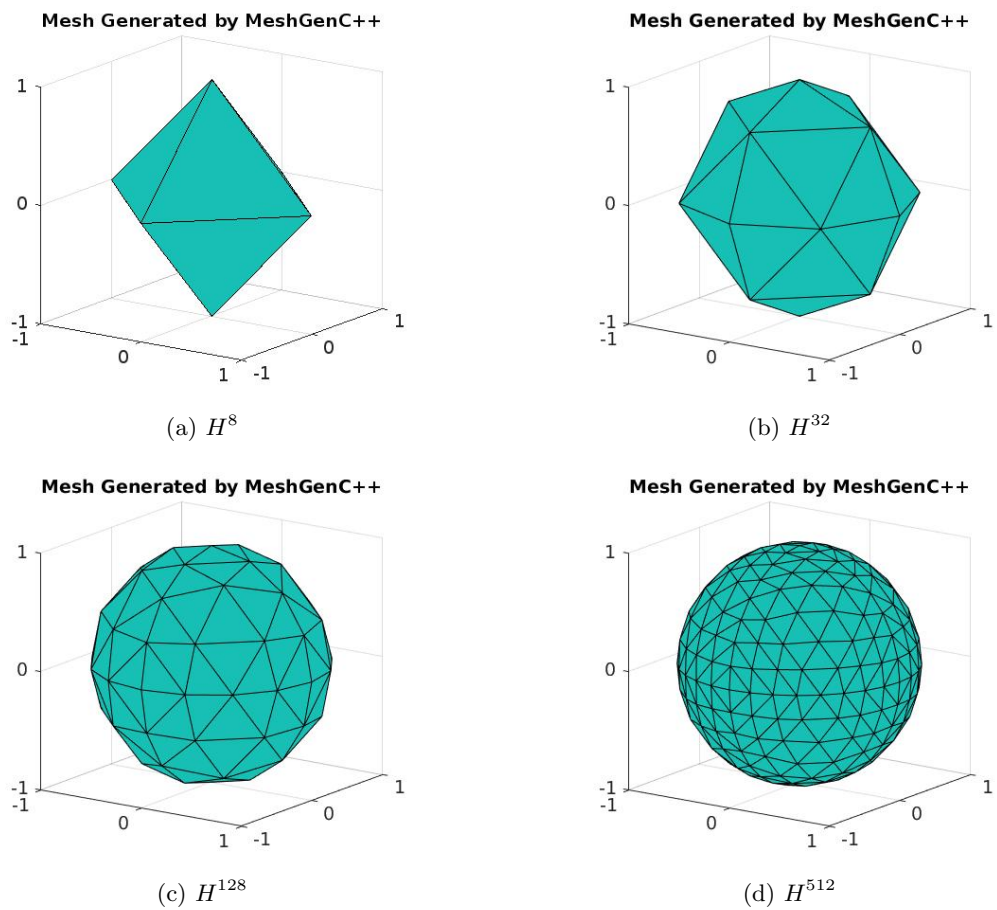


Figure 5.3: Octantal triangular meshes for the Hybrid Discrete Method.

CHAPTER 6. NUMERICAL RESULTS

In this chapter, we provide the numerical results of H_N^T approximation to the linear kinetic transport equation with plane source problem (1D), line source problem (2D), and lattice problem (2D). The comparison of P_N and H_N^T solutions is also given in order to gain insight into the properties of each method.

6.1 Numerical Results in 1D

First we test the plane source problem. The particle density is plotted for each P_N in Figure 6.1. In order to compare the results, we take the semi-analytic P_N solutions from [22]. Also, the convergence rate for each P_N solution is provided in Figure 6.2. Next we provide the comparison of P_N and H_N^T in Figure 6.3, then give the results of positive limiter in Figure 6.4. The smooth function $e^{-300(x-1)^2}$ is used as an initial condition for Figure 6.1 and the Dirac delta function is used for Figure 6.3 and 6.4.

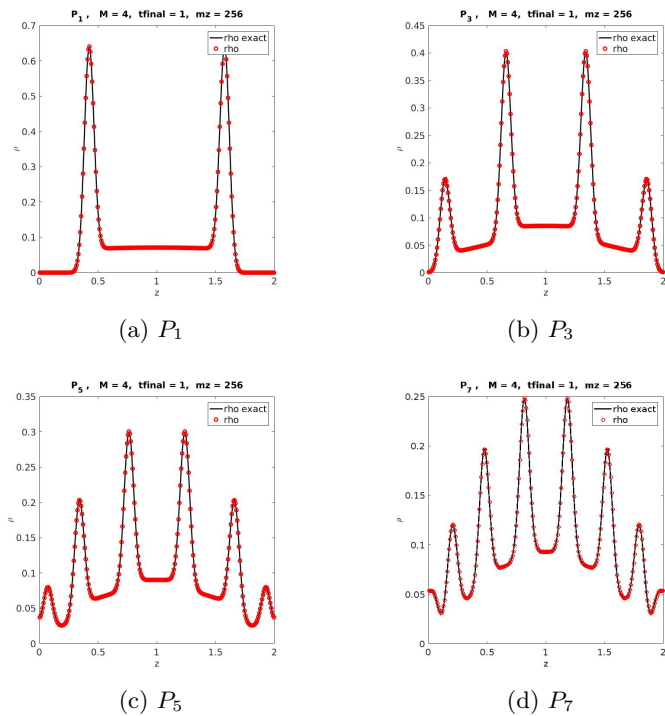


Figure 6.1: P_N solutions in 1D. Here each P_N solutions are compared to the exact P_N solutions. This is the numerical accuracy test for our numerical schemes.

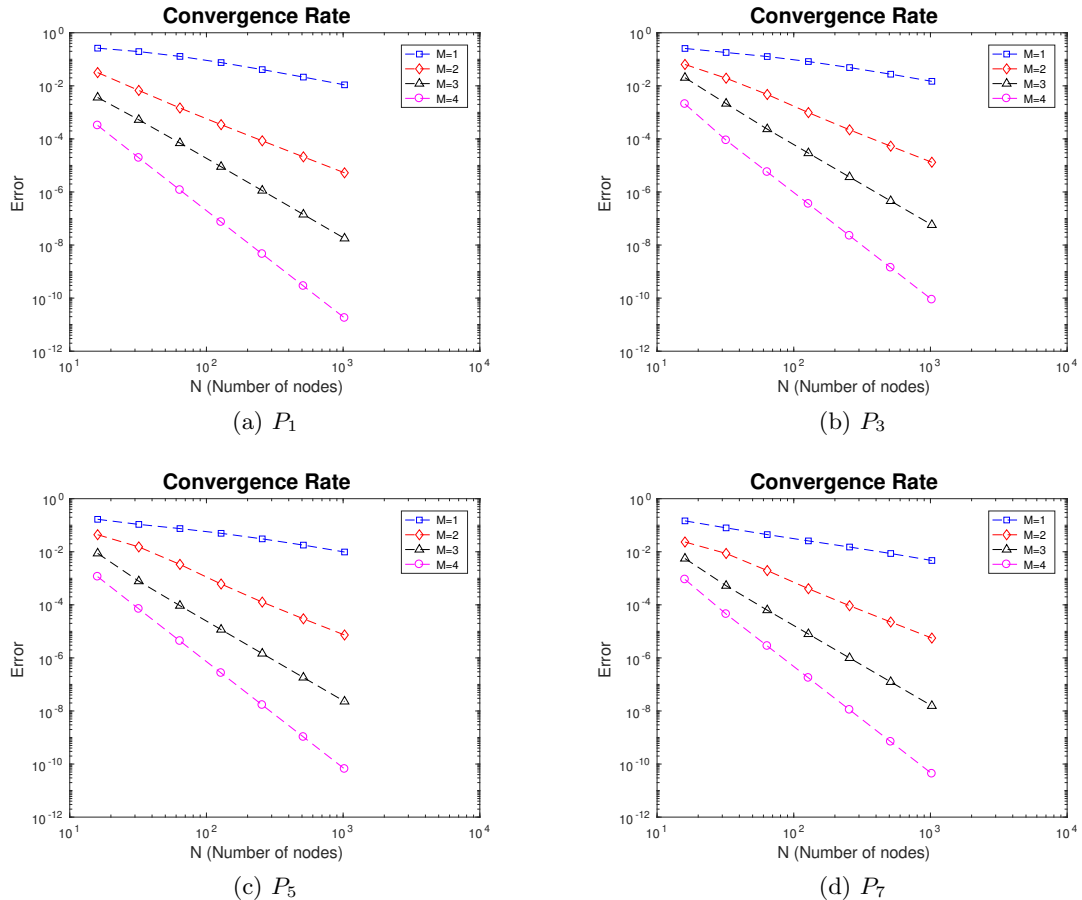


Figure 6.2: The convergence rate of P_N solutions in 1D. Each of P_N solutions show the correct order by our SSP-RK4-DG scheme: 1st, 2nd, 3rd and 4th order, respectively. This shows that our numerical scheme has correct order of accuracy.

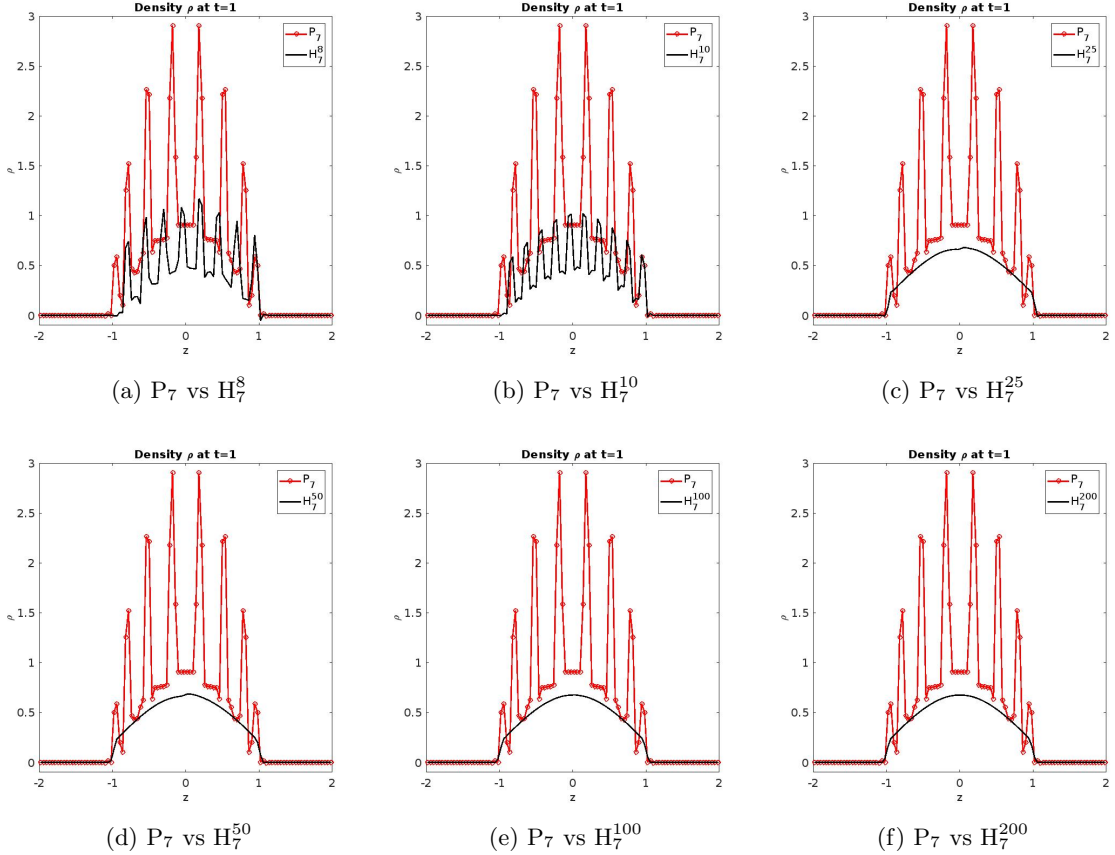


Figure 6.3: The density obtained from P_N and H_N^T solutions in 1D. Red plots represent the P_N solutions, while black plots represent the H_N^T solutions. The H_N^T solution converges to the exact solution as T increases.

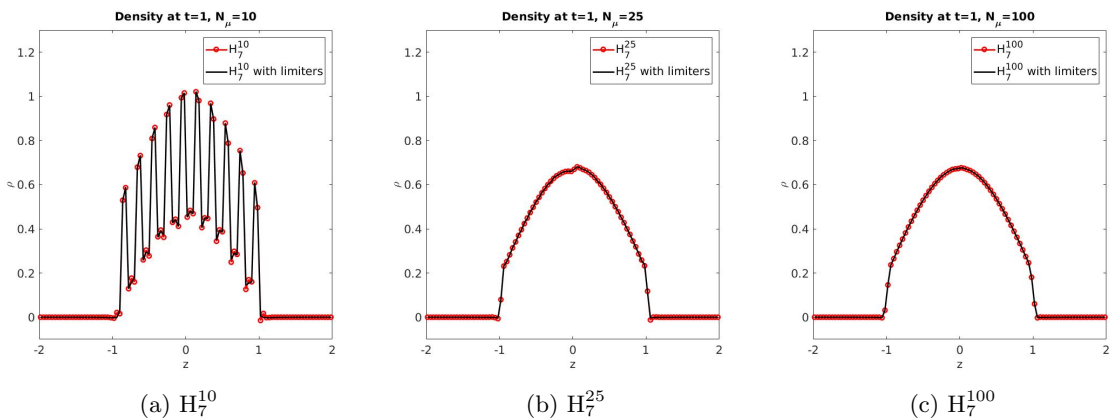


Figure 6.4: The density obtained from H_N^T solutions in 1D. Red plots represent the H_N^T solutions with negative particle concentration near $z = -1$ and $z = 1$, while black plots do not show negativity due to the positivity-preserving limiters.

6.2 Numerical Results in 2D

6.2.1 The line-source problem

We test the line-source problem first. In the line-source problem, the infinite-line source emits a pulse of particles. This problem clearly indicates the differences between various approximations. We compare the P_N and H_N^T solutions to the linear kinetic equation in Figure 6.26. The spatial domain is $[-1.5, 1.5] \times [-1.5, 1.5]$ and all other parameters used in this test is given in Table 6.1.

Table 6.1: Parameters for the 2D line-source problem.

$N_x = 200, N_y = 200$	number of spatial cells
$t_{end} = 1.0$	end time
$\alpha = 0.03$	constant for IC
$\sigma_a = 0$	absorption cross sections
$\sigma_s = 1.0$	scattering cross sections

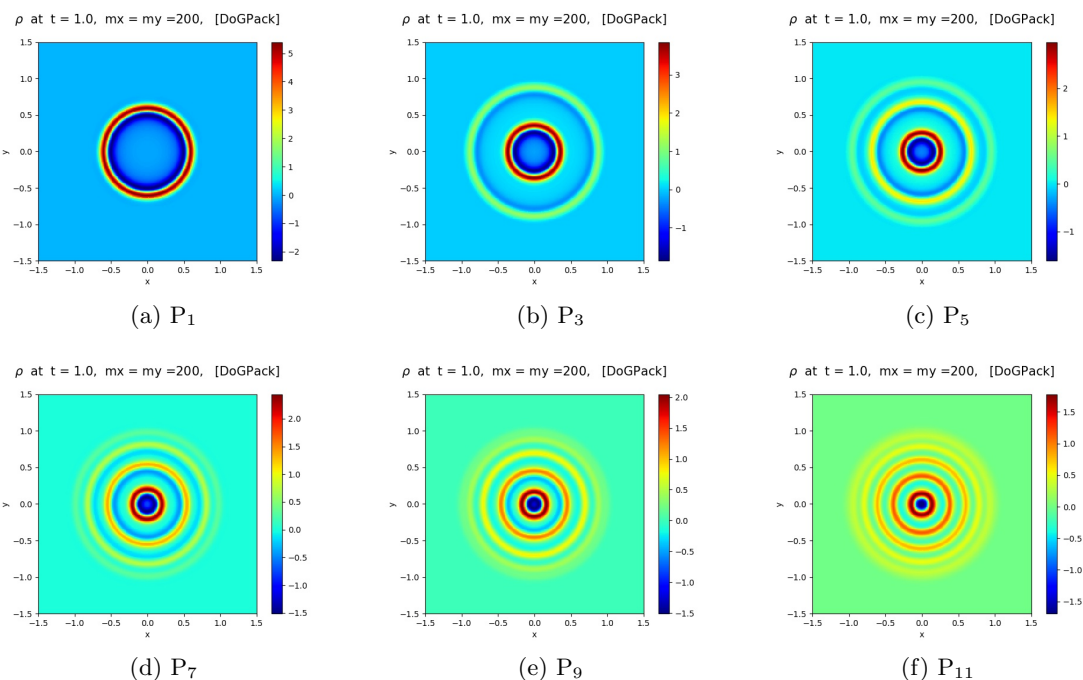


Figure 6.5: P_N solutions with low N in 2D.

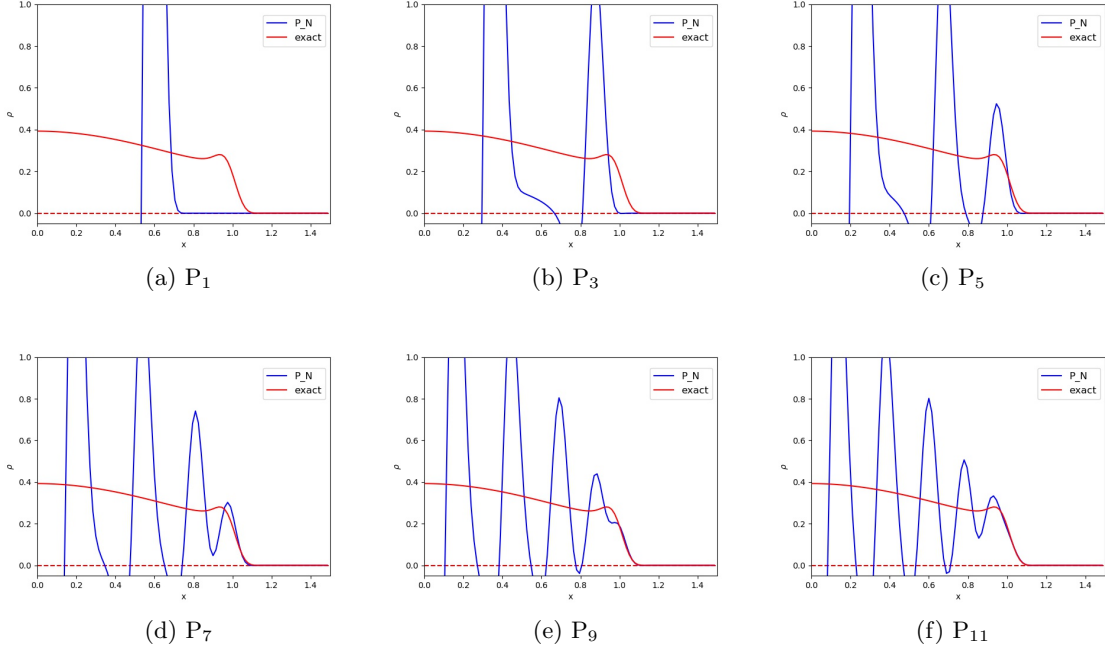
Figure 6.6: P_N solutions with low N in 2D.

Figure 5.2 shows the triangles used in our code. Figure 6.6, 6.8, 6.23, 6.10, and 6.11 show the results under the same initial condition(stEEP Gaussian distribution function):

$$F(\underline{r}, \underline{\Omega}, 0) = \frac{1}{4\pi\alpha^2} \cdot \exp\left(-\frac{x^2 + y^2}{4\alpha^2}\right) \quad (6.1)$$

where $\alpha = 0.03$.

Table 6.2: Convergence rate of spherical error for H_1^T . We fix the order of polynomial basis function ($N = 0$) for each spherical triangle and increase the number of spherical triangles T .

T (for H_1^T)	$\ \rho_N^T - \rho\ _{L^\infty}$	error ratio	order of accuracy
20	1.6809e+00	-	-
80	5.8812e-01	2.8580e+00	1.5150e+00
320	1.3058e-01	4.5039e+00	2.1712e+00
1280	1.5405e-02	8.4764e+00	3.0835e+00
5120	7.8527e-03	1.9617e+00	9.7214e-01

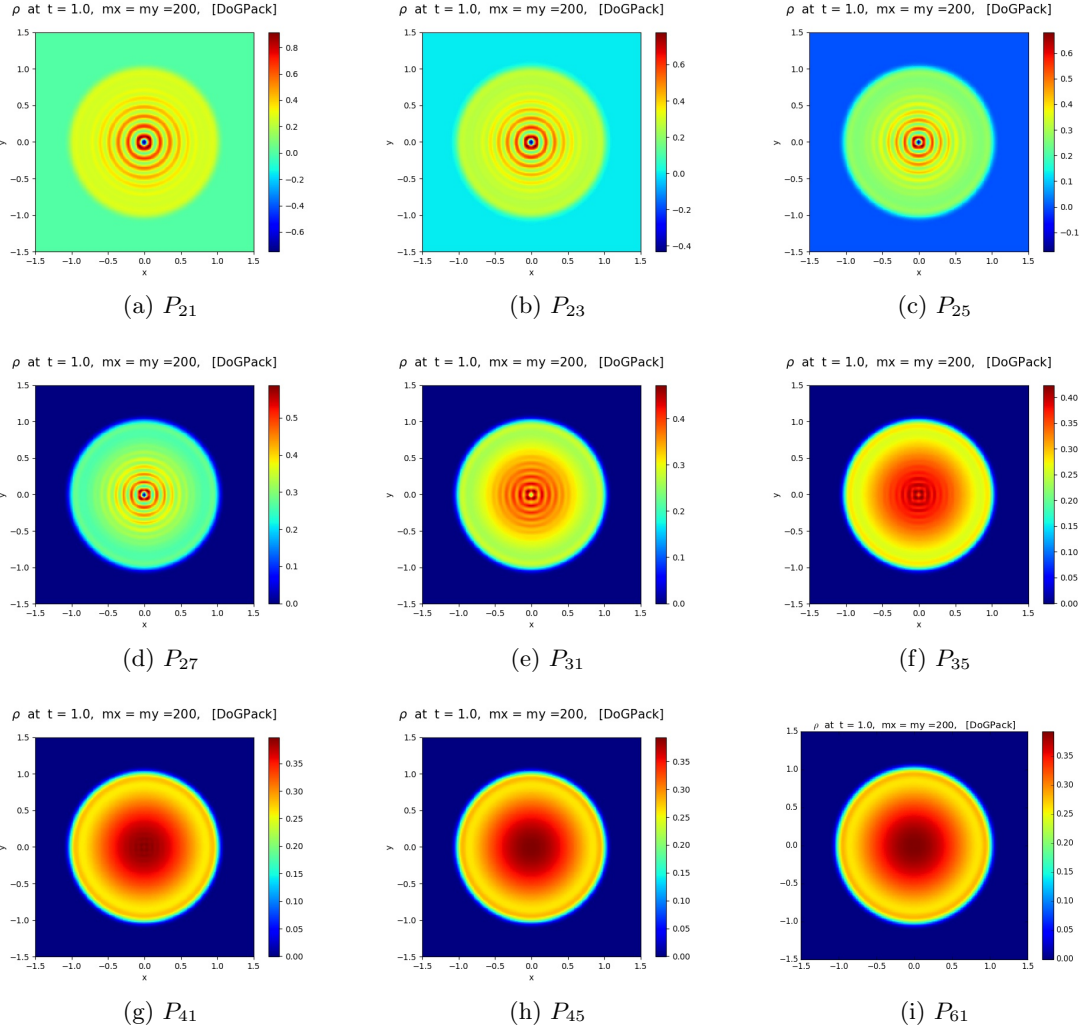
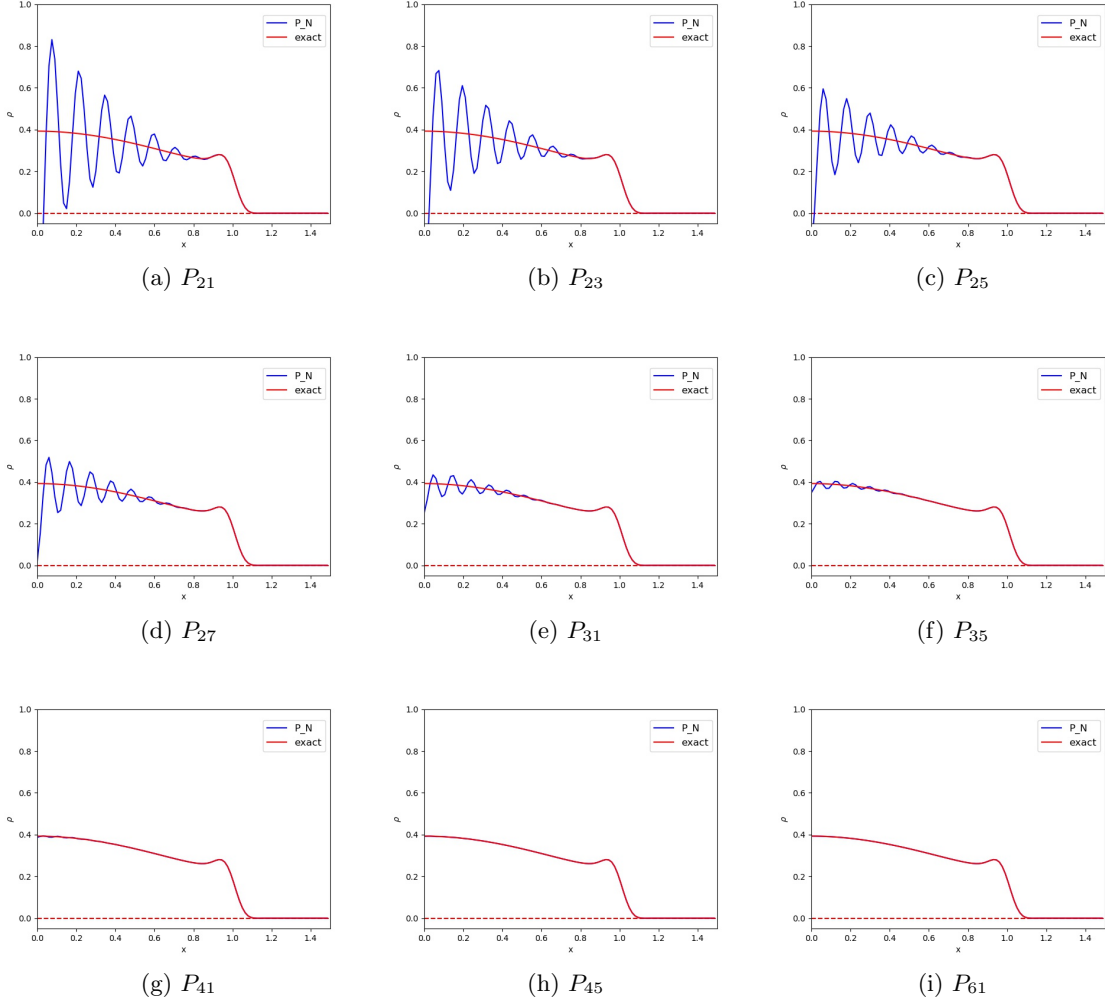


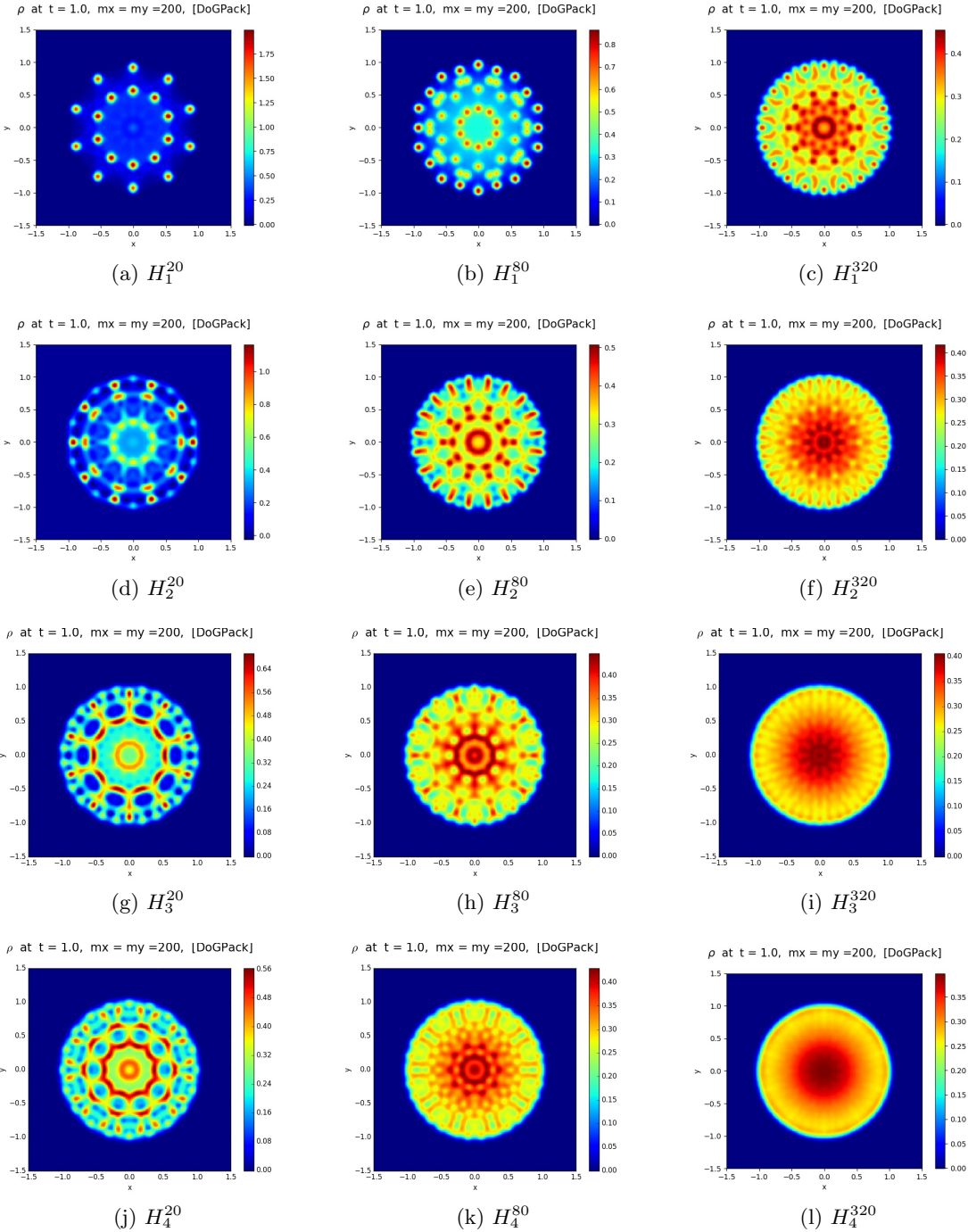
Figure 6.7: P_N solutions with high N in 2D.

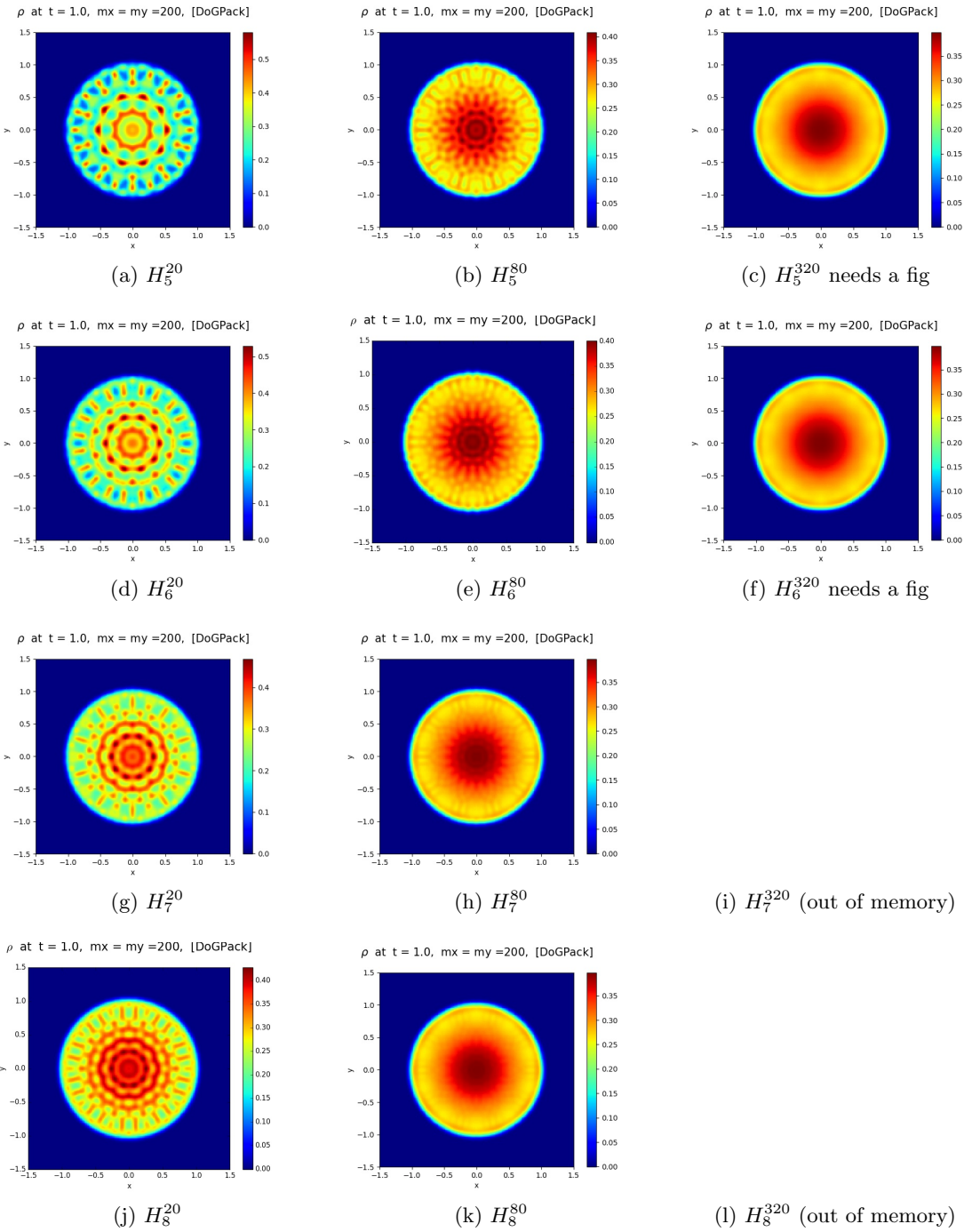
6.2.2 The lattice problem

The next problem we consider is the lattice problem. The checkerboard of highly scattering and highly absorbing regions is considered in this problem. The two-dimensional domain consists of various materials with highly absorbing regions as well as highly scattering regions [8]. There is no initial radiation and an isotropic source of strength one is located in the center(yellow) region, i.e., $S(\underline{r}, \underline{\Omega}, t) = 1$ if $\underline{r} \in [3, 4] \times [-4, -3]$, otherwise $S = 0$. The spatial domain is $[0, 7] \times [-7, 0]$ and all other parameters used in this test can be found in Table 6.9. The logarithmic density $\log_{10} \rho$ is plotted for the lattice problem.

Figure 6.8: P_N solutions with high N in 2D.Table 6.3: Convergence rate of spherical error for H_2^T . We fix the order of polynomial basis function ($N = 1$) for each spherical triangle and increase the number of spherical triangles T .

T (for H_2^T)	$\ \rho_N^T - \rho\ _{L^\infty}$	error ratio	order of accuracy
20	8.8715e-01	-	-
80	2.0092e-01	4.4155e+00	2.1426e+00
320	3.9717e-02	5.0587e+00	2.3388e+00
1280	8.9674e-03	4.4290e+00	2.1470e+00

Figure 6.9: H_N^T for the line source problem in 2D.

Figure 6.10: H_N^T for the line source problem in 2D.

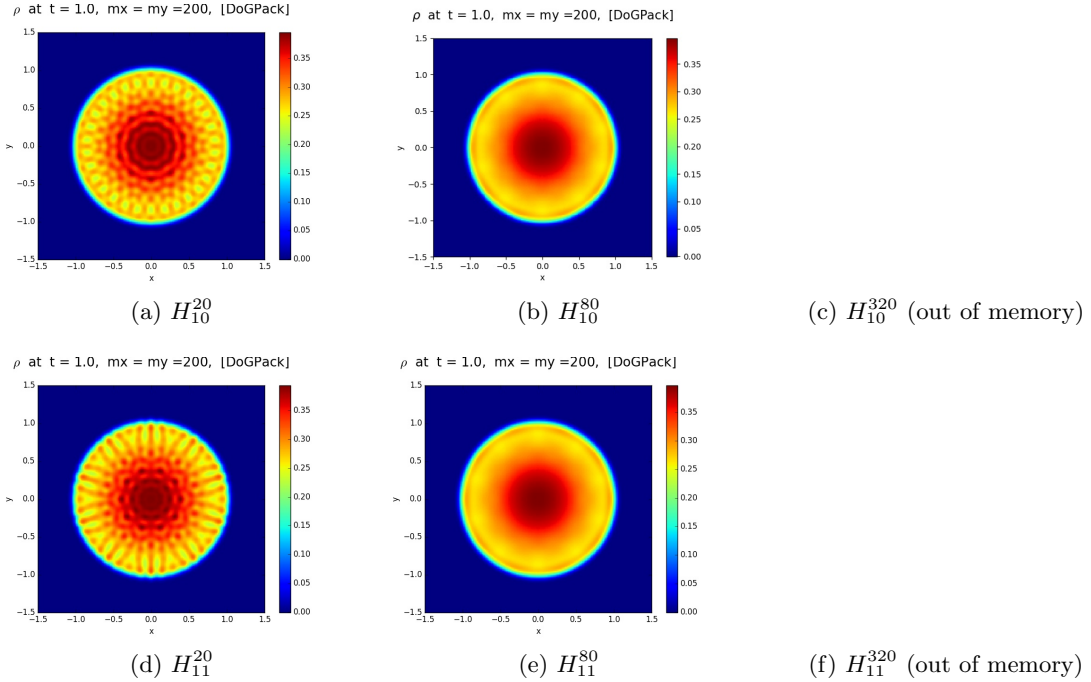


Figure 6.11: H_N^T for the line source problem in 2D.

Table 6.4: Convergence rate of spherical error for H_3^T . We fix the order of polynomial basis function ($N = 2$) for each spherical triangle and increase the number of spherical triangles T .

T (for H_3^T)	$\ \rho_N^T - \rho\ _{L^\infty}$	error ratio	order of accuracy
20	4.0809e-01	-	-
80	1.3966e-01	2.9221e+00	1.5470e+00
320	1.8886e-02	7.3947e+00	2.8865e+00

Table 6.5: Convergence rate of spherical error for H_4^T . We fix the order of polynomial basis function ($N = 3$) for each spherical triangle and increase the number of spherical triangles T .

T (for H_4^T)	$\ \rho_N^T - \rho\ _{L^\infty}$	error ratio	order of accuracy
20	2.4613e-01	-	-
80	5.9547e-02	4.1334e+00	2.0473e+00
320	9.2038e-03	6.4698e+00	2.6937e+00

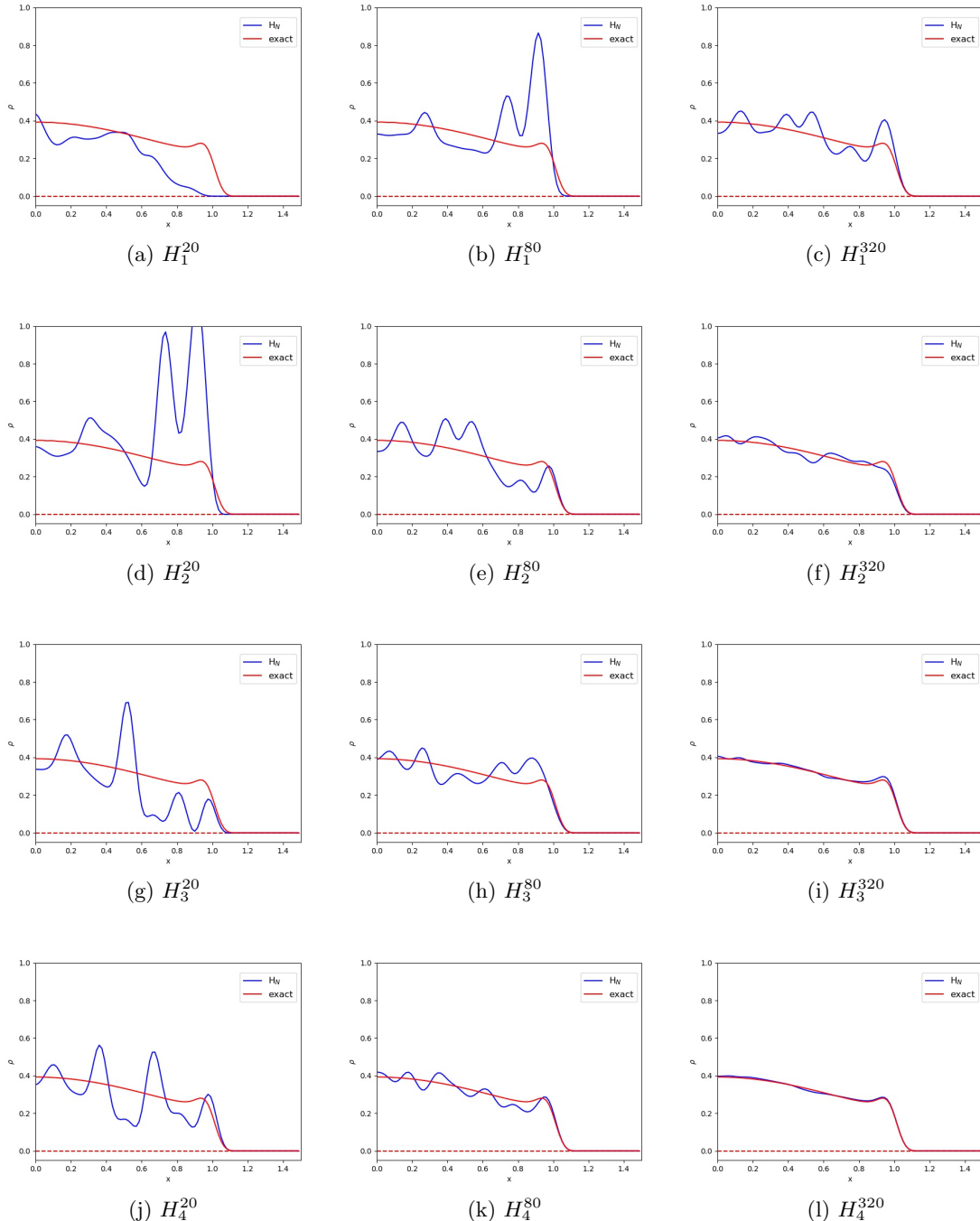


Figure 6.12: H_N^T for the line source problem in 2D (cross section along x-axis).

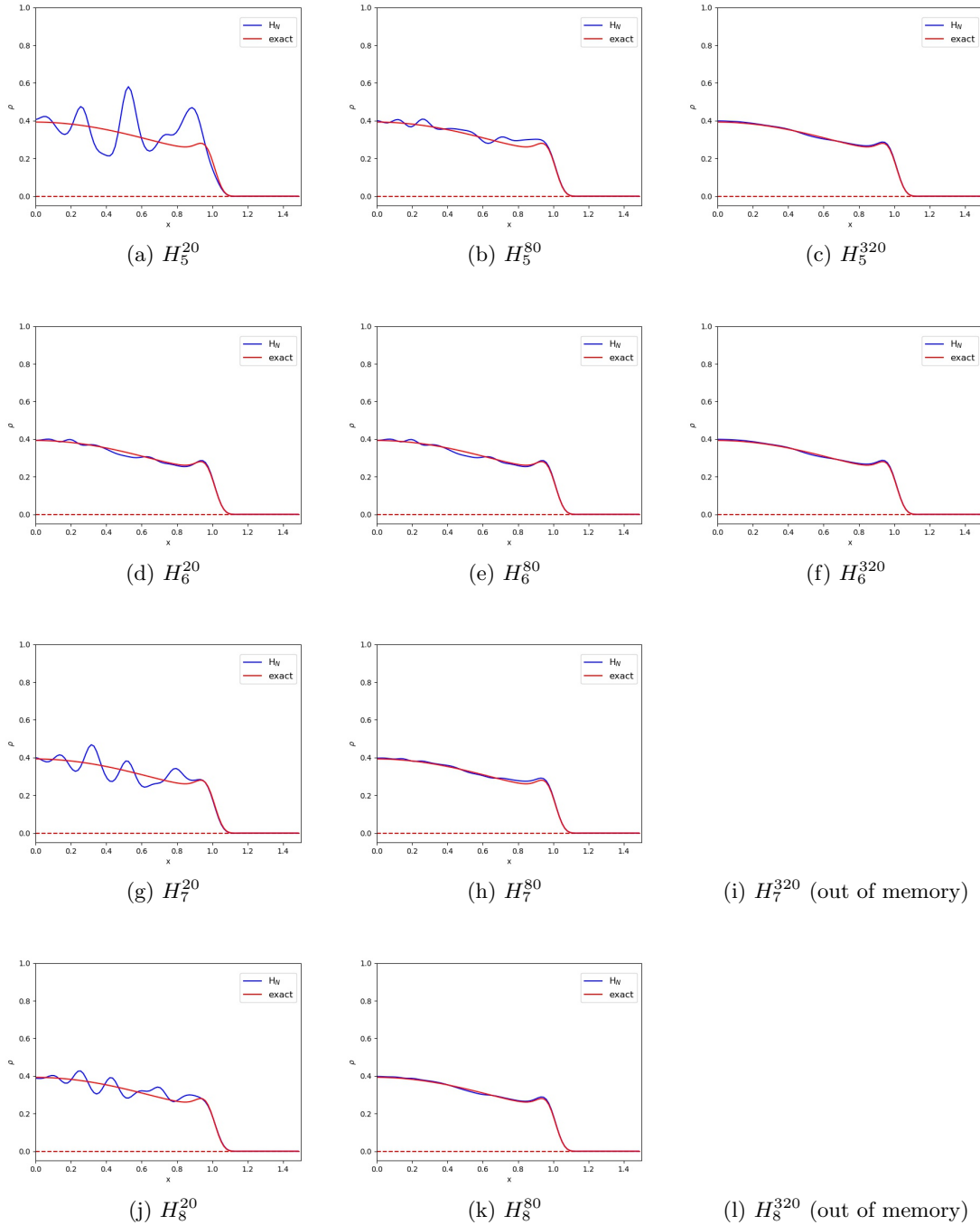


Figure 6.13: H_N^T for the line source problem in 2D (cross section along x-axis).

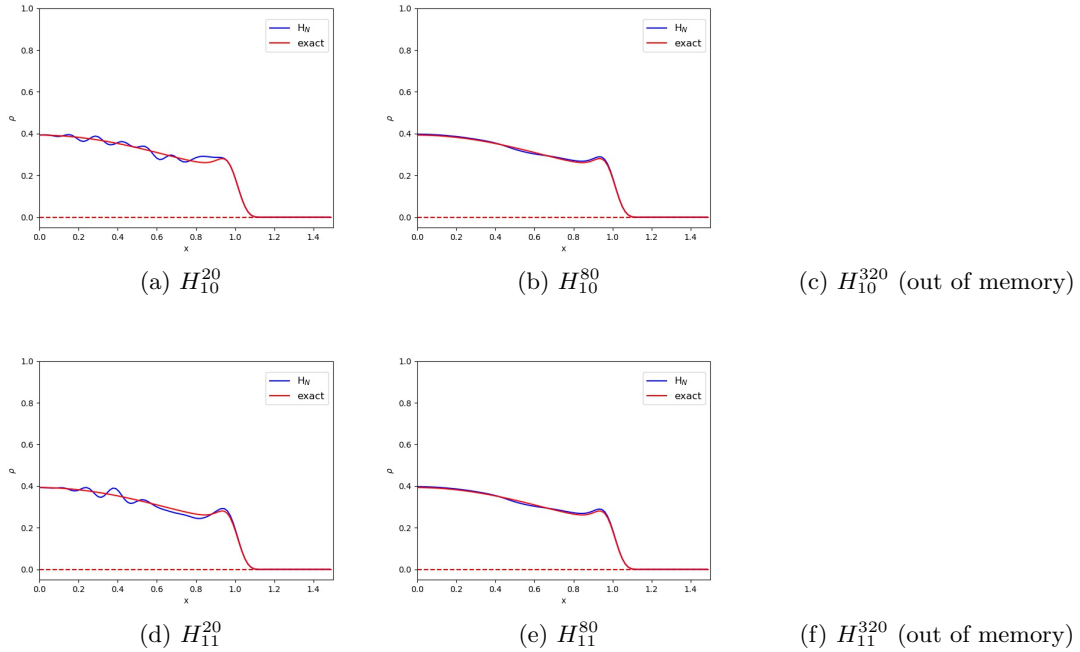


Figure 6.14: H_N^T for the line source problem in 2D (cross section along x-axis).

Table 6.6: Convergence rate of spherical error for H_N^{20} . Here we fix the number of spherical triangles ($T = 20$) and increase the order of polynomial basis function for each triangle from 0 to 10.

N (for H_N^{20})	$\ \rho_N^T - \rho\ _{L^\infty}$	error ratio
1	1.6809e+00	-
2	8.8715e-01	1.8947e+00
3	4.0809e-01	2.1739e+00
4	2.4613e-01	1.6580e+00
5	2.5370e-01	9.7018e-01
6	1.7793e-01	1.4258e+00
7	1.0171e-01	1.7493e+00
8	6.8681e-02	1.4810e+00
9	5.6241e-02	1.2212e+00
10	3.6031e-02	1.5609e+00
11	4.0637e-02	8.8667e-01

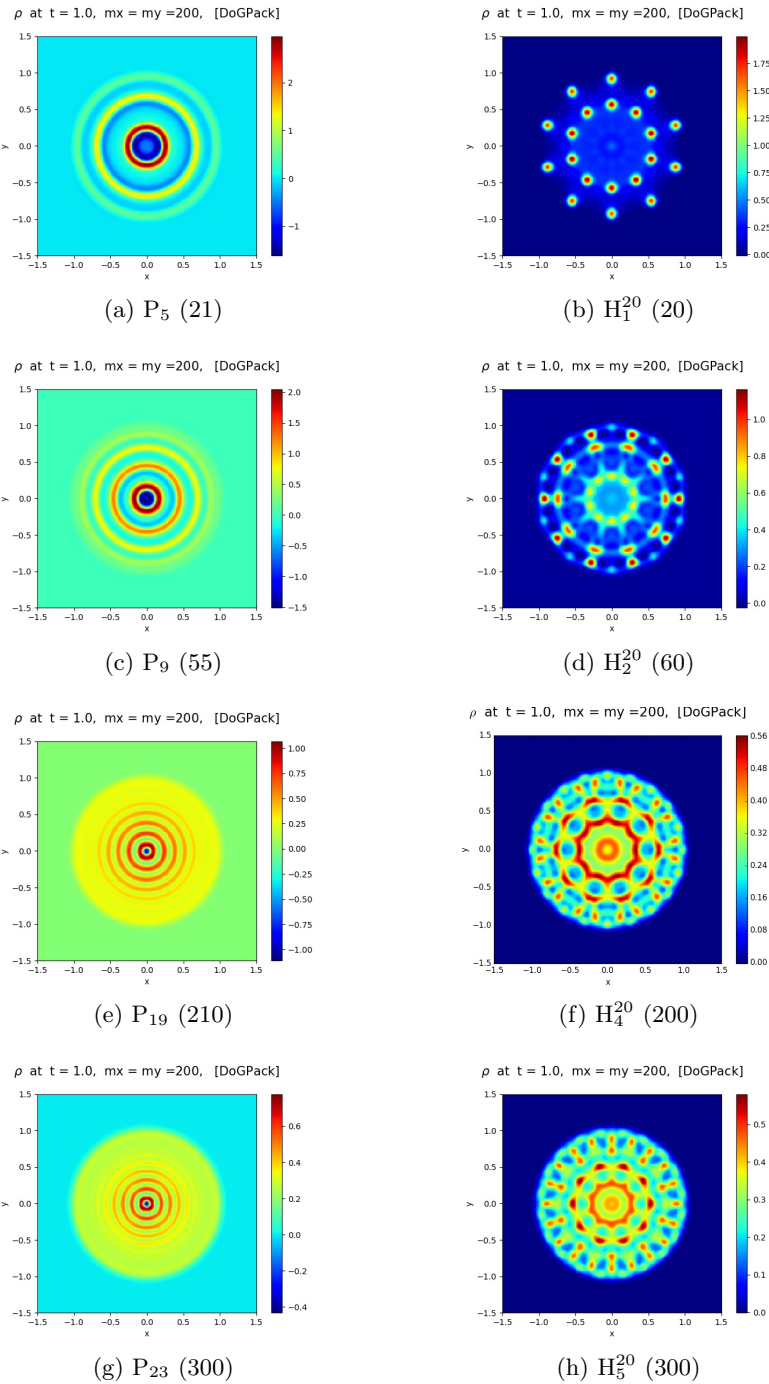


Figure 6.15: P_N vs H_N^T with similar number of equations.

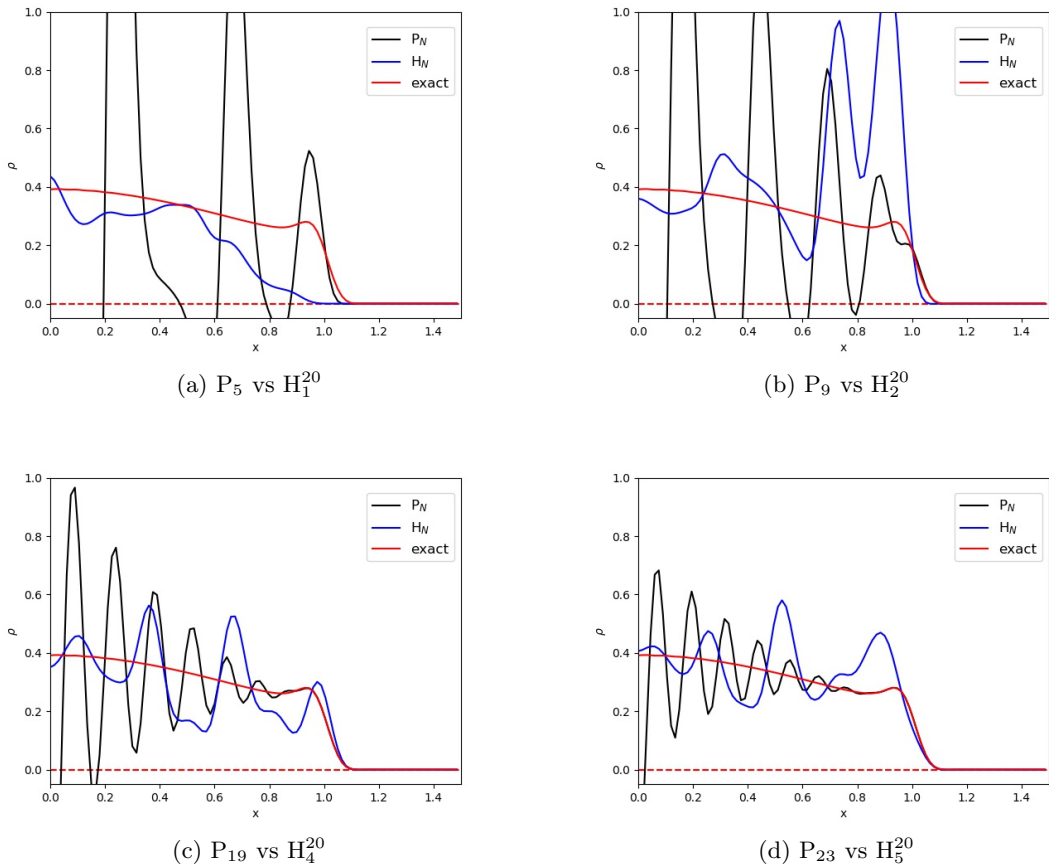


Figure 6.16: P_N vs H_N^T with similar number of equations (cross-section along x-axis). Red plots are the exact solutions for the line source problem with the initial condition (6.2). Black plots are P_N solutions and blue plots are H_N^T solutions. Each plot has the similar number of equations for efficiency comparison. H_N^T approximations tend to have better accuracy than P_N approximations for relatively small number of equations.

Table 6.7: Convergence rate of spherical error for H_N^{80} . We fix the number of spherical triangles ($T = 80$) and increase the order of polynomial basis function for each triangle from 0 to 10.

N (for H_N^{80})	$\ \rho_N^T - \rho\ _{L^\infty}$	error ratio
1	5.8812e-01	-
2	2.0092e-01	2.9272e+00
3	1.3966e-01	1.4387e+00
4	5.9547e-02	2.3453e+00
5	3.8715e-02	1.5381e+00
6	2.0420e-02	1.8959e+00
7	1.3775e-02	1.4824e+00
8	9.9901e-03	1.3789e+00

Table 6.8: Convergence rate of spherical error for H_N^{320} . We fix the number of spherical triangles ($T = 320$) and increase the order of polynomial basis function for each triangle from 0 to 5. Due to the limit of memory, it is impossible to test higher order in our computational environment.

N (for H_N^{320})	$\ \rho_N^T - \rho\ _{L^\infty}$	error ratio
1	1.3058e-01	-
2	3.9717e-02	3.2877e+00
3	1.8886e-02	2.1030e+00
4	9.2038e-03	2.0520e+00
5	7.7924e-03	1.1811e+00
6	7.6843e-03	1.0141e+00

Table 6.9: Parameters for the lattice problem.

$N_x = 280, N_y = 280$	number of spatial cells
$t_{end} = 3.2$	end time
$\sigma_a = 0, \sigma_s = 1.0$	cross sections of blue region
$\sigma_a = 10.0, \sigma_s = 0$	cross sections of squares
S=1	strength of source

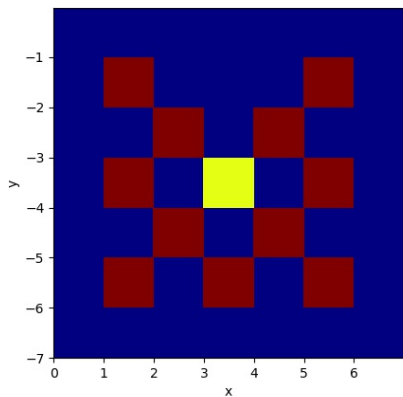


Figure 6.17: The lattice system: Red and yellow regions are highly absorbing while blue regions are highly scattering. The source of strength one is located in the center (yellow) region.

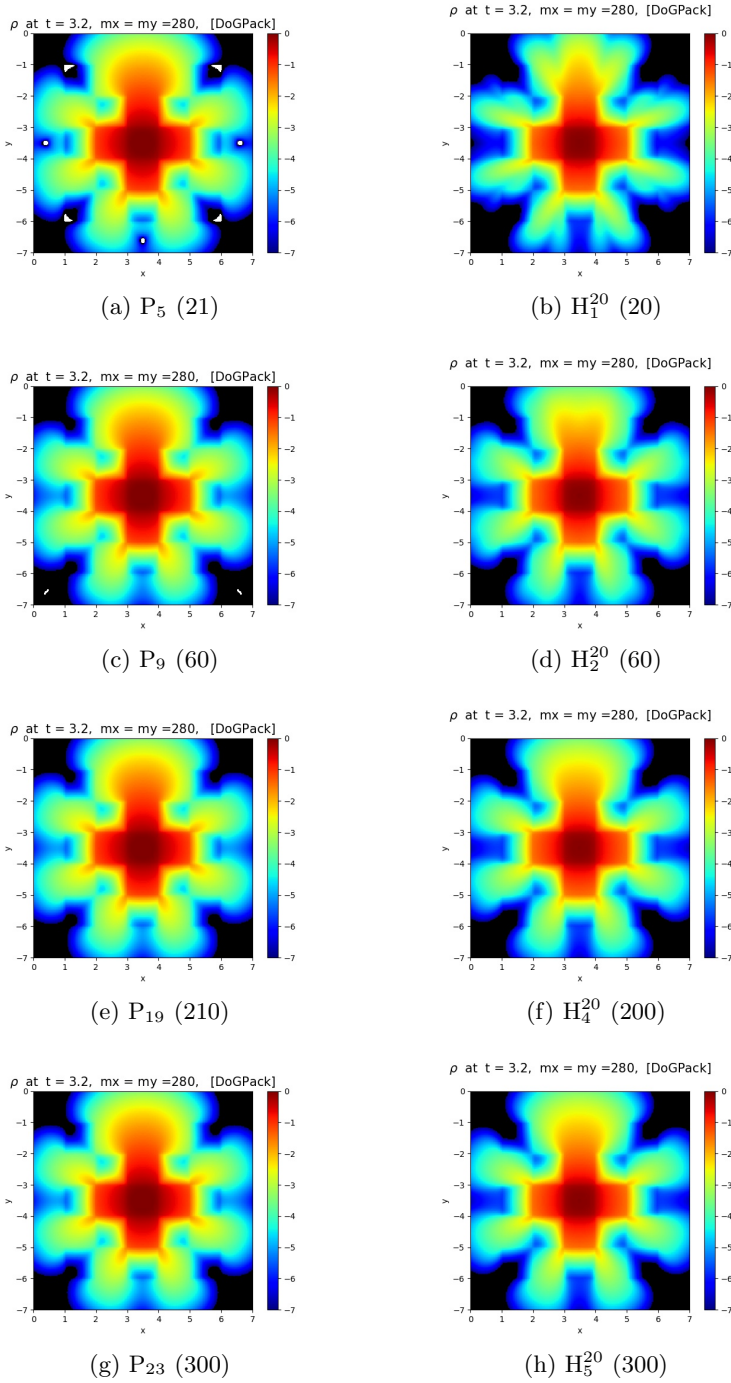
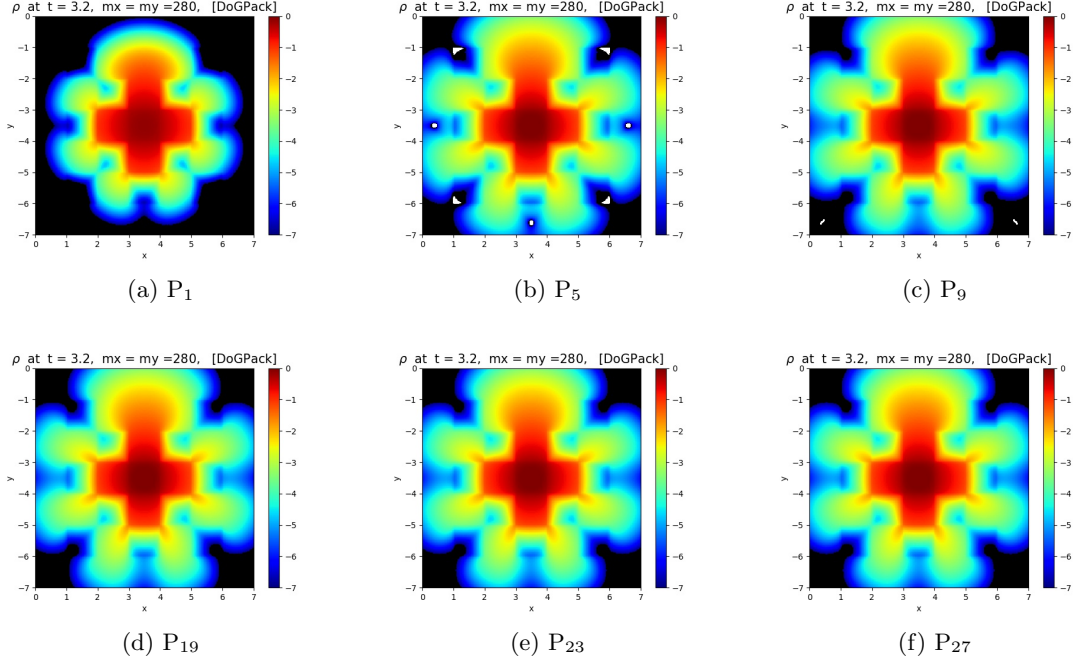
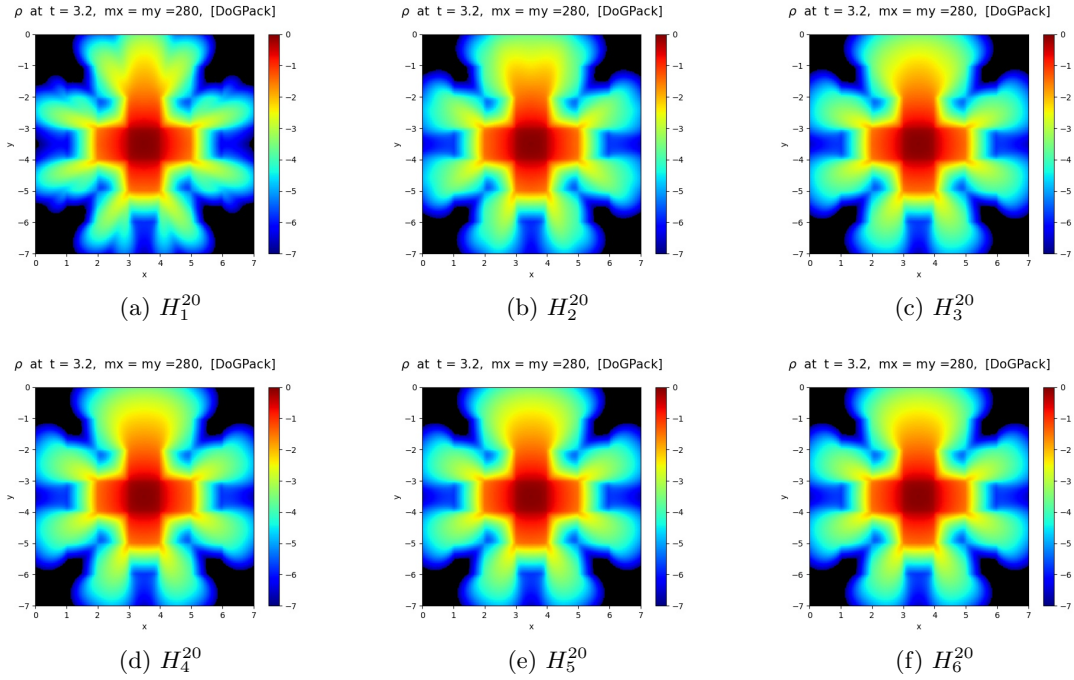


Figure 6.18: Lattice solution with P_N vs H_N^T .

Figure 6.19: Lattice P_N solutions in 2D.Figure 6.20: Lattice H_N^T solutions in 2D.

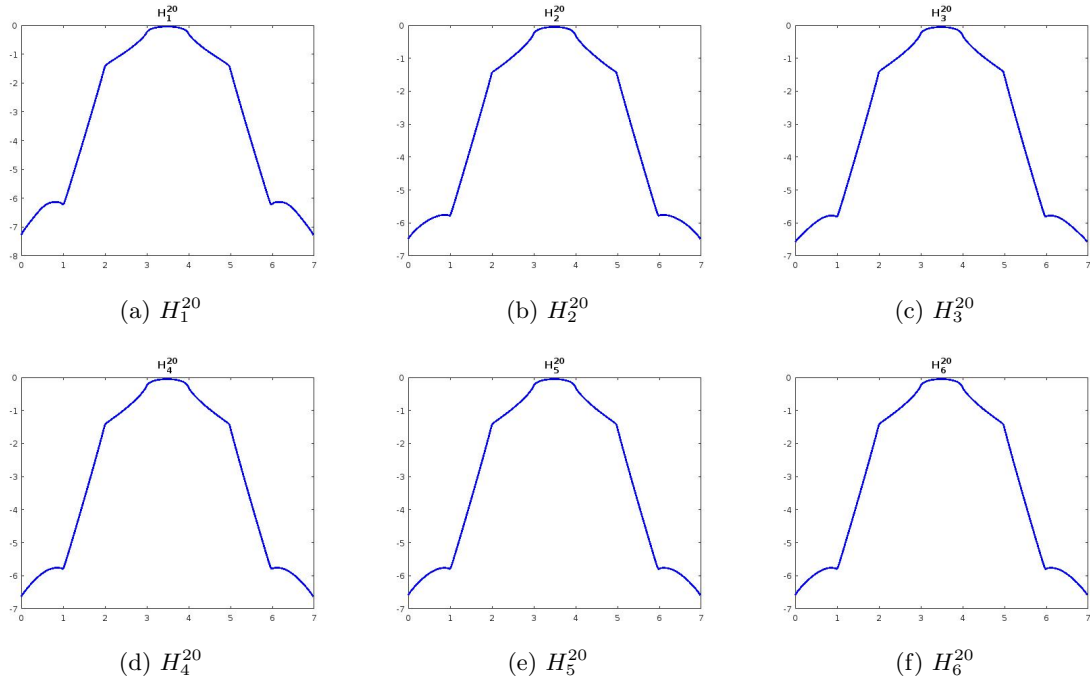


Figure 6.21: Lattice H_N^T solutions in 2D (cross-section along x-axis from center).

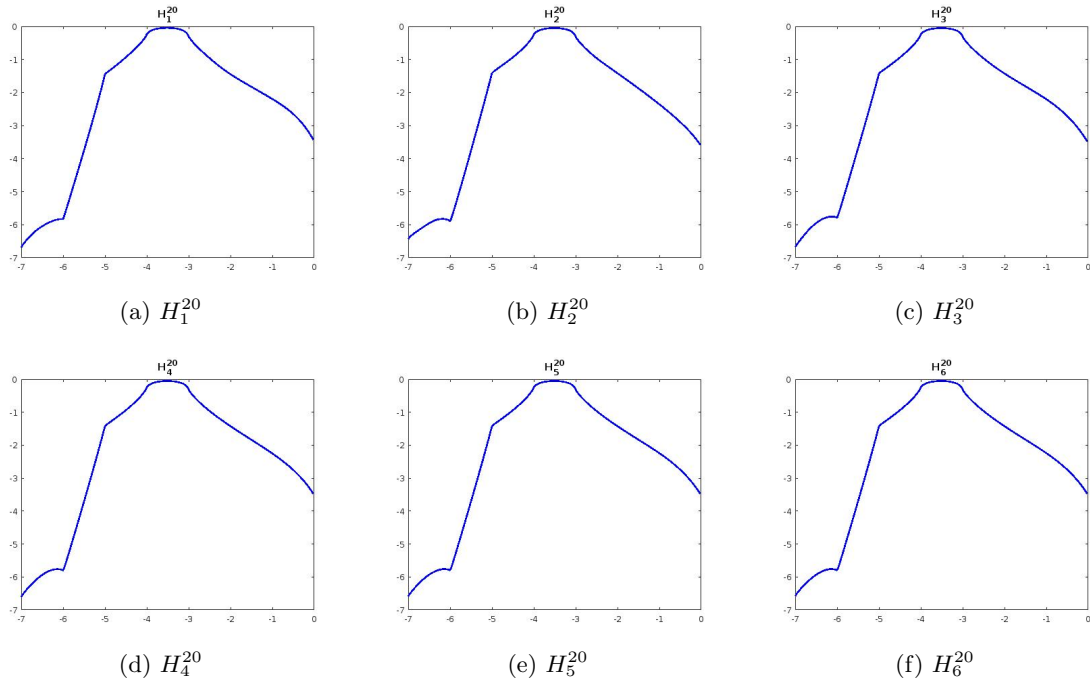


Figure 6.22: Lattice H_N^T solutions in 2D (cross-section along y-axis from center).

6.3 Numerical Results in 2D with Octantal-Spherical-Triangular Mesh

In this section, instead of using equilateral triangles in Figure 5.2 generated by MeshGenC++, we adopt the octantal-triangles (i.e. each triangle is in each octant in three dimensional Cartesian coordinate) projection to the spherical triangles 5.3 used in [32]. In the first level, there are only 8 spherical triangles on the unit sphere \mathbb{S}^2 . This allows to align the flux directions so that we can achieve better implementation of boundary conditions.

We do the same procedure with same parameters as in 6.2 to test the line-source problem with octantal-spherical-triangular mesh. The initial condition (steep Gaussian distribution function) is same as in the previous section 6.2

$$F(\underline{r}, \underline{\Omega}, 0) = \frac{1}{4\pi\alpha^2} \cdot \exp\left(-\frac{x^2 + y^2}{4\alpha^2}\right) \quad (6.2)$$

where $\alpha = 0.03$.

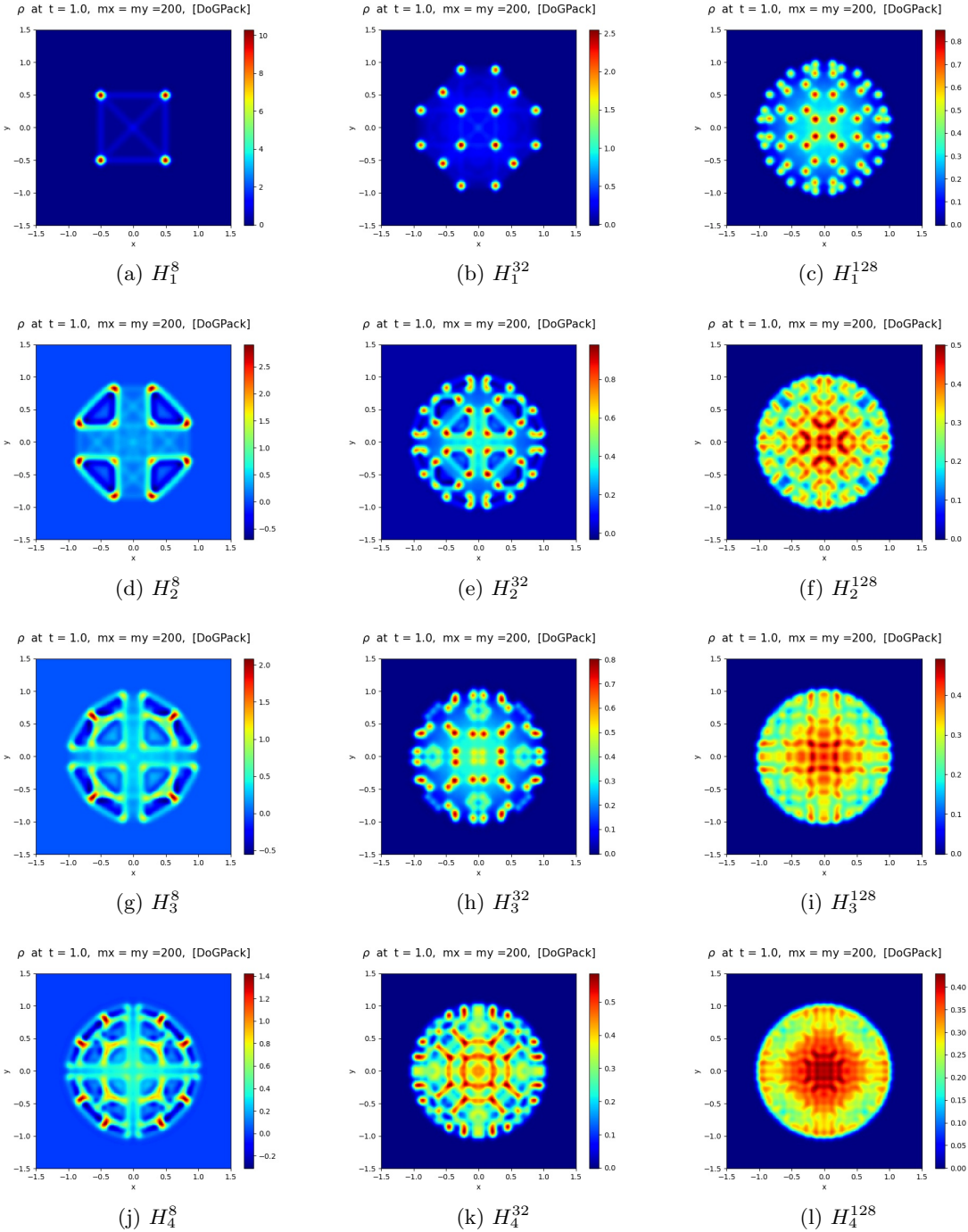


Figure 6.23: H_N^T for the line source problem in 2D.

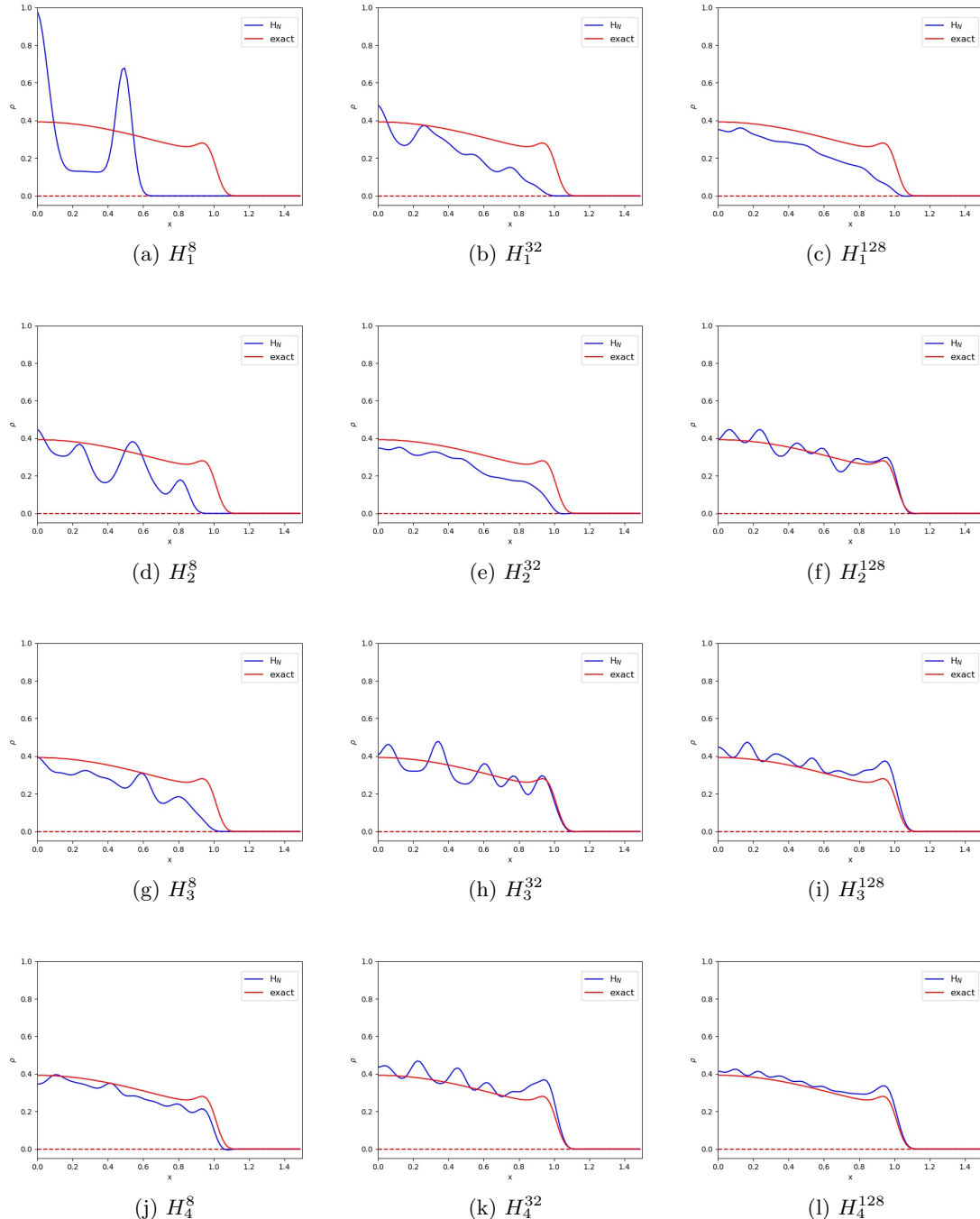


Figure 6.24: H_N^T for the line source problem in 2D (cross section along x-axis).

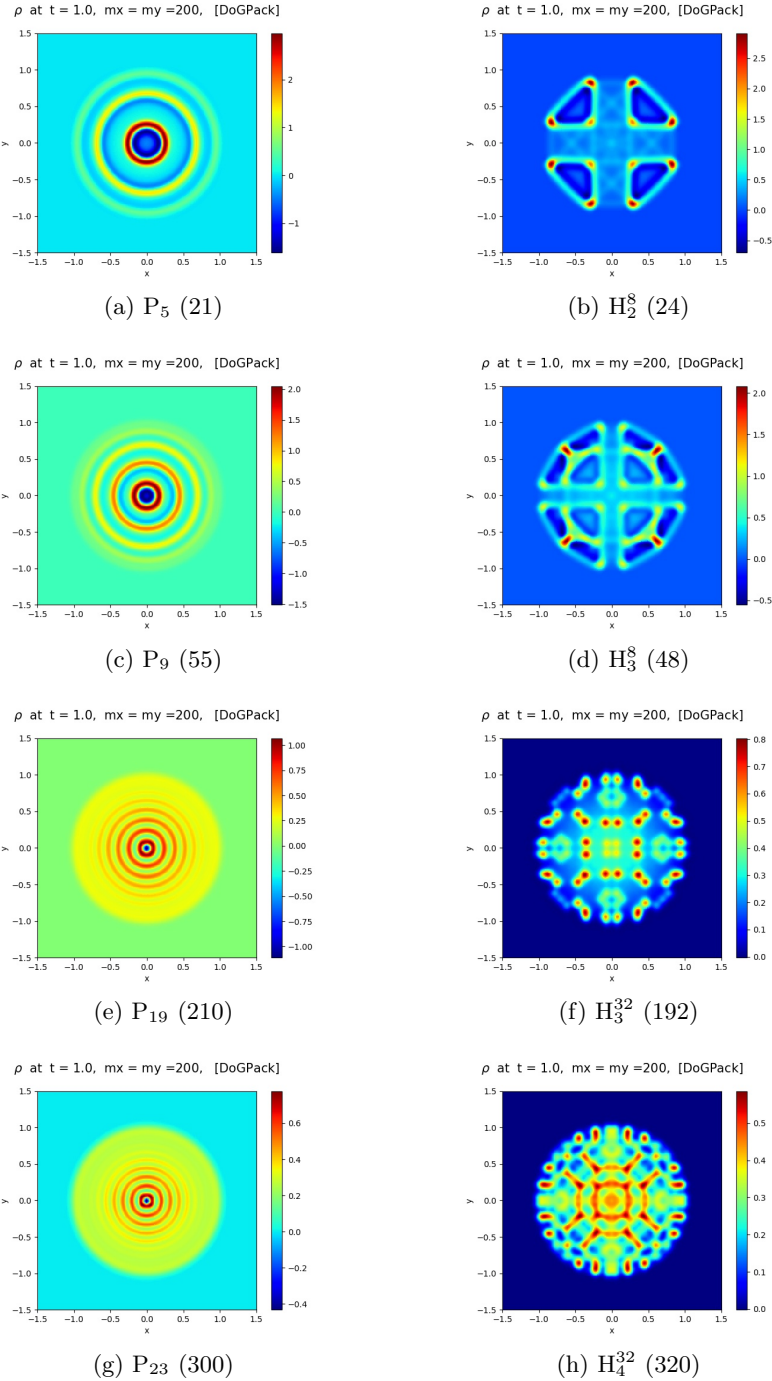


Figure 6.25: P_N vs H_N^T with similar number of equations.

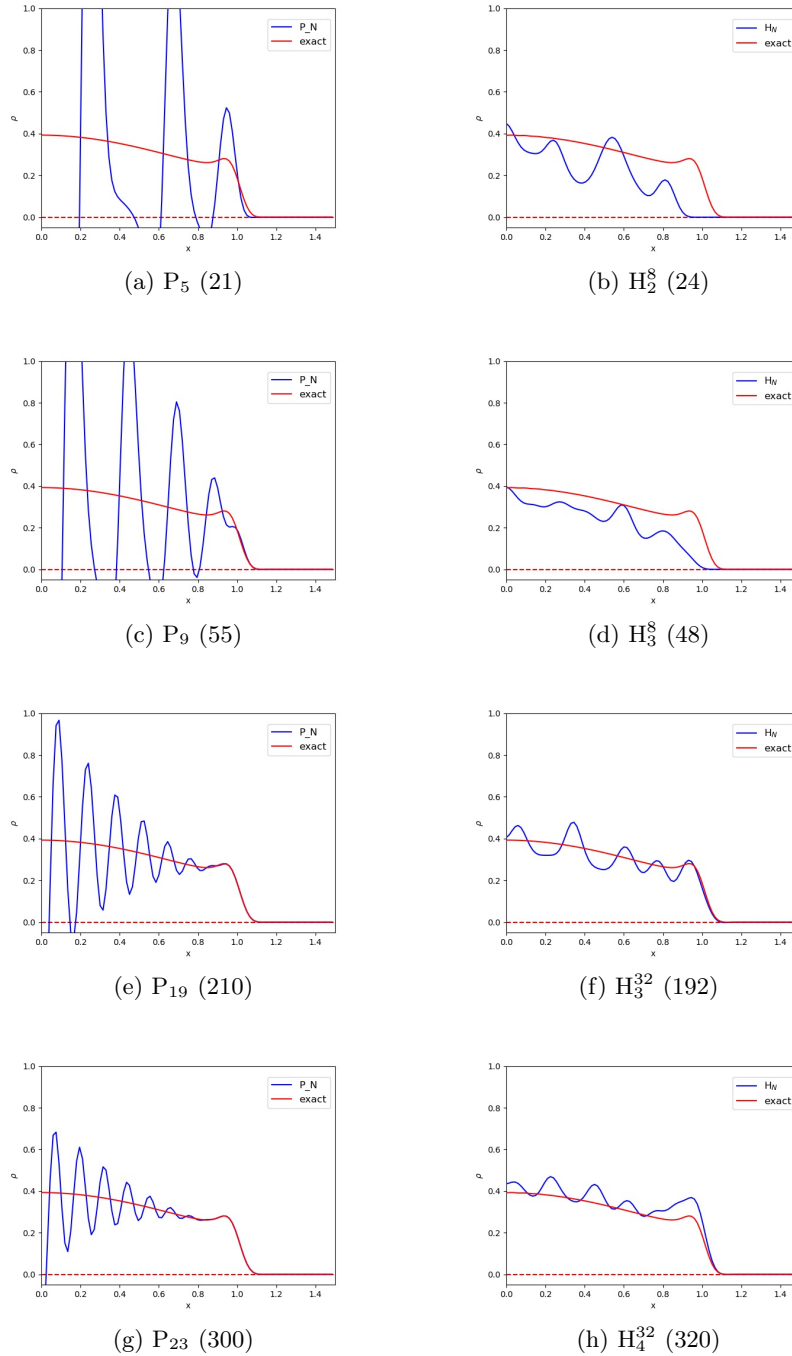


Figure 6.26: P_N vs H_N^T with similar number of equations.

CHAPTER 7. H_N^T APPROXIMATION WITH RICHARDSON EXTRAPOLATION

This is an attempt at improving H_N^T scheme using the Richardson extrapolation. The mesh size is reduced to approximately half, but not exactly half because our scheme uses the spherical-triangular mesh. The mesh size becomes half for the triangles on the plane, however, it does not become exactly half on the spherical mesh.

Instead of using equilateral triangles in Figure 5.2 generated by MeshGenC++, we adopt the octant triangles projection to the spherical triangles in Figure 5.3 used in [32]. In the first level, there are only 8 spherical triangles on the unit sphere \mathbb{S}^2 . Hence this mesh has a better refinement for the Richardson extrapolation. Since the density is the most important measure in most cases, we calculate the error of the density in L^∞ .

7.1 Derivation

When T and N are relatively small in the H_N^T method, the error of the solution is not dominated by the time error nor spatial error. Therefore, we only consider the spherical error produced by the H_N^T method.

Let h be the size of a triangle and assume

$$\rho_N^T = \rho + c_1 h^k + c_2 h^{k+1} + c_3 h^{k+2} + \mathcal{O}(h^{k+3}). \quad (7.1)$$

Then by reducing the size of each spherical triangle, we get

$$\rho_N^{4T} = \rho + c_1 \left(\frac{h}{2}\right)^k + c_2 \left(\frac{h}{2}\right)^{k+1} + c_3 \left(\frac{h}{2}\right)^{k+2} + \mathcal{O}\left(\frac{h}{2}\right)^{k+3}. \quad (7.2)$$

Now multiply (7.2) by 2^k and subtract (7.1) to get

$$2^k \rho_N^{4T} - \rho_N^T = (2^k - 1)\rho + c_2 h^{k+1} \left(\frac{1}{2} - 1\right) + c_3 h^{k+2} \left(\frac{1}{2^2} - 1\right) + \mathcal{O}(h^{k+3}). \quad (7.3)$$

Dividing (7.3) by $2^k - 1$, we get

$$\frac{2^k \rho_N^{4T} - \rho_N^T}{2^k - 1} = \rho + c_2 h^{k+1} \frac{\left(\frac{1}{2} - 1\right)}{2^k - 1} + c_3 h^{k+2} \frac{\left(\frac{1}{2^2} - 1\right)}{2^k - 1} + \mathcal{O}(h^{k+3}). \quad (7.4)$$

Repeating this process is called the Richardson extrapolation, and by doing this, we can achieve better approximation, theoretically.

7.2 Numerical Results

Here we solve the same line source problem with the original spherical-triangular mesh. For the error tables of the Richardson extrapolation with the original H_N^T method, see the Table 7.1 and Table 7.2.

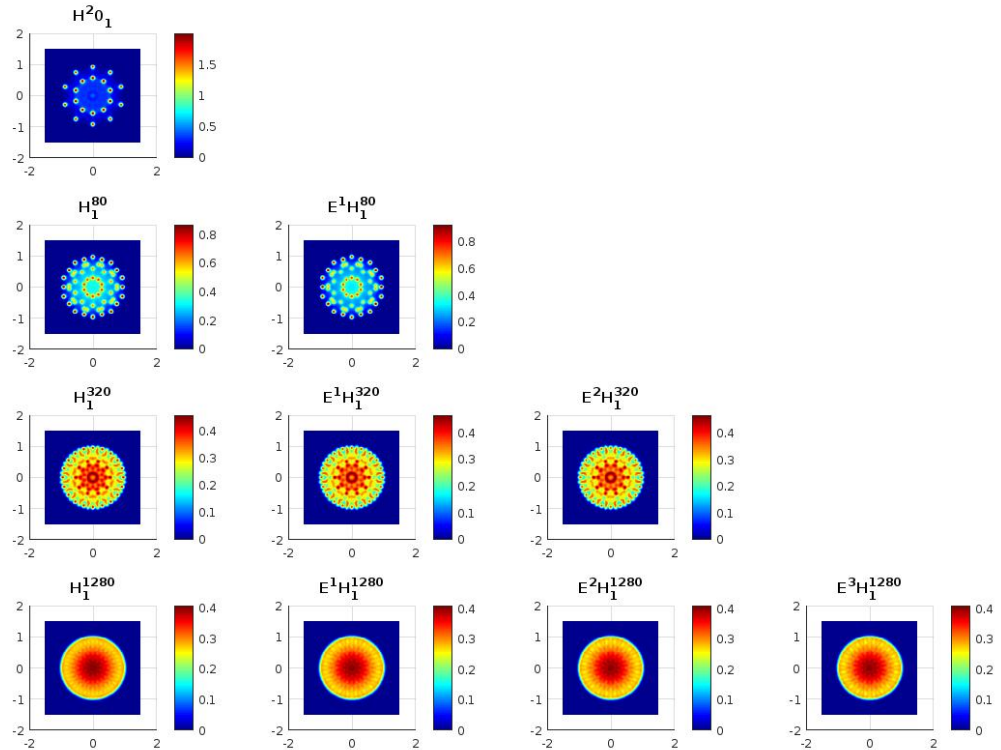


Figure 7.1: H_1^T solutions with Richardson extrapolation with the original spherical triangular mesh.

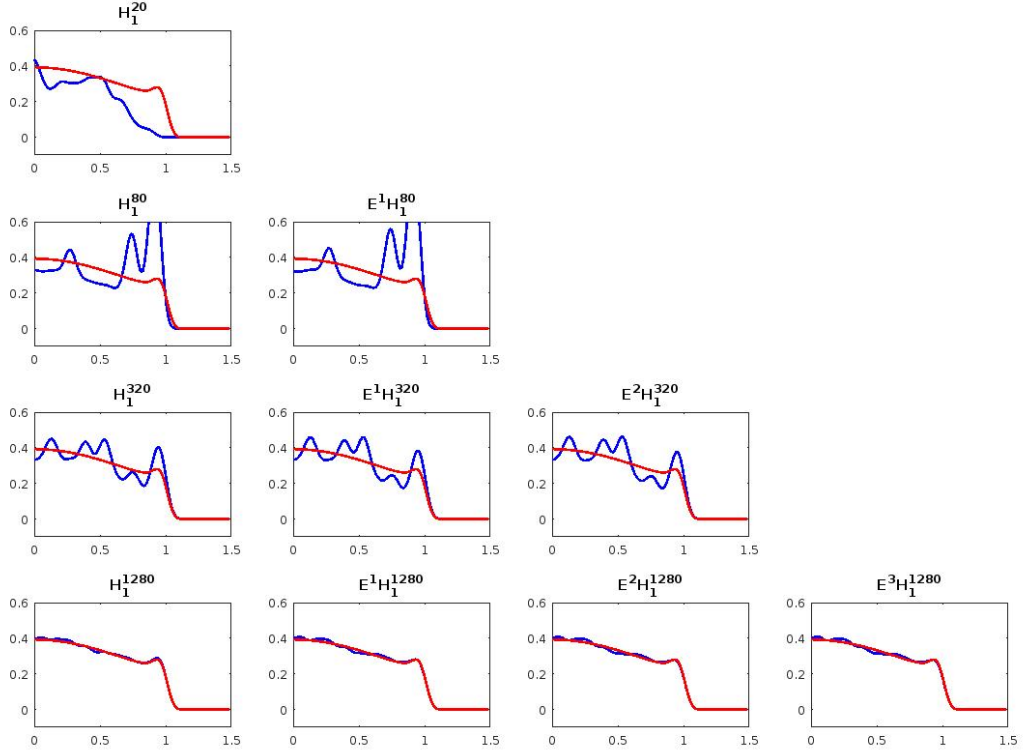


Figure 7.2: H_1^T solutions with Richardson extrapolation (cross-section along x-axis from center) with the original spherical triangular mesh.

Table 7.1: Error of H_1^T with Richardson extrapolation. With the Richardson extrapolation, we cannot obtain any improvement of the original error with the spherical triangular mesh. This might due to the refinement process of our spherical triangular mesh generation. Even though the number of spherical triangles become four times at the next step, the size of each triangle is not exactly one half of previous triangle.

T	$\ \rho_2^T - \rho\ _{L^\infty}$	$\ E^1 \rho_2^T - \rho\ _{L^\infty}$	$\ E^2 \rho_2^T - \rho\ _{L^\infty}$	$\ E^3 \rho_2^T - \rho\ _{L^\infty}$
20	1.6809e+00	-	-	-
80	5.8812e-01	6.4409e-01	-	-
320	1.3058e-01	1.3797e-01	1.4147e-01	-
1280	1.5405e-02	1.9325e-02	2.0392e-02	2.0665e-02

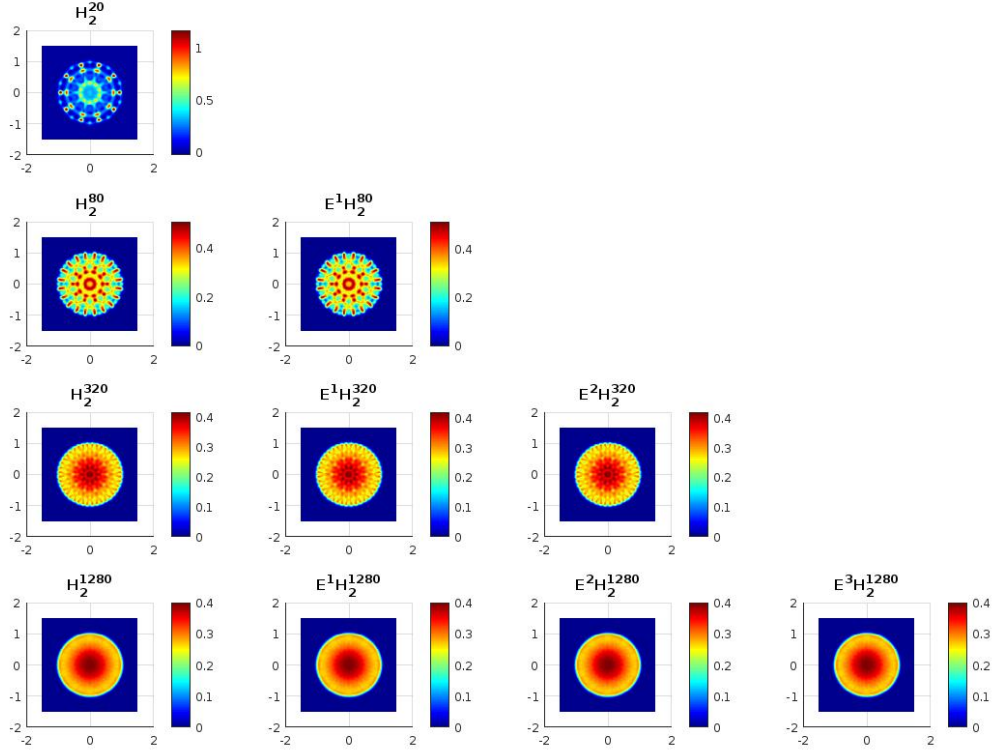


Figure 7.3: H_2^T solutions with Richardson extrapolation with the original spherical triangular mesh.

Table 7.2: Error of H_2^T with Richardson extrapolation. With the Richardson extrapolation, we cannot obtain any improvement of the original error with the spherical triangular mesh. This might due to the refinement process of our spherical triangular mesh generation. Even though the number of spherical triangles become four times at the next step, the size of each triangle is not exactly one half of previous triangle.

T	$\ \rho_2^T - \rho\ _{L^\infty}$	$\ E^1 \rho_2^T - \rho\ _{L^\infty}$	$\ E^2 \rho_2^T - \rho\ _{L^\infty}$	$\ E^3 \rho_2^T - \rho\ _{L^\infty}$
20	8.8715e-01	-	-	-
80	2.0092e-01	2.0809e-01	-	-
320	3.9717e-02	4.1187e-02	4.1375e-02	-
1280	8.9674e-03	9.5300e-03	9.6075e-03	9.6173e-03

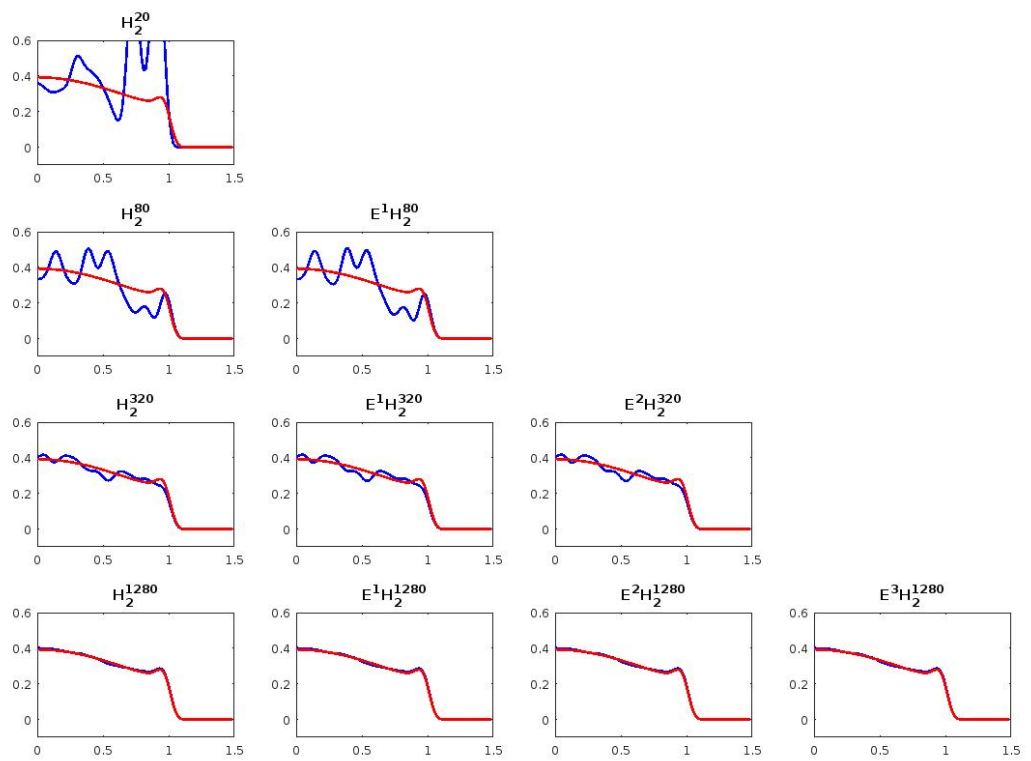


Figure 7.4: H_2^T solutions with Richardson extrapolation (cross-section along x-axis from center) with the original spherical triangular mesh.

CHAPTER 8. COLLIDED-UNCOLLIDED H_N^T APPROXIMATIONS

Recently, Crockatt and his co-workers have developed the hybrid methods for radiation transport [16, 17]. In this chapter, we study the hybrid collided-uncollided model approaches to solving RTE. We have not tested this method using H_N^T approximation, however, numerical implementation will be done in the near future.

The idea behind this method is decomposing the angular flux F in (2.6) into a collied part F_c and an uncollided part F_u with $F = F_u + F_c$ such that

$$F_{u,t} + \underline{\Omega} \cdot \nabla_r F_u + \sigma_t F_u = S, \quad (8.1)$$

$$F_{c,t} + \underline{\Omega} \cdot \nabla_r F_c + \sigma_t F_c = \frac{\sigma_s}{4\pi} \left(\int_{\mathbb{S}^2} F_u(\underline{r}, \underline{\Omega}, t) d\underline{\Omega} + \int_{\mathbb{S}^2} F_c(\underline{r}, \underline{\Omega}, t) d\underline{\Omega} \right). \quad (8.2)$$

Then they solved the each equation using discrete ordinate method with different order. In their paper, they used higher order of S_N method for uncollided equation. Since (8.1) is streaming dominated and (8.2) is scattering dominated, those two equations require different order of S_N for appropriate or desired accuracy.

In this chapter, we apply the same technique to our H_N^T method to solve (2.1) with $v = 1$ using (8.1) and (8.2).

First let the Cartesian coordinates of three vertices of k-th triangle be

$$\begin{aligned} \underline{x}_1^{(k)} &= (x_1^{(k)}, y_1^{(k)}, z_1^{(k)}), \\ \underline{x}_2^{(k)} &= (x_2^{(k)}, y_2^{(k)}, z_2^{(k)}), \\ \underline{x}_3^{(k)} &= (x_3^{(k)}, y_3^{(k)}, z_3^{(k)}). \end{aligned} \quad (8.3)$$

Also set the coordinate of a point inside a spherical triangle as

$$\underline{x}^{(k)} = (x^{(k)}, y^{(k)}, z^{(k)}), \quad (8.4)$$

and distance between the origin and the point as

$$r^{(k)} = \sqrt{\left(x^{(k)}\right)^2 + \left(y^{(k)}\right)^2 + \left(z^{(k)}\right)^2}. \quad (8.5)$$

Note that $r^{(k)} \neq 1$, since each triangle is not on the surface of a unit sphere \mathbb{S}^2 before projection onto \mathbb{S}^2 . Then we get a Jacobian,

$$J^{(k)}(\xi, \eta) = \frac{a^{(k)}x^{(k)}(\xi, \eta) + b^{(k)}y^{(k)}(\xi, \eta) + c^{(k)}z^{(k)}(\xi, \eta)}{\left(r^{(k)}(\xi, \eta)\right)^3}, \quad (8.6)$$

where $J^{(k)}(\xi, \eta)$ is the transformation from $(\xi, \eta) \in \mathbb{R}^2$ to points on \mathbb{S}^2 , and

$$\begin{aligned} a^{(k)} &= -y_2^{(k)}z_1^{(k)} + y_3^{(k)}z_1^{(k)} + y_1^{(k)}z_2^{(k)} - y_3^{(k)}z_2^{(k)} - y_1^{(k)}z_3^{(k)} + y_2^{(k)}z_3^{(k)}, \\ b^{(k)} &= x_2^{(k)}z_1^{(k)} - x_3^{(k)}z_1^{(k)} - x_1^{(k)}z_2^{(k)} + x_3^{(k)}z_2^{(k)} + x_1^{(k)}z_3^{(k)} - x_2^{(k)}z_3^{(k)}, \\ c^{(k)} &= -x_2^{(k)}y_1^{(k)} + x_3^{(k)}y_1^{(k)} + x_1^{(k)}y_2^{(k)} - x_3^{(k)}y_2^{(k)} - x_1^{(k)}y_3^{(k)} + x_2^{(k)}y_3^{(k)}. \end{aligned} \quad (8.7)$$

Now $\underline{x}^{(k)}$ can be expressed in terms of three vertices of a k-th triangle $\underline{x}_1^{(k)}, \underline{x}_2^{(k)}, \underline{x}_3^{(k)}$ and the center of the triangle $\underline{x}_c^{(k)}$:

$$\underline{x}^{(k)} = \underline{x}_c^{(k)} + \xi \left(\underline{x}_2^{(k)} - \underline{x}_1^{(k)} \right) + \eta \left(\underline{x}_3^{(k)} - \underline{x}_1^{(k)} \right), \quad (8.8)$$

where

$$\underline{x}_c^{(k)} = \frac{1}{3} \left(\underline{x}_1^{(k)} + \underline{x}_2^{(k)} + \underline{x}_3^{(k)} \right). \quad (8.9)$$

On the spherical spherical triangle $\mathcal{T}^{(k)} \subset \mathbb{S}^2$, we define a polynomial basis,

$\underline{\Psi}^{(k)}(\xi, \eta) : \mathbb{R}^2 \mapsto \mathbb{R}^M$, with the property that

$$\frac{1}{|\mathcal{T}^{(k)}|} \int_{-\frac{1}{3}}^{\frac{2}{3}} \int_{-\frac{1}{3}}^{\frac{1}{3}-\eta} \underline{\Psi}^{(k)} \underline{\Psi}^{(k)T} J^{(k)}(\xi, \eta) d\xi d\eta = \mathbb{I}, \quad (8.10)$$

where \mathbb{I} is an identity matrix. Now we can easily derive

$$\begin{aligned} F_{,t}^{(k)} &+ \frac{x^{(k)}(\xi, \eta)}{r^{(k)}(\xi, \eta)} F_{,x}^{(k)} + \frac{y^{(k)}(\xi, \eta)}{r^{(k)}(\xi, \eta)} F_{,y}^{(k)} + \frac{z^{(k)}(\xi, \eta)}{r^{(k)}(\xi, \eta)} F_{,z}^{(k)} + \sigma_t F^{(k)} \\ &= \frac{\sigma_s}{4\pi} \sum_{\mathcal{T}^{(k)} \subset \mathbb{S}^2} \frac{1}{|\mathcal{T}^{(k)}|} \int_{\mathcal{T}^{(k)}} F^{(k)}(x, y, z, \xi, \eta, t) J^{(k)}(\xi, \eta) d\xi d\eta + S^{(k)}, \end{aligned} \quad (8.11)$$

where $k = 1, 2, \dots, T$ with T is the number of spherical triangles.

From now on, we only consider two dimensional case. Decomposing (8.11) into uncollided and collided parts gives

$$F_{u,t}^{(k)} + \frac{x^{(k)}(\xi, \eta)}{r^{(k)}(\xi, \eta)} F_{u,x}^{(k)} + \frac{y^{(k)}(\xi, \eta)}{r^{(k)}(\xi, \eta)} F_{u,y}^{(k)} + \sigma_t F_u^{(k)} = S^{(k)}, \quad (8.12)$$

where $k = 1, 2, \dots, T_u$ with T_u is the number of spherical triangles for uncollided equation.

$$\begin{aligned} & F_{c,t}^{(k)} + \frac{x^{(k)}(\xi, \eta)}{r^{(k)}(\xi, \eta)} F_{c,x}^{(k)} + \frac{y^{(k)}(\xi, \eta)}{r^{(k)}(\xi, \eta)} F_{c,y}^{(k)} + \sigma_t F_c^{(k)} \\ &= \frac{\sigma_s}{4\pi} \sum_{k=1}^{T_u} \frac{1}{|\mathcal{T}_u^{(k)}|} \int_{-\frac{1}{3}}^{\frac{2}{3}} \int_{-\frac{1}{3}}^{\frac{1}{3}-\eta} F_u^{(k)}(x, y, \xi, \eta, t) J_u^{(k)}(\xi, \eta) d\xi d\eta \\ &+ \frac{\sigma_s}{4\pi} \sum_{k=1}^{T_c} \frac{1}{|\mathcal{T}_c^{(k)}|} \int_{-\frac{1}{3}}^{\frac{2}{3}} \int_{-\frac{1}{3}}^{\frac{1}{3}-\eta} F_c^{(k)}(x, y, \xi, \eta, t) J_c^{(k)}(\xi, \eta) d\xi d\eta. \end{aligned} \quad (8.13)$$

where $k = 1, 2, \dots, T_c$ with T_c is the number of spherical triangles for collided equation.

Define $F_u^{(k)}$ and $F_c^{(k)}$ as

$$F_u^{(k)} := \sum_{m=1}^{N_u} F_u^{(k)m}(x, y, t) \Psi_u^{(k)m}(\xi, \eta), \quad (8.14)$$

$$F_c^{(k)} := \sum_{m=1}^{N_c} F_c^{(k)m}(x, y, t) \Psi_c^{(k)m}(\xi, \eta) \quad (8.15)$$

where N_u and N_c are the number of basis functions $\Psi^{(k)m}(\xi, \eta)$ defined on a spherical triangle for uncollided and collided equations, respectively. Note that if the highest order of Ψ is n , then $N = n(n+1)/2$. Plug (8.14) and (8.15) into (8.12) and (8.13), and multiply both (8.12) and (8.13) by $\Psi_u^{(k)m'}$ and $\Psi_c^{(k)m'}$, respectively, then integrate over the corresponding spherical triangle to get two systems of equations:

$$\begin{aligned} & \frac{1}{|\mathcal{T}_u^{(k)}|} \int_{-\frac{1}{3}}^{\frac{2}{3}} \int_{-\frac{1}{3}}^{\frac{1}{3}-\eta} \sum_{m=1}^{N_u} F_{u,t}^{(k)m}(x, y, t) \Psi_u^{(k)m}(\xi, \eta) \Psi_u^{(k)m'}(\xi, \eta) J_u^{(k)}(\xi, \eta) d\xi d\eta \\ &+ \frac{1}{|\mathcal{T}_u^{(k)}|} \int_{-\frac{1}{3}}^{\frac{2}{3}} \int_{-\frac{1}{3}}^{\frac{1}{3}-\eta} \sum_{m=1}^{N_u} \frac{x^{(k)}(\xi, \eta)}{r^{(k)}(\xi, \eta)} F_{u,x}^{(k)m}(x, y, t) \Psi_u^{(k)m}(\xi, \eta) \Psi_u^{(k)m'}(\xi, \eta) J_u^{(k)}(\xi, \eta) d\xi d\eta \\ &+ \frac{1}{|\mathcal{T}_u^{(k)}|} \int_{-\frac{1}{3}}^{\frac{2}{3}} \int_{-\frac{1}{3}}^{\frac{1}{3}-\eta} \sum_{m=1}^{N_u} \frac{y^{(k)}(\xi, \eta)}{r^{(k)}(\xi, \eta)} F_{u,y}^{(k)m}(x, y, t) \Psi_u^{(k)m}(\xi, \eta) \Psi_u^{(k)m'}(\xi, \eta) J_u^{(k)}(\xi, \eta) d\xi d\eta \\ &+ \frac{\sigma_t}{|\mathcal{T}_u^{(k)}|} \int_{-\frac{1}{3}}^{\frac{2}{3}} \int_{-\frac{1}{3}}^{\frac{1}{3}-\eta} \sum_{m=1}^{N_u} F_u^{(k)m}(x, y, t) \Psi_u^{(k)m}(\xi, \eta) \Psi_u^{(k)m'}(\xi, \eta) J_u^{(k)}(\xi, \eta) d\xi d\eta \\ &= \frac{1}{|\mathcal{T}_u^{(k)}|} \int_{-\frac{1}{3}}^{\frac{2}{3}} \int_{-\frac{1}{3}}^{\frac{1}{3}-\eta} \sum_{m=1}^{N_u} S^{(k)}(x, y, t) \Psi_u^{(k)m}(\xi, \eta) \Psi_u^{(k)m'}(\xi, \eta) J_u^{(k)}(\xi, \eta) d\xi d\eta, \end{aligned} \quad (8.16)$$

for $k = 1, 2, \dots, T_u$, and

$$\begin{aligned}
& \frac{1}{|\mathcal{T}_c^{(k)}|} \int_{-\frac{1}{3}}^{\frac{2}{3}} \int_{-\frac{1}{3}}^{\frac{1}{3}-\eta} \sum_{m=1}^{N_c} F_{c,t}^{(k)m}(x, y, t) \Psi_c^{(k)m} \Psi_c^{(k)m'} J_c^{(k)} d\xi d\eta \\
& + \frac{1}{|\mathcal{T}_c^{(k)}|} \int_{-\frac{1}{3}}^{\frac{2}{3}} \int_{-\frac{1}{3}}^{\frac{1}{3}-\eta} \sum_{m=1}^{N_c} \frac{x^{(k)}(\xi, \eta)}{r^{(k)}(\xi, \eta)} F_{c,x}^{(k)m} \Psi_c^{(k)m}(\xi, \eta) \Psi_c^{(k)m'} J_c^{(k)} d\xi d\eta \\
& + \frac{1}{|\mathcal{T}_c^{(k)}|} \int_{-\frac{1}{3}}^{\frac{2}{3}} \int_{-\frac{1}{3}}^{\frac{1}{3}-\eta} \sum_{m=1}^{N_c} \frac{y^{(k)}(\xi, \eta)}{r^{(k)}(\xi, \eta)} F_{c,y}^{(k)m} \Psi_c^{(k)m} \Psi_c^{(k)m'} J_c^{(k)} d\xi d\eta \\
& + \frac{\sigma_t}{|\mathcal{T}_c^{(k)}|} \int_{-\frac{1}{3}}^{\frac{2}{3}} \int_{-\frac{1}{3}}^{\frac{1}{3}-\eta} \sum_{m=1}^{N_c} F_c^{(k)m} \Psi_c^{(k)m} \Psi_c^{(k)m'} J_c^{(k)} d\xi d\eta \\
& = \frac{\sigma_s}{4\pi} \sum_{k'=1}^{T_u} \left(\frac{1}{|\mathcal{T}_u^{(k')}|} \int_{-\frac{1}{3}}^{\frac{2}{3}} \int_{-\frac{1}{3}}^{\frac{1}{3}-\eta} \sum_{m=1}^{N_u} F_u^{(k')m} \Psi_u^{(k')m} J_u^{(k')} d\xi d\eta \right) \frac{1}{|\mathcal{T}_c^{(k)}|} \int_{-\frac{1}{3}}^{\frac{2}{3}} \int_{-\frac{1}{3}}^{\frac{1}{3}-\eta} \Psi_c^{(k)m'} J_c^{(k)} d\xi' d\eta' \\
& + \frac{\sigma_s}{4\pi} \sum_{k'=1}^{T_c} \left(\frac{1}{|\mathcal{T}_c^{(k')}|} \int_{-\frac{1}{3}}^{\frac{2}{3}} \int_{-\frac{1}{3}}^{\frac{1}{3}-\eta} \sum_{m=1}^{N_c} F_c^{(k')m} \Psi_c^{(k')m} J_c^{(k')} d\xi d\eta \right) \frac{1}{|\mathcal{T}_c^{(k)}|} \int_{-\frac{1}{3}}^{\frac{2}{3}} \int_{-\frac{1}{3}}^{\frac{1}{3}-\eta} \Psi_c^{(k)m'} J_c^{(k)} d\xi' d\eta',
\end{aligned} \tag{8.17}$$

for $k = 1, 2, \dots, T_c$.

For better representation of the system of equations:

$$F_{u,t} + \underline{\underline{A}_u}(e_1) F_{u,x} + \underline{\underline{A}_u}(e_2) F_{u,y} = -\sigma_t \underline{F}_u + \underline{S}, \tag{8.18}$$

$$F_{c,t} + \underline{\underline{A}_c}(e_1) F_{c,x} + \underline{\underline{A}_c}(e_2) F_{c,y} = -\sigma_t \underline{F}_c + \underline{B}, \tag{8.19}$$

where $e_1 = (1, 0)$, $e_2 = (0, 1)$, $\underline{\underline{A}_u}^k$ and $\underline{\underline{A}_c}^k$ are k -th blocks of block diagonal matrices $\underline{\underline{A}_u}$ and $\underline{\underline{A}_c}$, respectively,

$$\underline{\underline{A}_u}^{(k)}(\hat{n}) = \frac{1}{|\mathcal{T}_u^{(k)}|} \int_{-\frac{1}{3}}^{\frac{2}{3}} \int_{-\frac{1}{3}}^{\frac{1}{3}-\eta} (\hat{n} \cdot \underline{v}) \underline{\Psi}_u^{(k)} \underline{\Psi}_u^{(k)T} J_u^{(k)}(\xi, \eta) d\xi d\eta, \tag{8.20}$$

$$\underline{\underline{A}_c}^{(k)}(\hat{n}) = \frac{1}{|\mathcal{T}_c^{(k)}|} \int_{-\frac{1}{3}}^{\frac{2}{3}} \int_{-\frac{1}{3}}^{\frac{1}{3}-\eta} (\hat{n} \cdot \underline{v}) \underline{\Psi}_c^{(k)} \underline{\Psi}_c^{(k)T} J_c^{(k)}(\xi, \eta) d\xi d\eta, \tag{8.21}$$

$$\underline{v} = \left[\frac{x^{(k)}(\xi, \eta)}{r^{(k)}(\xi, \eta)}, \frac{y^{(k)}(\xi, \eta)}{r^{(k)}(\xi, \eta)} \right]^T, \tag{8.22}$$

$$\underline{\underline{A}_u} = \begin{bmatrix} \underline{\underline{A}_u}^{(1)} & & & \\ & \underline{\underline{A}_u}^{(2)} & & \\ & & \underline{\underline{A}_u}^{(3)} & \\ & & & \ddots \\ & & & & \underline{\underline{A}_u}^{(T_u)} \end{bmatrix}, \quad \underline{\underline{A}_c} = \begin{bmatrix} \underline{\underline{A}_c}^{(1)} & & & \\ & \underline{\underline{A}_c}^{(2)} & & \\ & & \underline{\underline{A}_c}^{(3)} & \\ & & & \ddots \\ & & & & \underline{\underline{A}_c}^{(T_c)} \end{bmatrix}.$$

And since

$$F_u^{(k)}(x, y, \xi, \eta, t) = \sum_{m=1}^{N_u} F_u^{(k)m}(x, y, t) \Psi_u^{(k)m}(\xi, \eta) = \underline{\Psi}_u^{(k)T} \underline{F}_u^{(k)}, \quad (8.23)$$

$$F_c^{(k)}(x, y, \xi, \eta, t) = \sum_{m=1}^{N_b} F_c^{(k)m}(x, y, t) \Psi_c^{(k)m}(\xi, \eta) = \underline{\Psi}_c^{(k)T} \underline{F}_c^{(k)}, \quad (8.24)$$

we have vectors \underline{F}_u and \underline{F}_c as follow:

$$\underline{F}_u = \begin{bmatrix} \underline{F}_u^{(1)} \\ \underline{F}_u^{(2)} \\ \underline{F}_u^{(3)} \\ \vdots \\ \underline{F}_u^{(T_u)} \end{bmatrix}, \quad \underline{F}_c = \begin{bmatrix} \underline{F}_c^{(1)} \\ \underline{F}_c^{(2)} \\ \underline{F}_c^{(3)} \\ \vdots \\ \underline{F}_c^{(T_c)} \end{bmatrix}.$$

Also, \underline{B} in the equation (8.19) is

$$\underline{B} = \frac{\sigma_s}{4\pi} \left(\sum_{k=1}^{T_u} \underline{F}_u^{(k)1} + \sum_{k'=1}^{T_c} \underline{F}_c^{(k')1} \right) \underline{w} \quad (8.25)$$

where \underline{w} is a sparse vector:

$$\underline{w} = \left\{ \begin{bmatrix} \underline{c} \\ \underline{c} \\ \underline{c} \\ \vdots \\ \underline{c} \end{bmatrix} \right\} N_c \times T_c \text{ rows}, \quad \underline{c} = \left\{ \begin{bmatrix} 1 \\ 0 \\ 0 \\ \vdots \\ 0 \end{bmatrix} \right\} N_c \text{ rows}$$

with T_c is the number of triangular elements on the unit sphere \mathbb{S}^2 , and N_c is the number of basis functions for each triangle, both for collided equation.

CHAPTER 9. BLENDED P_N AND H_N^T SCHEMES

Our goal in this chapter is improving H_N^T methods by hybridizing the method and the P_N approximation to obtain desirable aspects of P_N approach, e.g. rotational invariance.

9.1 Derivation

In this chapter, we introduce the real form of spherical harmonics R_ℓ^m from [37], instead of the complex form of spherical harmonics Y_ℓ^m as before. The real form of spherical harmonics has a form of

$$R_\ell^m(\underline{\Omega}) = \begin{cases} \sqrt{2} C_\ell^m P_\ell^m(\mu) \cos(m\varphi), & \text{if } 0 < m \leq \ell \leq N, \\ C_\ell^0 P_\ell^0(\mu), & \text{if } 0 \leq \ell \leq N, \\ \sqrt{2} C_\ell^{|m|} P_\ell^{|m|}(\mu) \sin(|m|\varphi), & \text{if } 0 < -m \leq \ell \leq N, \end{cases} \quad (9.1)$$

with

$$C_\ell^m = \sqrt{\frac{(2\ell+1)(\ell-m)!}{4\pi(\ell+m)!}}. \quad (9.2)$$

This changes the spherical harmonics expansion and the number of moments we used in Chapter 2. Therefore we have to set up P_N equations again using the real form of the spherical harmonics R_ℓ^m . Flux Jacobians can be found in [43]. We need only P_1 and P_3 equations here. The P_1 Jacobians are as follow:

$$\underline{\underline{A}} = \left[\begin{array}{c|ccc} 0 & 0 & 0 & \frac{1}{\sqrt{2}} f_1^1 \\ \hline 0 & 0 & 0 & 0 \\ 0 & 0 & 0 & 0 \\ \frac{1}{\sqrt{2}} f_1^1 & 0 & 0 & 0 \end{array} \right],$$

$$\underline{\underline{B}} = \left[\begin{array}{c|ccc} 0 & \frac{1}{\sqrt{2}} f_1^1 & 0 & 0 \\ \hline \frac{1}{\sqrt{2}} f_1^1 & 0 & 0 & 0 \\ 0 & 0 & 0 & 0 \\ 0 & 0 & 0 & 0 \end{array} \right],$$

and P_3 Jacobians are

$$\underline{\underline{A}} = \left[\begin{array}{c|cc|ccccc} 0 & 0 & 0 & \frac{1}{\sqrt{2}} f_1^1 & 0 & 0 & 0 & 0 & 0 \\ \hline 0 & 0 & 0 & 0 & \frac{1}{2} f_2^2 & 0 & 0 & 0 & 0 \\ 0 & 0 & 0 & 0 & 0 & 0 & 0 & \frac{1}{\sqrt{2}} f_2^1 & 0 \\ \frac{1}{\sqrt{2}} f_1^1 & 0 & 0 & 0 & 0 & 0 & -\frac{1}{\sqrt{2}} d_2^0 & 0 & \frac{1}{2} f_2^2 \\ \hline 0 & \frac{1}{2} f_2^2 & 0 & 0 & 0 & 0 & 0 & 0 & 0 \\ 0 & 0 & 0 & 0 & 0 & 0 & 0 & 0 & 0 \\ 0 & 0 & 0 & -\frac{1}{\sqrt{2}} d_2^0 & 0 & 0 & 0 & 0 & 0 \\ 0 & 0 & \frac{1}{\sqrt{2}} f_2^1 & 0 & 0 & 0 & 0 & 0 & 0 \\ 0 & 0 & 0 & \frac{1}{2} f_2^2 & 0 & 0 & 0 & 0 & 0 \end{array} \right],$$

and

$$\underline{\underline{B}} = \left[\begin{array}{c|cc|ccccc} 0 & \frac{1}{\sqrt{2}} f_1^1 & 0 & 0 & 0 & 0 & 0 & 0 & 0 \\ \hline \frac{1}{\sqrt{2}} f_1^1 & 0 & 0 & 0 & 0 & 0 & -\frac{1}{\sqrt{2}} d_2^0 & 0 & -\frac{1}{2} f_2^2 \\ 0 & 0 & 0 & 0 & 0 & \frac{1}{\sqrt{2}} f_2^1 & 0 & 0 & 0 \\ 0 & 0 & 0 & 0 & \frac{1}{2} f_2^2 & 0 & 0 & 0 & 0 \\ \hline 0 & 0 & 0 & \frac{1}{2} f_2^2 & 0 & 0 & 0 & 0 & 0 \\ 0 & 0 & \frac{1}{\sqrt{2}} f_2^1 & 0 & 0 & 0 & 0 & 0 & 0 \\ 0 & -\frac{1}{\sqrt{2}} d_2^0 & 0 & 0 & 0 & 0 & 0 & 0 & 0 \\ 0 & 0 & 0 & 0 & 0 & 0 & 0 & 0 & 0 \\ 0 & -\frac{1}{2} f_2^2 & 0 & 0 & 0 & 0 & 0 & 0 & 0 \end{array} \right],$$

where

$$f_\ell^k = \sqrt{\frac{(\ell+k)(\ell+k-1)}{(2\ell+1)(2\ell-1)}}, \quad (9.3)$$

and

$$d_\ell^k = \sqrt{\frac{(\ell-k)(\ell-k-1)}{(2\ell+1)(2\ell-1)}}. \quad (9.4)$$

Then we get the following P_1 equations and P_3 equations. The P_1 equations are as follow:

$$\begin{bmatrix} F_0^0 \\ F_1^{-1} \\ F_1^0 \\ F_1^1 \end{bmatrix}_{,t} + \begin{bmatrix} \frac{1}{\sqrt{3}} F_1^1 \\ 0 \\ 0 \\ \frac{1}{\sqrt{3}} F_0^0 \end{bmatrix}_{,x} + \begin{bmatrix} \frac{1}{\sqrt{3}} F_1^{-1} \\ \frac{1}{\sqrt{3}} F_0^0 \\ 0 \\ 0 \end{bmatrix}_{,y} = \begin{bmatrix} (\sigma_s - \sigma_t) F_0^0 \\ -\sigma_t F_1^{-1} \\ -\sigma_t F_1^0 \\ -\sigma_t F_1^1 \end{bmatrix}. \quad (9.5)$$

If we choose three moments F_0^0, F_1^{-1}, F_1^0 , and F_1^1 from P_3 equations, then we can get

$$\begin{bmatrix} F_0^0 \\ F_1^{-1} \\ F_1^0 \\ F_1^1 \end{bmatrix}_{,t} + \begin{bmatrix} \frac{1}{\sqrt{3}} F_1^1 \\ \frac{1}{\sqrt{5}} F_2^{-2} \\ \frac{1}{\sqrt{5}} F_2^1 \\ \frac{1}{\sqrt{3}} F_0^0 - \frac{1}{\sqrt{15}} F_2^0 + \frac{1}{\sqrt{5}} F_2^2 \end{bmatrix}_{,x} + \begin{bmatrix} \frac{1}{\sqrt{3}} F_1^{-1} \\ \frac{1}{\sqrt{3}} F_0^0 - \frac{1}{\sqrt{15}} F_2^0 - \frac{1}{\sqrt{5}} F_2^2 \\ \frac{1}{\sqrt{5}} F_2^{-1} \\ \frac{1}{\sqrt{5}} F_2^{-2} \end{bmatrix}_{,y} = \begin{bmatrix} (\sigma_s - \sigma_t) F_0^0 \\ -\sigma_t F_1^{-1} \\ -\sigma_t F_1^0 \\ -\sigma_t F_1^1 \end{bmatrix}. \quad (9.6)$$

In each stage of the Runge-Kutta time-stepping procedure, we consider two distinct models that communicate through various moments. For the first model we consider the P_1 approximation, but with missing moments, which are highlighted in red, supplied by the H_N^T approximation:

$$\begin{bmatrix} F_0^0 \\ F_1^{-1} \\ F_1^0 \\ F_1^1 \end{bmatrix}_{,t} + \begin{bmatrix} \frac{1}{\sqrt{3}} F_1^1 \\ \frac{1}{\sqrt{5}} F_2^{-2} \\ \frac{1}{\sqrt{5}} F_2^1 \\ \frac{1}{\sqrt{3}} F_0^0 - \frac{1}{\sqrt{15}} F_2^0 + \frac{1}{\sqrt{5}} F_2^2 \end{bmatrix}_{,x} + \begin{bmatrix} \frac{1}{\sqrt{3}} F_1^{-1} \\ \frac{1}{\sqrt{3}} F_0^0 - \frac{1}{\sqrt{15}} F_2^0 - \frac{1}{\sqrt{5}} F_2^2 \\ \frac{1}{\sqrt{5}} F_2^{-1} \\ \frac{1}{\sqrt{5}} F_2^{-2} \end{bmatrix}_{,y} = \begin{bmatrix} (\sigma_s - \sigma_t) F_0^0 \\ -\sigma_t F_1^{-1} \\ -\sigma_t F_1^0 \\ -\sigma_t F_1^1 \end{bmatrix}. \quad (9.7)$$

The second model is the H_N^T model, but with the density provided from the P_N model, which we again highlight in red:

$$F_{,t} + \underline{\Omega} \cdot \nabla_r F = -\sigma_t F + \sigma_s \rho. \quad (9.8)$$

The moments F_ℓ^m can be calculated by the formula

$$F_\ell^m(x, y, t) = \int_{\mathbb{S}^2} F(x, y, \underline{\Omega}, t) R_\ell^m(\underline{\Omega}) d\underline{\Omega}, \quad (9.9)$$

where R_ℓ^m is defined in (9.1). We need five real spherical harmonics:

$$\begin{aligned} R_2^{-2}(\mu, \varphi) &= \sqrt{\frac{15}{16\pi}}(1 - \mu^2) \sin 2\varphi, \\ R_2^{-1}(\mu, \varphi) &= -\sqrt{\frac{15}{4\pi}}\mu\sqrt{1 - \mu^2} \sin \varphi, \\ R_2^0(\mu, \varphi) &= \sqrt{\frac{5}{16\pi}}(3\mu^2 - 1), \\ R_2^1(\mu, \varphi) &= -\sqrt{\frac{15}{4\pi}}\mu\sqrt{1 - \mu^2} \cos \varphi, \\ R_2^2(\mu, \varphi) &= \sqrt{\frac{15}{16\pi}}(1 - \mu^2) \cos 2\varphi. \end{aligned} \quad (9.10)$$

The solution $F(x, y, \underline{\Omega}, t)$ in the k -th triangle can be express as

$$F(x, y, \mu, \varphi, t) \Big|_{\mathcal{T}^{(k)}} = F^{(k)}(x, y, \xi, \eta, t) = F(x, y, \mu^{(k)}(\xi, \eta), \varphi^{(k)}(\xi, \eta), t), \quad (9.11)$$

where

$$\mu^{(k)}(\xi, \eta) = \frac{z^{(k)}(\xi, \eta)}{r^{(k)}(\xi, \eta)}, \quad (9.12)$$

and

$$\varphi^{(k)}(\xi, \eta) = \arctan \left(\frac{y^{(k)}(\xi, \eta)}{x^{(k)}(\xi, \eta)} \right). \quad (9.13)$$

Hence (9.9) becomes

$$\begin{aligned} F_\ell^m(x, y, t) &= \int_{\mathbb{S}^2} F(x, y, \underline{\Omega}, t) Y_\ell^m(\underline{\Omega}) d\underline{\Omega} \\ &= \sum_{k=1}^T \frac{1}{|\mathcal{T}^{(k)}|} \int_{-\frac{1}{3}}^{\frac{2}{3}} \int_{-\frac{1}{3}}^{\frac{1}{3}-\eta} \sum_{n=1}^N F^{(k)n} \Psi^{(k)n}(\xi, \eta) J^{(k)}(\xi, \eta) R_\ell^{m(k)}(\xi, \eta) d\xi d\eta, \end{aligned} \quad (9.14)$$

where

$$R_\ell^{m(k)}(\xi, \eta) = R_\ell^m(\mu, \varphi) \Big|_{\mathcal{T}^{(k)}} = R_\ell^m(\mu^{(k)}(\xi, \eta), \varphi^{(k)}(\xi, \eta)). \quad (9.15)$$

Therefore, five moments $F_2^{-2}, F_2^{-1}, F_2^0, F_2^1$ and F_2^2 are given by

$$\begin{aligned}
F_2^{-2} &= \sum_{k=1}^T \frac{1}{|\mathcal{T}^{(k)}|} \int_{-\frac{1}{3}}^{\frac{2}{3}} \int_{-\frac{1}{3}}^{\frac{1}{3}-\eta} \sum_{n=1}^N F^{(k)n} \Psi^{(k)n} J^{(k)} R_2^{-2(k)}(\xi, \eta) d\xi d\eta, \\
&= \sqrt{\frac{15}{16\pi}} \sum_{k=1}^T \frac{1}{|\mathcal{T}^{(k)}|} \int_{-\frac{1}{3}}^{\frac{2}{3}} \int_{-\frac{1}{3}}^{\frac{1}{3}-\eta} \sum_{n=1}^N F^{(k)n} \Psi^{(k)n} J^{(k)} \left(1 - (\mu^{(k)})^2\right) \sin 2\varphi^{(k)} d\xi d\eta. \\
F_2^{-1} &= \sum_{k=1}^T \frac{1}{|\mathcal{T}^{(k)}|} \int_{-\frac{1}{3}}^{\frac{2}{3}} \int_{-\frac{1}{3}}^{\frac{1}{3}-\eta} \sum_{n=1}^N F^{(k)n} \Psi^{(k)n} J^{(k)} R_2^{-1(k)}(\xi, \eta) d\xi d\eta, \\
&= -\sqrt{\frac{15}{4\pi}} \sum_{k=1}^T \frac{1}{|\mathcal{T}^{(k)}|} \int_{-\frac{1}{3}}^{\frac{2}{3}} \int_{-\frac{1}{3}}^{\frac{1}{3}-\eta} \sum_{n=1}^N F^{(k)n} \Psi^{(k)n} J^{(k)} \mu^{(k)} \sqrt{1 - (\mu^{(k)})^2} \sin \varphi^{(k)} d\xi d\eta, \\
F_2^0 &= \sum_{k=1}^T \frac{1}{|\mathcal{T}^{(k)}|} \int_{-\frac{1}{3}}^{\frac{2}{3}} \int_{-\frac{1}{3}}^{\frac{1}{3}-\eta} \sum_{n=1}^N F^{(k)n} \Psi^{(k)n} J^{(k)} R_2^{0(k)}(\xi, \eta) d\xi d\eta, \\
&= \sqrt{\frac{5}{16\pi}} \sum_{k=1}^T \frac{1}{|\mathcal{T}^{(k)}|} \int_{-\frac{1}{3}}^{\frac{2}{3}} \int_{-\frac{1}{3}}^{\frac{1}{3}-\eta} \sum_{n=1}^N F^{(k)n} \Psi^{(k)n} J^{(k)} \left(3(\mu^{(k)})^2 - 1\right) d\xi d\eta, \\
F_2^1 &= \sum_{k=1}^T \frac{1}{|\mathcal{T}^{(k)}|} \int_{-\frac{1}{3}}^{\frac{2}{3}} \int_{-\frac{1}{3}}^{\frac{1}{3}-\eta} \sum_{n=1}^N F^{(k)n} \Psi^{(k)n} J^{(k)} R_2^{1(k)}(\xi, \eta) d\xi d\eta, \\
&= -\sqrt{\frac{15}{4\pi}} \sum_{k=1}^T \frac{1}{|\mathcal{T}^{(k)}|} \int_{-\frac{1}{3}}^{\frac{2}{3}} \int_{-\frac{1}{3}}^{\frac{1}{3}-\eta} \sum_{n=1}^N F^{(k)n} \Psi^{(k)n} J^{(k)} \mu^{(k)} \sqrt{1 - (\mu^{(k)})^2} \cos \varphi^{(k)} d\xi d\eta,
\end{aligned}$$

and

$$\begin{aligned}
F_2^2 &= \sum_{k=1}^T \frac{1}{|\mathcal{T}^{(k)}|} \int_{-\frac{1}{3}}^{\frac{2}{3}} \int_{-\frac{1}{3}}^{\frac{1}{3}-\eta} \sum_{n=1}^N F^{(k)n} \Psi^{(k)n} J^{(k)} R_2^{2(k)}(\xi, \eta) d\xi d\eta, \\
&= \sqrt{\frac{15}{16\pi}} \sum_{k=1}^T \frac{1}{|\mathcal{T}^{(k)}|} \int_{-\frac{1}{3}}^{\frac{2}{3}} \int_{-\frac{1}{3}}^{\frac{1}{3}-\eta} \sum_{n=1}^N F^{(k)n} \Psi^{(k)n} J^{(k)} \left(1 - (\mu^{(k)})^2\right) \cos 2\varphi^{(k)} d\xi d\eta.
\end{aligned} \tag{9.16}$$

The algorithm is as follow:

1. Solve the equation (9.8) and (9.7) simultaneously with the initial density $\rho^{(n)}$.
2. In each stage of the Runge-Kutta time-stepping procedure, $F_2^{-2}, F_2^{-1}, F_2^0, F_2^1$ and F_2^2 are calculated by the equations (9.16).
3. Five moments obtained from the second step are used to find new density ρ or F_0^0 , instead of collecting H_N^T moments.

4. Repeat the process.

9.2 Numerical Results

Numerical tests for the blended P_N and H_N^T scheme have been done. The solution is supposed to converge to the exact solution, however, in this test we did not get the convergent solutions. We might need to examine our codes thoroughly and test the method again in the near future.

CHAPTER 10. CONCLUSION AND FUTURE WORK

We have developed the H_N^T approximations by combining of the ideas of the P_N and S_N methods. Both methods converge to the exact solution in different ways. However, when the degrees of freedom of both methods are small, we can see that the H_N^T methods perform better than P_N due to the high oscillation of P_N approximations. One of the undesirable aspects of P_N approximations is the difficulty of the implementation of boundary conditions. H_N^T methods can also behave better when it comes to the boundary conditions by using the octantal-spherical-triangular mesh. However, our H_N^T schemes are not free from the ray effect seen in discrete ordinates methods, although we can reduce the ray effect by increasing the number of triangular elements T or the order of the polynomial basis for the elements $N - 1$. We also explored several generalizations of this idea that could be used to improve the simulation accuracy, including Richardson extrapolation, collided-uncollided decompositions, and blended P_N - H_N^T schemes. In future work, we will work on extending the 1D positivity limiters for the multi-dimensional H_N^T method to guarantee positive particle concentrations. Also, we would like to provide the comparison of the efficiency of this method and other methods including P_N and S_N methods. We have solved the line source problem and lattice problem in our work, however, we hope to be able to solve other famous benchmark problems including the hohlraum problem [7]. In addition, multi-energy groups and frequency will be added to solve practical problems, such as those of interest in nuclear reactors and astrophysical applications. We will keep working on the collided-uncollided H_N^T method to see the numerical results. Blended P_N and H_N^T scheme will be done in the very near future. Also, in order to improve numerical efficiency, implicit time stepping should be used in our scheme. Due to the size of the problem, parallelization of our scheme is also necessary to reduce the computational cost.

BIBLIOGRAPHY

- [1] M. Abramowitz. *Handbook of Mathematical Functions: with Formulas, Graphs, and Mathematical Tables*. Dover Publications, Inc., New York, NY, USA, 1974.
- [2] M. L. Adams and E. W. Larsen. Fast iterative methods for discrete-ordinates particle transport calculations. *Progress in Nuclear Energy*, 40(1):3–159, 2002.
- [3] R. Alexander. Diagonally implicit Runge-Kutta methods for stiff O.D.E.’s. *SIAM J. Numer. Anal.*, 14(6):1006–1021, 1977.
- [4] G. Arfken. *Mathematical Methods for Physicists, 3rd ed.* Academic Press, Orlando, FL, 1985.
- [5] D. Balsara. Fast and accurate discrete ordinates methods for multidimensional radiative transfer. Part I, basic methods. *Journal of Quantitative Spectroscopy and Radiative Transfer*, 69:671–707, 2001.
- [6] T. A. Brunner. *Riemann solvers for time-dependent transport based on the maximum entropy and spherical harmonics closures*. PhD thesis, University of Michigan, Ann Arbor, Michigan, 2000.
- [7] T. A. Brunner. *Forms of approximate radiation transport*. Tech. Rep. SAND2002-1778, Sandia National Laboratories, 2002.
- [8] T. A. Brunner and J. P. Holloway. Two-dimensional time-dependent Riemann solvers for neutron transport. *J. Comput. Phys.*, 210(1):386–399, 2005.

- [9] T. Camminady, M. Frank, K. Kupper, and J. Kusch. Ray effect mitigation for the discrete ordinates method through quadrature rotation. *arXiv:1808.05846 [math.NA]*, 2018.
- [10] J. C. Chai, HaeOk S. Lee, and Suhas V. Patankar. Ray effect and false scattering in the discrete ordinates method. *Numerical Heat Transfer, Part B: Fundamentals*, 24(4):373–389, 1993.
- [11] B. Cockburn, S. Hou, and C.-W. Shu. TVB Runge-Kutta local projection discontinuous Galerkin finite element method for conservation laws IV: The multidimensional case. *Math. Comp.*, 54(545), 1990.
- [12] B. Cockburn, S. Y. Lin, and C.-W. Shu. TVB Runge-Kutta local projection discontinuous Galerkin finite element method for conservation laws III: One dimensional systems. *J. Comput. Phys.*, 84(90), 1989.
- [13] B. Cockburn and C.-W. Shu. TVB Runge-Kutta local projection discontinuous Galerkin finite element method for scalar conservation laws II: General framework. *Math. Comp.*, 52:411–435, 1989.
- [14] B. Cockburn and C.-W. Shu. The Runge-Kutta local projection P^1 -discontinuous-Galerkin finite element method for scalar conservation laws. *RAIRO Model. Math. Anal. Numer.*, 25(3):337–361, 1991.
- [15] B. Cockburn and C.-W. Shu. The Runge-Kutta discontinuous Galerkin method for conservation laws V: Multidimensional systems. *J. Comput. Phys.*, 141:199–224, 1998.
- [16] M. M. Crockatt, A. J. Christlieb, C. K. Garrett, and C. D. Hauck. An arbitrary-order, fully implicit, hybrid kinetic solver for linear radiative transport using integral deferred correction. *J. Comput. Phys.*, 346(1):212–241, 2017.

- [17] M. M. Crockatt, A. J. Christlieb, C. K. Garrett, and C. D. Hauck. Hybrid methods for radiation transport using diagonally implicit Runge-Kutta and space-time discontinuous Galerkin time integration. *J. Comput. Phys.*, 376:455–477, 2019.
- [18] S.F. Davis. Tvd finite difference scheme and artificial viscosity. *ICASE Report 84-20*, 1984.
- [19] T. Endo and A. Yamamoto. Development of new solid angle quadrature sets to satisfy even- and odd-moment conditions. *Journal of Nuclear Science and Technology*, 44(10):1249–1258, 2012.
- [20] W.A. Fiveland. The selection of discrete ordinate quadrature sets for anisotropic scattering. *Fundamentals of Radiation Heat Transfer*, 160, 1991.
- [21] J. A. Fleck, Jr., and J. D. Cummings. An implicit Monte Carlo scheme for calculating time and frequency dependent nonlinear radiation transport. *J. Comput. Phys.*, 8(3):313–342, 1971.
- [22] B. D. Ganapol, C. T. Kelley, and G. C. Pomraning. Asymptotically exact boundary conditions for the P_N equations. *Nucl. Sci. Eng.*, 114:12–19, 1993.
- [23] J. Goncalves and P. J. Coelho. Parallelization of the discrete ordinates method. *Numerical Heat Transfer, Part B: Fundamentals*, 32(2):151–173, 1997.
- [24] S. Gottlieb, C.-W. Shu, and E. Tadmor. Strong stability-preserving high-order time discretization methods. *SIAM Review*, 43(1):89–112, 2001.
- [25] E. Hairer and G. Wanner. *Solving Ordinary Differential Equations II: Stiff and Differential-Algebraic Problems (second edition)*, volume 14. Springer Series in Computational Mathematics, Springer-Verlag, Berlin, Heidelberg, 1996.

- [26] A. Harten and P.D. Lax. A random choice finite difference scheme for hyperbolic conservation laws. *SIAM J. Numer. Anal.*, 18:289–315, 1981.
- [27] C. D. Hauck and R. G. McClarren. Positive P_N closures. *SIAM J. Sci. Comput.*, 32(5):2603–2626, 2010.
- [28] J. S. Hesthaven. DG-FEM for PDEs, <http://www.cfm.brown.edu/people/jansh/resources/Publications/Lectures/USC10-1.pdf>. *RMMC, lecture notes*, 2008.
- [29] F. B. Hildebrand. *Introduction to Numerical Analysis*. McGraw-Hill, New York, 1956.
- [30] B. Hunter and Z. Guo. Comparison of quadrature schemes in DOM for anisotropic scattering radiative transfer analysis. *Numerical Heat Transfer, Part B: Fundamentals*, 63(6):485–507, 2013.
- [31] H. Iwabuchi. Efficient Monte Carlo methods for radiative transfer modeling. *Journal of the Atmospheric Sciences*, 63(9):2324–2339, 2006.
- [32] J.J. Jarrell and M.L. Adams. Discrete-ordinates quadrature sets based on linear discontinuous finite elements. In *Proc. International Conference on Mathematics and Computational Methods applied to Nuclear Science and Engineering, Rio de Janeiro, Brazil*, 2011.
- [33] Y. Jiang and H. Liu. Invariant-region-preserving DG methods for multi-dimensional hyperbolic conservation law systems, with an application to compressible Euler equations. *J. Comput. Phys.*, 373:385–409, 2018.
- [34] C. A. Kennedy and M. H. Carpenter. Diagonally implicit Runge-Kutta methods for ordinary differential equations. A review. *NASA technical memorandum*, NASA/TM-2016-219173, 2016.

- [35] D. I. Ketcheson. Highly efficient strong stability-preserving Runge-Kutta methods with low-storage implementations. *SIAM J. on Scientific Computing*, 30(4):2113–2136, 2008.
- [36] G. Krishnamoorthy, R. Rawat, and P. J. Smith. Parallel computations of radiative heat transfer using the discrete ordinates method. *Numerical Heat Transfer, Part B*, 46:19–38, 2005.
- [37] V. M. Laboure, R. G. McClarren, and C. D. Hauck. Implicit Filtered P_N for high-energy density thermal radiation transport using discontinuous Galerkin finite elements. *J. Comput. Phys.*, 321:624–643, 2016.
- [38] E. W. Larsen and J. E. Morel. Advances in discrete-ordinates methodology. *Springer*, 2010.
- [39] E. W. Larsen and G. C. Pomraning. The P_N theory as an asymptotic limit of transport theory in planar geometry I: Analysis. *Nucl. Sci. Eng.*, 109:49–75, 1991.
- [40] R. J. LeVeque. *Finite Volume Methods for Hyperbolic Problems*. Cambridge University Press, 2002.
- [41] C. D. Levermore. Boundary conditions for moment closures. *Presented at Institute for Pure and Applied Mathematics University of California, Los Angeles, CA*, 2009.
- [42] E. E. Lewis and W. F. Miller. *Computational Methods of Neutron Transport*. John Wiley & Sons, DeKalb, 1994.
- [43] M. Frank and C. Hauck and K. Kupper. Convergence of filtered spherical harmonic equations for radiation transport. *Communications in Mathematical Sciences*, 14:1443–1465, 2016.

- [44] R. G. McClaren. Spherical harmonics methods for thermal radiation transport. *Ph.D. thesis, The University of Michigan, Nuclear Engineering and Radiological Sciences*, 2006.
- [45] M. F. Modest. *Radiative Heat Transfer, 2nd ed.* Academic Press, Newyork, 2003.
- [46] S. Osher. Numerical solution of singular perturbation problems and hyperbolic systems of conservation laws. *Math. Studies No. 47 (O. Axelsson, L. S. Frank, A. van der Sluis, Eds.)*, North-Holland, Amsterdam, pages 179–205, 1981.
- [47] T. M. Pandya, S. R. Johnson, T. M. Evans, G. G. Davidson, S. P. Hamilton, and A. T. Godfrey. Implementation, capabilities, and benchmarking of Shift, a massively parallel Monte Carlo radiation transport code. *J. Comput. Phys.*, 308:239–272, 2016.
- [48] G. C. Pomraning. Variational boundary conditions for the spherical harmonics approximation to the neutron transport equation. *Ann. Phys.*, 27:193–215, 1964.
- [49] A. Prothero and A. Robinson. On the stability and accuracy of one-step methods for solving stiff systems of ordinary differential equations. *Math. Comp.*, 28(125):145–162, 1974.
- [50] A. Quarteroni, R. Sacco, and F. Saleri. *Numerical Mathematics*, volume 37. Texts in Applied Mathematics, Springer, New York, 2001.
- [51] W.H. Reed and T.R. Hill. Triangular mesh methods for the neutron transport equation. *Technical Report LA-UR-73-479, Los Alamos Scientific Laboratory*, 1973.
- [52] P.L. Roe. The use of the Riemann problem in finite difference schemes. *Lecture Notes in Physics*, 141:354–359, 1981.
- [53] V.V. Rusanov. Computation of interaction of nonstationary shocks with obstacles. *Zh. Vych. Matem. Mat. Fiz.* 1121, pages 267–279, 1961.

- [54] C.-W. Shu. Total-variation-diminishing time discretizations. *SIAM J. Sci. Stat. Comput.*, 9(6):1073–1084, 1988.
- [55] C.-W. Shu and S. Osher. Efficient implementation of essentially non-oscillatory shock-capturing schemes. *J. Comput. Phys.*, 77:439–471, 1988.
- [56] B. van Leer. Flux-vector splitting for the Euler equations. *Lecture Notes in Physics*, 170:507–512, 1982.
- [57] B. van Leer, J. L. Thomas, P. Roe, and R. W. Newsome. A comparison of numerical flux formulas for the Euler and Navier-Stokes equations. *AIAA-paper 87-1104*, 1987.
- [58] P. R. Wallace. *Mathematical Analysis of Physical Problems*. Dover Publications Inc., 1972.
- [59] H. Yee. Construction of explicit and implicit symmetric TVD schemes and their applications. *J. Comput. Phys.*, pages 151–179, 1987.
- [60] X. Zhang. *Maximum-principle-satisfying and positivity-preserving high order schemes for conservation laws*. PhD thesis, Brown University, 2011.
- [61] X. Zhang and C.-W. Shu. On maximum-principle-satisfying high order schemes for scalar conservation laws. *J. Comput. Phys.*, 229(9):3091–3120, 2010.
- [62] X. Zhang and C.-W. Shu. On positivity-preserving high order discontinuous Galerkin schemes for compressible Euler equations on rectangular meshes. *Comput. Phys.*, 229(23):8918–8934, 2010.
- [63] X. Zhang and C.-W. Shu. Positivity-preserving high order discontinuous Galerkin schemes for compressible Euler equations with source terms. *J. Comput. Phys.*, 230(4):1238–1248, 2011.

- [64] X. Zhang, Y. Xia, and C.-W. Shu. Maximum-principle-satisfying and positivity-preserving high order discontinuous Galerkin schemes for conservation laws on triangular meshes. *J. Sci. Comput.*, 50(1):29–62, 2012.